

REPORT DOCUMENTATION PAGE

Form Approved
OMB No. 0704-0188

Public reporting burden for this collection of information is estimated to average 1 hour per response, including the time for reviewing instructions, searching existing data sources, gathering and maintaining the data needed, and completing and reviewing the collection of information. Send comments regarding this burden estimate or any other aspect of this collection of information, including suggestions for reducing this burden, to Washington Headquarters Services, Directorate for Information Operations and Reports, 1215 Jefferson Davis Highway, Suite 1204, Arlington, VA 22202-4302, and to the Office of Management and Budget, Paperwork Reduction Project (0704-0188), Washington, DC 20503.

1. AGENCY USE ONLY (Leave blank)	2. REPORT DATE	3. REPORT TYPE AND DATES COVERED	
	13 December 1994	Final Report (8/15/92-9/30/94)	
4. TITLE AND SUBTITLE		5. FUNDING NUMBERS	
Analysis of 3D complex structure and heterogeneity effects on formation and propagation of regional phases in Eurasia		Grant F49620-92-J-0461	
6. AUTHOR(S)		8. PERFORMING ORGANIZATION REPORT NUMBER	
Thorne Lay Ru-Shan Wu		AFOSR-TR- 95 0084	
7. PERFORMING ORGANIZATION NAME(S) AND ADDRESS(ES)		9. SPONSORING/MONITORING AGENCY NAME(S) AND ADDRESS(ES)	
University of California, Santa Cruz Institute of Tectonics Applied Science Division Santa Cruz, CA 95064		AFOSR/NL (Sponsor) 110 Duncan Ave. Suite B115 Bolling AFB DC 20332-0001 Prof. Man.: Stanley Dickinson/ NL	
11. SUPPLEMENTARY NOTES		10. SPONSORING/MONITORING AGENCY REPORT NUMBER	
12a. DISTRIBUTION/AVAILABILITY STATEMENT		12b. DISTRIBUTION CODE	
Approval for public release: distribution unlimited		DTIC ELECTED FEB 24 1995	
13. ABSTRACT (Maximum 200 words)			
<p>This is the final report for this grant to develop new three-dimensional wave propagation techniques for high frequency waves in heterogeneous media. The report is divided into four sections, each being a published paper sponsored by this grant. In the first section we formulate a one-way wide-angle elastic wave propagation method for arbitrarily heterogeneous media in both the space and wavenumber domains using elastic Rayleigh integrals and local elastic Born scattering theory. In the second section this complex phase screen method is compared with fourth-order finite differences and exact eigenfunction expansion calculations for two-dimensional inhomogeneous media to assess the accuracy of the one-way propagation algorithm. In the third section, an observational study of continental margin structure influence on Lg propagation is presented, using data from the former Soviet stations for nuclear explosions at Novaya Zemlya. We find that bathymetric features can be correlated with energy levels of Lg, suggesting that waveguide structure influences regional phase energy partitioning. This idea is pursued in the fourth section, using Eurasian earthquake and nuclear explosion data along with information about the crustal structure in Eurasia. We develop empirical relations that reduce the scatter in the P/Lg discriminant at low frequency</p>			
14. SUBJECT TERMS		15. NUMBER OF PAGES	
Wave Propagation Phase Screen Lg Blockage		Regional Phases Inhomogeneous Waves	
		66	
17. SECURITY CLASSIFICATION OF REPORT		18. SECURITY CLASSIFICATION OF THIS PAGE	
Unclassified		Unclassified	
19. SECURITY CLASSIFICATION OF ABSTRACT		20. LIMITATION OF ABSTRACT	
Unclassified		SAR	

Table of Contents

Section 1. Wide-angle elastic wave one-way propagation in heterogeneous media and an elastic wave complex-screen method	1
Section 2. A comparison between phase screen, finite difference, and eigenfunction expansion calculations for scalar waves in inhomogeneous media	17
Section 3. Effects of crustal structure under the Barents and Kara Seas on short-period regional wave propagation for Novaya Zemlya explosions: Empirical relations	32
Section 4. Multivariate analysis of waveguide effects on short-period regional wave propagation in Eurasia and its application in seismic discrimination	48

Accesion For	
NTIS	CRA&I
DTIC	TAB
Unannounced	
Justification _____	
By _____	
Distribution / _____	
Availability Codes	
Dist	Avail and / or Special
A-1	

19950214 005

Wide-angle elastic wave one-way propagation in heterogeneous media and an elastic wave complex-screen method

Ru-Shan Wu

Institute of Tectonics, University of California, Santa Cruz

In this paper a system of equations for wide-angle one-way elastic wave propagation in arbitrarily heterogeneous media is formulated in both the space and wavenumber domains using elastic Rayleigh integrals and local elastic Born scattering theory. The wavenumber domain formulation leads to compact solutions to one-way propagation and scattering problems. It is shown that wide-angle scattering in heterogeneous elastic media cannot be formulated as passage through regular phase-screens, since the interaction between the incident wavefield and the heterogeneities is not local in both the space domain and the wavenumber domain. Our more generally valid formulation is called the "thin-slab" formulation. After applying the small-angle approximation, the thin-slab effect degenerates to that of an elastic complex-screen (or "generalized phase-screen"). Compared with scalar phase-screen, the elastic complex-screen has the following features. (1) For P - P scattering and S - S in-plane scattering, the elastic complex-screen acts as two separate scalar phase-screens for P and S waves respectively. The phase distortions are determined by the P and S wave velocity perturbations respectively. (2) For P - S and S - P conversions, the screen is no longer a pure phase-screen and becomes complex (with both phase and amplitude terms); both conversions are determined by the shear wave velocity perturbation and the shear modulus perturbation. For Poisson solids the S wave velocity perturbation plays a major role. In the special case of $\alpha_0 = 2\beta_0$, S wave velocity perturbation becomes the only factor for both conversions. (3) For the cross-coupling between in-plane S waves and off-plane S waves, only the shear modulus perturbation $\delta\mu$ has influence in the thin-slab formulation. For the complex-screen method the cross-coupling term is neglected because it is a higher order small quantity for small-angle scattering. Relative to prior derivations of vector phase-screen method, our method can correctly treat the conversion between P and S waves and the cross-coupling between differently polarized S waves. A comparison with solutions from three-dimensional finite difference and exact solutions using eigenfunction expansion is made for two special cases. One is for a solid sphere with only P velocity perturbation; the other is with only S velocity perturbation. The Elastic complex-screen method generally agrees well with the three-dimensional finite difference method and the exact solutions. In the limiting case of scalar waves, the derivation in this paper leads to a more generally valid new method, namely, a scalar thin-slab method. When making the small-angle approximation to the interaction term while keeping the propagation term unchanged, the thin-slab method approaches the currently available scalar wide-angle phase-screen method.

1. INTRODUCTION

The one-way wave equation has been widely used for calculating acoustic wavefields, especially in ocean acoustics. The one-way wave equation is a marching algorithm similar to a Markov process, in which the calculation of the next wavefront requires only knowledge of the current wavefront. Compared with the two-way full wave equation, in which at any moment the wavefield is related to the wavefield of the previous time step for the whole space, the one-way equation approach has the advantages of fast computation speed and less storage requirement, and at present is the only method to calculate the long-range acoustic wave propagation in the range-dependent ocean environment [e.g., Tappert, 1977; Flatté and Tappert, 1975; Collins, 1989, 1990]. In exploration geophysics, it has been used for both migration and modeling [e.g., Stoffa *et al.*, 1990; Wu and Huang, 1992].

The generalization of the one-way wave equation to elastic waves has great potential for applications in many disciplines,

such as modeling and inversion in seismic exploration, and long range seismo-acoustic wave propagation in the ocean with the sedimentary-bottom and ice-cap interactions. Modeling long-range crustal wave propagation in heterogeneous wave guides to study the propagation and scattering of regional phases such as Lg , which is an extensively used wave group for yield estimation of underground nuclear explosions, presents another need for such a technique. Especially for three-dimensional (3D) cases, the full two-way elastic wave finite difference method (for a review, see Frankel [1989] is not realistic for the study of long-range propagation and scattering effects.

The traditional way of deriving the one-way parabolic equation for scalar waves is to assume a solution in the form of $p = A \exp(ik_x x)$, where k_x is the principal wavenumber in the propagation direction and A is the slowly varying amplitude function. One substitutes this trial solution into the two-way full wave equation. Taking the small-angle approximation by dropping higher order derivatives in the propagation direction results in a parabolic equation for the amplitude function (see Tappert, [1977]). This approach became very popular in acoustics. The generalization from scalar wave to elastic wave parabolic equations was first introduced by Landers and Claerbout

[1972] for a two-dimensional (2D) case along similar lines. In their derivation, the dilatation and the single nonzero component of the rotation of the elastic wavefield were used as variables, and a higher order approximation was made to extend the valid range to wider propagation angles. *Hudson* [1980] used the displacement fields as variables in his derivation but followed the same single principal wavenumber approach. His derivation is for the 3D case but the approximation was made only for small-angle propagation (parabolic approximation). Now we know that this *single principal wavenumber approach* is only good for the common-mode scattering problem and is intrinsically not appropriate to deal with wave conversion problems. In the case of elastic media, there exist two wave speeds, the compressional and the shear wave speeds. Therefore, two separate parabolic equations must be obtained for both the P and S waves. Although each equation has a coupling term, this pseudo-conversion term may not correctly represent the real physical conversion, because the neglected terms during the process of making the parabolic approximation are not necessarily small compared with the remaining terms due to the large difference between the P and S wavenumbers. It has been shown that in some cases, this approach can lead to unreasonably large errors [Wales and McCoy, 1983].

Another approach is to derive the one-way equation for layered media (one-dimensional media). In this case the downgoing and upgoing waves are decoupled; therefore a one-way matrix equation can be obtained [see: Ursin, 1983; Kennett, 1983; Wapenaar and Berkhouit, 1989; Frazer, 1990]. However, this approach does not have the capacity of dealing with 3D propagation and scattering problems. Some types of one-way finite difference equations can be also derived for the case of a layered medium, which can be applied for weakly range-dependent propagation problems [Greene, 1984, 1985; Wetton and Brooke, 1990; Collins, 1989, 1991]. In this approach, the vertical displacement and the dilatation are used as variables. After normalization of variables for cylindrical spreading, the governing differential equations become 2D coupled equations, which in turn, are factored into one-way equations and the square-root operator is approximated by a higher order Pade' approximation, resulting in a system of stable elastic parabolic equations. The equations are solved by a finite difference algorithm and can be used for wide-angle and weak range-dependent propagation problems. However, this formulation is not capable of dealing with many scattering problems, such as the $SV-SH$ cross-coupling, strong range variations and real 3D scattering problems.

McCoy [1977] and Wales [1986] adopted a perturbation approach and derived a system of elastic parabolic equations for the P and S wave potentials. The two wave speeds are put into the formulation in the beginning; therefore the wave conversion problem can be treated properly. The final result is in the form of a marching finite difference algorithm in the space domain. The method is suitable for small-angle forward propagation problems. Since the free boundary conditions for the potentials are rather difficult to formulate, there are some stability problems for certain wave types [Wales, 1986].

Fisk and McCarter [1991], hereafter identified as FM91, have introduced a vector phase-screen method for elastic waves, and made some comparisons with the 2D finite difference method [Fisk et al., 1992]. They assumed that the medium is smooth and the gradients of parameter variation can be neglected, resulting in a pair of decoupled P and S wave equations. The scattering effects are simulated by passing the P

and S waves through two separate phase-screens involving P and S wave speed perturbations, respectively. The $P-S$ conversion is obtained by projecting the distorted P wavefront to the corresponding S wave components. The same is done for the $S-P$ conversion. The procedure is relatively simple. However, there exists some intrinsic difficulty and internal inconsistency in this approach. First, the basic assumption of decoupled P and S wave equations implies that the theory is not capable of dealing with the conversion problem. The theory can only handle the first-order effects of the wave front distortion due to velocity perturbations, such as focusing and defocusing, and coda generation by forward scattering. Formally projecting the distorted P wave front into S wave components may produce nonphysical conversions. We will discuss this in section 4. Second, there is ambiguity about the scattering effects of perturbations of different parameters. In their method (FM91), $P-P$ and $P-S$ scattering are determined by P wave velocity perturbations $\delta\alpha$, while $S-S$ and $S-P$ scattering are determined by S wave perturbations $\delta\beta$, leading to ambiguity in selecting the combination of three perturbations $\delta\alpha$, $\delta\lambda$, and $\delta\mu$ for an isotropic elastic medium. The P wave velocity perturbation $\delta\alpha$ could be an arbitrary combination of $\delta\alpha$, $\delta\lambda$, $\delta\mu$. While these perturbations can have very different scattering effects, the method they adopted could not distinguish between these effects, which implies again that the method cannot handle the wave conversion properly.

In this paper I will derive one-way elastic wave equations for P and S displacement fields using the elastic wave Rayleigh integrals and elastic Born scattering theory following a perturbation approach. First the wide-angle "thin-slab" formulas are derived in space domain (section 2) and wavenumber domain (section 3). The method can be implemented in the wavenumber domain similar to a generalized split-step algorithm for elastic waves, and applied to wide-angle forward scattering problems. Next, an elastic "complex-screen" algorithm is obtained by using the small-angle approximation (parabolic approximation) (section 4), which can be implemented by a dual-domain technique using fast Fourier transform (FFT), which has much faster speed (2 to 3 orders of magnitude) than the thin-slab method. Computation speed is discussed, and comparison with finite difference and exact solutions for an elastic sphere is made through numerical examples (section 4). Finally, the limiting case of scalar waves is obtained in section 5. This approach leads to a scalar thin-slab algorithm, which is valid under more general conditions than the currently available "wide-angle" phase-screen methods. When making the small-angle approximation to the interaction term while keeping the propagation term unchanged, the method approaches the regular wide-angle scalar phase-screen [Feit and Fleck, 1978; Thomson and Chapman, 1983].

2. SPACE DOMAIN FORMULATION

General Media

The equation of motion in a linear, heterogeneous elastic

$$\rho(\mathbf{x})\ddot{\mathbf{u}}(\mathbf{x}) = \nabla \cdot \boldsymbol{\sigma}(\mathbf{x}) \quad (1)$$

where \mathbf{u} is the displacement vector, $\boldsymbol{\sigma}(\mathbf{x})$ is the stress tensor (dyadic) and ρ is the density of the medium. Here $\ddot{\mathbf{u}}$ is defined as $\partial^2 \mathbf{u} / \partial t^2$. We assume no body force exists in the medium. We know the stress-displacement relation

$$\sigma(x) = c(x) : \epsilon(x) = \frac{1}{2} c : (\nabla u + u \nabla) \quad (2)$$

where c is the elastic constant tensor of the medium, ϵ is the strain field, $u \nabla$ stands for the transpose of ∇u , and ":" stands for double scalar product of tensors defined through $(ab):(cd) = (b \cdot c)(a \cdot d)$. Equation (1) can then be written as a wave equation of the displacement field:

$$\rho(x) \ddot{u}(x) = \nabla \cdot \left[\frac{1}{2} c : (\nabla u + u \nabla) \right]. \quad (3)$$

If the parameters of the elastic medium and the total wave field can be decomposed as

$$\begin{aligned} \rho(x) &= \rho_0 + \delta\rho(x) \\ c(x) &= c_0 + \delta c(x) \\ u(x) &= u^0(x) + U(x) \end{aligned} \quad (4)$$

where ρ_0 and c_0 are the parameters of the background medium, $\delta\rho$ and δc are the corresponding perturbations, u^0 is the incident field and U is the scattered field, then (3) can be rewritten as

$$\rho_0 \ddot{U} - \nabla \cdot \left[\frac{1}{2} c_0 : (\nabla U + U \nabla) \right] = Q \quad (5)$$

$$Q = - \left\{ \delta\rho \ddot{u} - \nabla \cdot \left[\frac{1}{2} \delta c : (\nabla u + u \nabla) \right] \right\} = - \delta\rho \ddot{u} + \nabla \cdot [\delta c : \epsilon] \quad (6)$$

where Q is the equivalent body force due to scattering. Note that u also satisfies equation (5).

If the wave field is known on a closed surface S , then from the representation theory [Aki and Richards, 1980] we can express the solution of (5) as the sum of a surface integral and a volume integral

$$\begin{aligned} u(x_1) &= \int_S dS \left\{ [\hat{n} \cdot \sigma(x)] \cdot G(x, x_1) - u(x) \cdot [\hat{n} \cdot \Sigma(x, x_1)] \right\} \\ &+ \int_V Q(x) \cdot G(x_1, x) \end{aligned} \quad (7)$$

where $\sigma(x)$ is the stress field on the surface, $T(x) = \hat{n} \cdot \sigma(x)$ is the corresponding traction field, $u(x)$ is the displacement field on the surface, \hat{n} is the outward normal, $G(x, x_1)$, $\Sigma(x, x_1)$, and

$\Sigma_n(x, x_1) = \hat{n} \cdot \Sigma(x, x_1)$ are the Green's displacement, stress, and traction tensors, respectively. This representation integral in the present form was first introduced and discussed by Love in 1904 (in a more general form first by Betti in 1872 [e.g., Aki and Richards 1980]), and is called the Love integral or the elastic-wave Kirchhoff integral [Pao and Varatharajulu, 1976]. Note that the Love integral (the surface integral) is from the contribution of outside sources, i.e. the sources outside the surface. The known field on the surface can be generated by actual sources outside the surface, or by scattering of the heterogeneities outside the surface. The scattered field generated by the heterogeneities inside the surface will have zero value of the surface integration and therefore does not contribute to the Love integral. We can then call the part of field represented by the Love integral as the primary field. Therefore, (7) becomes

$$u(x_1) = u^0(x_1) + U(x_1) \quad (8)$$

$$u^0(x_1) = \int_S dS \left\{ T(x) \cdot G(x, x_1) - u(x) \cdot \Sigma_n(x, x_1) \right\} \quad (9)$$

$$\begin{aligned} U(x_1) &= \int_V dV \left\{ -\delta\rho(x) \ddot{u}(x) \cdot G(x_1, x) + \nabla \cdot [\delta c : \epsilon(x)] \cdot G(x_1, x) \right\} \\ &= \int_V dV \left\{ -\delta\rho(x) \ddot{u}(x) \cdot G(x_1, x) - [\delta c : \epsilon(x)] : \nabla G(x_1, x) \right\}. \end{aligned} \quad (10)$$

In equation (10) integration by parts has been used so that the volume integration contains no gradients of the elastic constants [see Wu and Aki, 1985; Wu, 1989b]. Note that in (7) and (10) the integration volume V is over the whole volume which contains all the scatterers. When performing integration by parts, the surface is chosen to be outside the heterogeneous region, so that the surface terms vanish.

Now we formulate the *representation integral for the forward propagation* problem. Suppose the incident wave is propagating along the x -axis. Now consider that the integration surface in the Love integral is composed of a plane surface S at x , which is perpendicular to the propagation direction, and a hemisphere with a large radius. As seen in Figure 1, we can assume that the major contribution to the surface integral to calculate the primary field between planes S and S_1 is from the large-aperture plane surface S . The contribution from the other parts of the closed surface can be neglected due to the weakness and time delay of the signal. Therefore the Love integral gives the elastic wave field generated by the sources and by wave scattering of all the heterogeneities on the left-hand side of plane S .

Now let us examine the contribution from volume heterogeneities. Now the volume integral accounts for the contribution from all the scatterers on the right-hand side of S . However, under the one-way propagation assumption, the backscattered waves are neglected, and therefore the contribution from the scatterers on the right-hand side of S_1 on which the observation point x_1 is situated, is excluded. Furthermore, if the distance between S and S_1 is small, then the field $u(x')$, where x' is situated between x and x_1 , can be approximated by $u^0(x')$, since the modification of the wave field due to scattering between S and S_1 is small compared with $u^0(x')$. Therefore, the scattered field can be approximated as

$$U(x_1) = \int_V (x') \left\{ -\delta\rho(x') \ddot{u}^0(x') \cdot G(x_1, x') - [\delta c(x') : \epsilon^0(x')] : \nabla' G(x_1, x') \right\} \quad (11)$$

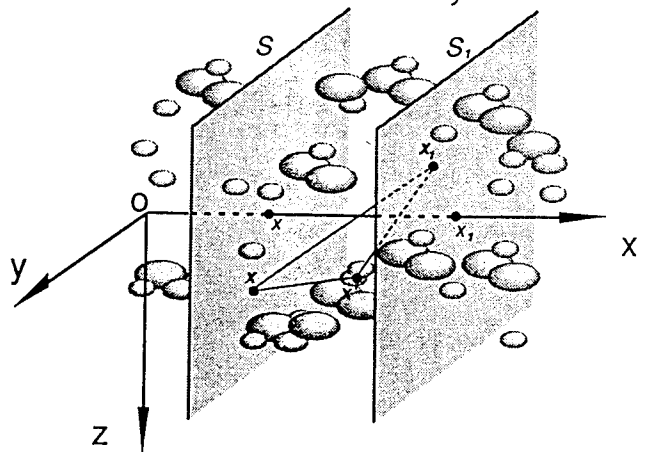


Fig. 1. Geometry of the derivation. The medium is sliced into thin slabs. Now consider the scattering and propagation effects of the thin-slab between plane S and S_1 . Suppose the wave field is known on S . The wave field on S_1 will be formulated by the forward propagation approximation.

where ∇' means the operation is taken with respect to \mathbf{x}' , a point inside the slab. In fact, this is an integral of elastic Born scattering [Gubernatis *et al.*, 1977; Wu and Aki, 1985; Wu, 1989b]. Here we can consider (11) as a local Born approximation.

In order to calculate $\mathbf{u}(\mathbf{x}_1)$, we need to determine $\mathbf{u}^0(\mathbf{x}_1)$, $\mathbf{u}^0(\mathbf{x}')$ and $\mathbf{\Sigma}(\mathbf{x}')$ from the known field on S using the Love integral. It has been shown that in the case of one-way propagation from a plane surface, the Love integral can be replaced by an elastic-wave Rayleigh integral (ERI) which is simpler and computationally much more efficient [Wu, 1989a; Wapenaar and Berkhouw, 1989]

$$\mathbf{u}^0(\mathbf{x}_1) = -2 \int_S dS \mathbf{u}(\mathbf{x}) \cdot \mathbf{\Sigma}_n(\mathbf{x}, \mathbf{x}_1). \quad (12)$$

This is ERI of type II. Similarly, we can calculate the strain field

$$\mathbf{\Sigma}^0(\mathbf{x}') = -2 \int_S dS \mathbf{u}(\mathbf{x}) \cdot \mathbf{\Sigma}_x[\mathbf{\Sigma}_n(\mathbf{x}, \mathbf{x}')]. \quad (13)$$

where $\mathbf{\Sigma}_x[\cdot]$ is the strain operator:

$$\mathbf{\Sigma}_x[\mathbf{a}] = \frac{1}{2} [\nabla_x \mathbf{a} + \mathbf{a} \nabla_x], \quad (14)$$

where ∇_x stands for taking a gradient with respect to \mathbf{x} .

Equivalently, if the traction field $\mathbf{T}(\mathbf{x})$ is known on S , the strain field can be calculated using the ERI of type I:

$$\mathbf{\Sigma}^0(\mathbf{x}') = 2 \int_S dS \mathbf{T}(\mathbf{x}) \cdot \mathbf{E}'(\mathbf{x}, \mathbf{x}') \quad (15)$$

where $\mathbf{E}'(\mathbf{x}, \mathbf{x}')$ is Green's strain tensor, defined as

$$\mathbf{E}'(\mathbf{x}, \mathbf{x}') = \mathbf{\Sigma}_x[\mathbf{G}(\mathbf{x}, \mathbf{x}')] = \frac{1}{2} [\nabla' \mathbf{G}(\mathbf{x}, \mathbf{x}') + (\nabla' \mathbf{G}(\mathbf{x}, \mathbf{x}'))^{213}] \quad (16)$$

where $\nabla' \mathbf{G}$ stands for taking the gradient of \mathbf{G} with respect to \mathbf{x}' and $(\nabla' \mathbf{G})^{213}$, the transpose of $\nabla' \mathbf{G}$ with respect to the first two indexes. The traction field is related to the strain field by

$$\mathbf{T}(\mathbf{x}) = \hat{\mathbf{n}} \cdot [\mathbf{c}(\mathbf{x}) : \mathbf{\Sigma}(\mathbf{x})]. \quad (17)$$

Isotropic Media

In the case of isotropic media, equations (8), (12), (11), and (15) can be further simplified to (in the frequency domain)

$$\mathbf{u}(\mathbf{x}_1) = \mathbf{u}^0(\mathbf{x}_1) + \mathbf{U}(\mathbf{x}_1) \quad (18)$$

$$\mathbf{u}^0(\mathbf{x}_1) = -2 \int_S dS \mathbf{u}(\mathbf{x}) \cdot \mathbf{\Sigma}_n(\mathbf{x}, \mathbf{x}_1) \quad (19)$$

$$\begin{aligned} \mathbf{U}(\mathbf{x}_1) = & \omega^2 \int_V dV \delta\rho(\mathbf{x}') \mathbf{u}^0(\mathbf{x}') \cdot \mathbf{G}(\mathbf{x}_1, \mathbf{x}') \\ & + \int_V dV \left[\delta\lambda(\mathbf{x}') \mathbf{\Sigma}^0(\mathbf{x}') \mathbf{I} + 2\delta\mu(\mathbf{x}') \mathbf{\Sigma}^0(\mathbf{x}') \right] : \nabla' \mathbf{G}(\mathbf{x}_1, \mathbf{x}') \end{aligned} \quad (20)$$

with $\mathbf{u}^0(\mathbf{x}')$ and $\mathbf{\Sigma}^0(\mathbf{x}')$ calculated by ERI of type II and type I, respectively. For the calculation of $\mathbf{\Sigma}^0(\mathbf{x}')$, (15) can be used and the traction field can be determined in this case by

$$\mathbf{T}(\mathbf{x}) = \hat{\mathbf{n}} \cdot \left[\lambda(\mathbf{x}) \mathbf{\Sigma}(\mathbf{x}) \mathbf{I} + 2\mu(\mathbf{x}) \mathbf{\Sigma}(\mathbf{x}) \right] \quad (21)$$

where \mathbf{I} is the unit tensor (idemfactor) and $|\mathbf{\Sigma}(\mathbf{x})| = \mathbf{I} : \mathbf{\Sigma}(\mathbf{x}) = \nabla \cdot \mathbf{u}(\mathbf{x})$.

Assuming a homogeneous background, Green's tensors in the above formulas can be written out explicitly. For details see Appendix A.

3. WAVE NUMBER DOMAIN FORMULATION

Referring to the geometry in Figure 1, Let us calculate the scattered field by the heterogeneities within a vertical thin slab of width $\Delta x = x_1 - x$. Assume we know the displacement field on the surface S , $\mathbf{u}^0(\mathbf{x}, \mathbf{x}_T)$, where $\mathbf{x}_T = (y, z)$ is the 2D position vector in the $y-z$ plane. For the sake of simplicity, we put $x = 0$ in the following derivation.

We decompose \mathbf{u}^0 on the surface S into plane waves

$$\mathbf{u}^0(0, \mathbf{x}_T) = \mathbf{u}_\alpha^0(0, \mathbf{x}_T) + \mathbf{u}_\beta^0(0, \mathbf{x}_T)$$

$$\mathbf{u}^0(0, \mathbf{x}_T) = \frac{1}{4\pi^2} \int d\mathbf{K}_T [\mathbf{u}_\alpha^0(\mathbf{K}_T) + \mathbf{u}_\beta^0(\mathbf{K}_T)] e^{i\mathbf{K}_T \cdot \mathbf{x}_T}. \quad (22)$$

Then the displacement field \mathbf{u}^0 everywhere in the slab can be expressed as

$$\begin{aligned} \mathbf{u}^0(\mathbf{x}') &= \mathbf{u}_\alpha^0(\mathbf{x}') + \mathbf{u}_\beta^0(\mathbf{x}') \\ &= \frac{1}{4\pi^2} \int d\mathbf{K}_T [\mathbf{u}_\alpha^0(\mathbf{K}_T) e^{i\mathbf{k}_\alpha \cdot \mathbf{x}'} + \mathbf{u}_\beta^0(\mathbf{K}_T) e^{i\mathbf{k}_\beta \cdot \mathbf{x}'}] \end{aligned} \quad (23)$$

where

$$\begin{aligned} \mathbf{k}_\alpha &= \sqrt{k_\alpha^2 - K_T^2} \hat{\mathbf{e}}_x + \mathbf{K}_T = \gamma_\alpha \hat{\mathbf{e}}_x + \mathbf{K}_T \\ \mathbf{k}_\beta &= \sqrt{k_\beta^2 - K_T^2} \hat{\mathbf{e}}_x + \mathbf{K}_T = \gamma_\beta \hat{\mathbf{e}}_x + \mathbf{K}_T \end{aligned} \quad (24)$$

and the strain field

$$\begin{aligned} \mathbf{\Sigma}^0(\mathbf{x}') &= \mathbf{\Sigma}_\alpha^0(\mathbf{x}') + \mathbf{\Sigma}_\beta^0(\mathbf{x}') = \frac{1}{2} (\nabla' \mathbf{u}^0 + \mathbf{u}^0 \nabla') \\ &= \frac{1}{8\pi^2} \int d\mathbf{K}_T [ik_\alpha (\hat{k}_\alpha \mathbf{u}_\alpha^0 + \mathbf{u}_\alpha^0 \hat{k}_\alpha) e^{i\mathbf{k}_\alpha \cdot \mathbf{x}'} \\ &\quad + ik_\beta (\hat{k}_\beta \mathbf{u}_\beta^0 + \mathbf{u}_\beta^0 \hat{k}_\beta) e^{i\mathbf{k}_\beta \cdot \mathbf{x}'}]. \end{aligned} \quad (25)$$

Also we decompose the scattered field $\mathbf{U}(\mathbf{x})$ expressed by (20) on the surface S_1 into plane waves. Substituting (23), (25), and the wavenumber domain expressions of Green's tensors (see the derivation in Appendix B) into (20), we can derive the expressions of the elastic wave Born scattering in wavenumber domain. As a demonstration of the procedure, we derive here the scattered P wave contributed by $\delta\rho$ for an incident P wave:

$$\begin{aligned} \mathbf{U}_p^{PP}(\mathbf{x}) &= \omega^2 \int_V dV \delta\rho(\mathbf{x}') \mathbf{u}^0(\mathbf{x}') \cdot \mathbf{G}_\alpha(\mathbf{x}, \mathbf{x}') \\ &= \frac{\omega^2}{4\pi^2} \int d\mathbf{K}'_T \int d\mathbf{K}_T \int_V dV \delta\rho(\mathbf{x}') e^{i\mathbf{k}_\alpha \cdot \mathbf{x}'} \\ &\quad \times \frac{ik_\alpha^2}{8\pi^2 \rho_0 \omega^2 \gamma_\alpha} (\mathbf{u}_\alpha^0(\mathbf{K}_T) \cdot \hat{k}'_\alpha) \hat{k}'_\alpha e^{i\mathbf{k}'_\alpha \cdot (\mathbf{x} - \mathbf{x}')} \\ &= \frac{1}{4\pi^2} \int d\mathbf{K}'_T e^{i\mathbf{K}'_T \cdot \mathbf{x}_T} \frac{i e^{i\gamma_\alpha \Delta x}}{2\gamma_\alpha} \\ &\quad \times \frac{1}{4\pi^2} \int d\mathbf{K}_T k_\alpha^2 \frac{\delta\rho(\mathbf{k}'_\alpha - \mathbf{k}_\alpha)}{\rho_0} \mathbf{u}_\alpha^0(\mathbf{K}_T) (\hat{k}_\alpha \cdot \hat{k}'_\alpha) \hat{k}'_\alpha \end{aligned} \quad (26)$$

where $\mathbf{u}_\alpha^0(\mathbf{K}_T) = |\mathbf{u}_\alpha^0(\mathbf{K}_T)|$ and $\delta\rho(\mathbf{k}_\alpha)$ is the 3D Fourier transform of $\delta\rho(\mathbf{x})$:

$$\begin{aligned}\delta\rho(k_\alpha) &= \int_V dV \delta\rho(x, K_T) e^{-iK_T \cdot x} e^{-i\gamma_\alpha x} \\ &= \int_0^{\Delta x} \delta\rho(x, K_T) e^{-i\gamma_\alpha x} dx.\end{aligned}\quad (27)$$

Therefore,

$$\begin{aligned}U_p^{PP}(x, K'_T) &= \frac{ie^{i\gamma_\alpha \Delta x}}{2\gamma_\alpha} k_\alpha^2 \frac{1}{4\pi^2} \int dK_T \\ &\times \frac{\delta\rho(\gamma_\alpha \cdot \gamma_\alpha, K'_T \cdot K_T)}{\rho_0} u_\alpha^0(0, K_T) (\hat{k}_\alpha \cdot \hat{k}'_\alpha) \hat{k}'_\alpha.\end{aligned}\quad (28)$$

We recognize that the phase term $e^{i\gamma_\alpha x}$ represents the plane wave propagation between the two surfaces. Then the $\delta\rho$ contribution to the scattered P wave of the wavenumber K'_T for an incident plane wave with wavenumber K_T can be represented as

$$U_p^{PP}(K'_T, K_T) = \frac{i}{2\gamma_\alpha} k_\alpha^2 \frac{\delta\rho(k'_\alpha - k_\alpha)}{\rho_0} u_\alpha^0(K_T) (\hat{k}_\alpha \cdot \hat{k}'_\alpha) \hat{k}'_\alpha\quad (29)$$

This is the wavenumber-domain formula of elastic wave scattering by the Born approximation (here the local Born approximation). It is similar to that of the far-field Born scattering [see Wu and Aki, 1985; Wu, 1989b] except for a weighting factor $i/2\gamma_\alpha$. However, in this wavenumber-domain formulation, no far-field approximation is made. The only approximation is the local Born approximation.

Following the same procedure for other parts of the scattered field, we have

$$\begin{aligned}U(K'_T, K_T) &= U^{PP}(K'_T, K_T) + U^{PS}(K'_T, K_T) \\ &+ U^{SP}(K'_T, K_T) + U^{SS}(K'_T, K_T)\quad (30) \\ U^{PP}(K'_T, K_T) &= \frac{i}{2\gamma_\alpha} k_\alpha^2 u_\alpha^0 \hat{k}'_\alpha \left\{ (\hat{k}_\alpha \cdot \hat{k}'_\alpha) \frac{\delta\rho(\tilde{k})}{\rho_0} \right. \\ &\left. - \frac{\delta\lambda(\tilde{k})}{\lambda_0 + 2\mu_0} \cdot (\hat{k}_\alpha \cdot \hat{k}'_\alpha)^2 \frac{2\delta\mu(\tilde{k})}{\lambda_0 + 2\mu_0} \right\} \\ U^{PS}(K'_T, K_T) &= \frac{i}{2\gamma_\beta} k_\beta^2 u_\alpha^0 [\hat{k}_\alpha \cdot \hat{k}'_\beta (\hat{k}_\alpha \cdot \hat{k}'_\beta)] \left\{ \frac{\delta\rho(\tilde{k})}{\rho_0} \right. \\ &\left. - 2\left(\frac{\beta_0}{\alpha_0}\right) (\hat{k}_\alpha \cdot \hat{k}'_\beta) \frac{\delta\mu(\tilde{k})}{\mu_0} \right\} \\ U^{SP}(K'_T, K_T) &= \frac{i}{2\gamma_\alpha} k_\alpha^2 (u_\beta^0 \cdot \hat{k}'_\alpha) \hat{k}'_\alpha \left\{ \frac{\delta\rho(\tilde{k})}{\rho_0} \right. \\ &\left. - 2\left(\frac{\beta_0}{\alpha_0}\right) (\hat{k}_\beta \cdot \hat{k}'_\alpha) \frac{\delta\mu(\tilde{k})}{\mu_0} \right\} \\ U^{SS}(K'_T, K_T) &= \frac{i}{2\gamma_\beta} k_\beta^2 \left\{ [u_\beta^0 \cdot \hat{k}'_\beta (u_\beta^0 \cdot \hat{k}'_\beta)] \frac{\delta\rho(\tilde{k})}{\rho_0} \right. \\ &\left. - \left[(\hat{k}_\beta \cdot \hat{k}'_\beta) (u_\beta^0 \cdot \hat{k}'_\beta) (u_\beta^0 \cdot \hat{k}'_\beta) + (u_\beta^0 \cdot \hat{k}'_\beta) (\hat{k}_\beta \cdot \hat{k}'_\beta) (\hat{k}_\beta \cdot \hat{k}'_\beta) \right] \frac{\delta\mu(\tilde{k})}{\mu_0} \right\} \\ &= \frac{i}{2\gamma_\beta} k_\beta^2 \left\{ \hat{m} |\mathbf{M}| \left[\frac{\delta\rho(\tilde{k})}{\rho_0} - (\hat{k}_\beta \cdot \hat{k}'_\beta) [1 - \frac{(\hat{k}'_\beta \cdot \hat{a})^2}{|\mathbf{M}|^2}] \frac{\delta\mu(\tilde{k})}{\mu_0} \right] \right. \\ &\left. - \hat{I} (u_\beta^0 \cdot \hat{k}'_\beta) (\hat{I} \cdot \hat{k}_\beta) \frac{\delta\mu(\tilde{k})}{\mu_0} \right\}\quad (31)\end{aligned}$$

where $u_\alpha^0 = |u_\alpha^0(K_T)|$, $u_\beta^0 = u_\beta^0(K_T)$, $\hat{a} = u_\beta^0/|u_\beta^0|$ and $\hat{m} = \mathbf{M}/|\mathbf{M}|$, $\mathbf{M} = u_\beta^0 \cdot \hat{k}'_\beta (u_\beta^0 \cdot \hat{k}'_\beta)$, $\hat{I} = \hat{m} \times \hat{k}'_\beta$.

In (31), $\tilde{k} = \mathbf{k}^{sc} - \mathbf{k}^{in}$ is the exchange wavenumber with \mathbf{k}^{in} , \mathbf{k}^{sc} as the incident and scattering wavenumbers, respectively, and

$$\begin{aligned}k_\alpha &= \sqrt{k_\alpha^2 - K_T^2} \hat{e}_x + K_T \\ k_\beta &= \sqrt{k_\beta^2 - K_T^2} \hat{e}_x + K_T \\ k'_\alpha &= \sqrt{k_\alpha^2 - K'_T^2} \hat{e}_x + K'_T \\ k'_\beta &= \sqrt{k_\beta^2 - K'_T^2} \hat{e}_x + K'_T.\end{aligned}\quad (32)$$

Note that \hat{m} is perpendicular to the outgoing direction \hat{k}'_β and lies in the plane determined by u_β^0 and \hat{k}'_β . Therefore, the first term of the last equation in (31) stands for the in-plane S wave, i.e. the non-coupled S wave; while \hat{I} is the off-plane unit vector which is perpendicular to both the outgoing direction and \hat{m} . We see the cross-coupling (the depolarization of S waves) can only be generated by shear modulus perturbations $\delta\mu$.

To obtain the scattered field at the surface S_1 with transverse wavenumber K'_T , we need to sum up the contributions from all the incident plane waves:

$$\begin{aligned}U^P(K'_T) &= \frac{1}{4\pi^2} \int dK_T e^{i\gamma_\alpha \Delta x} [U^{PP}(K'_T, K_T) + U^{SP}(K'_T, K_T)] \\ U^S(K'_T) &= \frac{1}{4\pi^2} \int dK_T e^{i\gamma_\beta \Delta x} [U^{PS}(K'_T, K_T) + U^{SS}(K'_T, K_T)]\end{aligned}\quad (33)$$

where Δx is the distance between the two surfaces. To account for the scattering effect of the heterogeneities between x and x_1 the integration limits in (27) need to be changed to x and x_1 .

The free propagation of the incident field in the wavenumber domain can be obtained from (19) by substituting (23) and the plane wave decomposition of $\Sigma_n(x, x')$ (Appendix B):

$$\begin{aligned}u^0(x_1) &= 2 \int_S dS u(x) \cdot \Sigma_x(x, x_1) \\ &= 2 \int_S dS \left\{ u_\alpha^0(x) \cdot \Sigma_x^\alpha(x, x_1) + u_\beta^0(x) \cdot \Sigma_x^\beta(x, x_1) \right\} \\ &= -\frac{1}{2\pi^2} \int_S dS \int dK_T \int dK'_T \frac{1}{8\pi^2 \rho \omega^2} \left\{ \right. \\ &\left. \frac{k_\alpha'^3}{\gamma_\alpha} e^{i\mathbf{k}'_\alpha \cdot (x_1 - x)} e^{i\mathbf{k}'_\alpha \cdot x} \left[\lambda(u_\alpha^0 \cdot \hat{x}) \hat{k}'_\alpha + 2\mu(u_\alpha^0 \cdot \hat{k}'_\alpha) (\hat{x} \cdot \hat{k}'_\alpha) \hat{k}'_\alpha \right] \right. \\ &\left. + \frac{k_\beta'^3}{\gamma_\beta} e^{i\mathbf{k}'_\beta \cdot (x_1 - x)} e^{i\mathbf{k}'_\beta \cdot x} \mu \right. \\ &\left. \times \left[(\hat{x} \cdot \hat{k}'_\beta) u_\beta^0 + (u_\beta^0 \cdot \hat{k}'_\beta) \hat{x} - 2(\hat{x} \cdot \hat{k}'_\beta) (u_\beta^0 \cdot \hat{k}'_\beta) \hat{k}'_\beta \right] \right\}.\end{aligned}\quad (34)$$

Knowing that

$$\begin{aligned} \int_S dS e^{i(\mathbf{k}_\alpha \cdot \mathbf{k}'_\alpha) \cdot x} &= e^{i(\gamma_\alpha \cdot \gamma'_\alpha) x} \int_S dS e^{i(K_T \cdot K'_T) \cdot x} \\ &= 4\pi^2 \delta(K_T - K'_T) e^{i(\gamma_\alpha \cdot \gamma'_\alpha) x} \\ \int_S dS e^{i(\mathbf{k}_\beta \cdot \mathbf{k}'_\beta) \cdot x} &= 4\pi^2 \delta(K_T - K'_T) e^{i(\gamma_\beta \cdot \gamma'_\beta) x}\end{aligned}\quad (35)$$

and noticing that $(\mathbf{u}_\beta^0 \cdot \hat{\mathbf{k}}_\beta) = 0$, the integration over \mathbf{K}'_T can be completed, resulting in

$$\mathbf{u}^0(\mathbf{x}_1) = -2 \int d\mathbf{K}_T \frac{1}{8\pi^2 \rho \omega^2} \left\{ \frac{k_\alpha^3}{\gamma_\alpha} e^{i\mathbf{k}_\alpha \cdot \mathbf{x}_1} (\lambda + 2\mu) (\hat{\mathbf{k}}_\alpha \cdot \hat{\mathbf{x}}) \mathbf{u}_\alpha^0(\mathbf{K}_T) \right. \\ \left. + \frac{k_\beta^3}{\gamma_\beta} e^{i\mathbf{k}_\beta \cdot \mathbf{x}_1} \mu (\hat{\mathbf{x}} \cdot \hat{\mathbf{k}}_\beta) \mathbf{u}_\beta^0(\mathbf{K}_T) \right\}. \quad (36)$$

By inspection, we obtain

$$\mathbf{u}^0(\mathbf{x}_1, \mathbf{K}_T) = \mathbf{u}_\alpha^0(\mathbf{x}, \mathbf{K}_T) e^{i\gamma_\alpha \Delta x} + \mathbf{u}_\beta^0(\mathbf{x}, \mathbf{K}_T) e^{i\gamma_\beta \Delta x}. \quad (37)$$

As expected, this is simply the free propagation between the two planes.

Finally, the total field at \mathbf{x}_1 is obtained by summing up the primary field (37) and the scattered field (33):

$$\mathbf{u}^P(\mathbf{x}_1, \mathbf{K}'_T) = e^{i\gamma_\alpha \Delta x} \left\{ \mathbf{u}_\alpha^0(\mathbf{x}, \mathbf{K}'_T) \right. \\ \left. + \frac{1}{4\pi^2} \int d\mathbf{K}_T \left[\mathbf{U}^{PP}(\mathbf{K}'_T, \mathbf{K}_T) + \mathbf{U}^{SP}(\mathbf{K}'_T, \mathbf{K}_T) \right] \right\} \\ \mathbf{u}^S(\mathbf{x}_1, \mathbf{K}'_T) = e^{i\gamma_\beta \Delta x} \left\{ \mathbf{u}_\beta^0(\mathbf{x}, \mathbf{K}'_T) \right. \\ \left. + \frac{1}{4\pi^2} \int d\mathbf{K}_T \left[\mathbf{U}^{SS}(\mathbf{K}'_T, \mathbf{K}_T) + \mathbf{U}^{PS}(\mathbf{K}'_T, \mathbf{K}_T) \right] \right\}. \quad (38)$$

The above procedure can be implemented iteratively in the wavenumber domain, and the propagation will march step by step in the forward direction. For each new step, the total field calculated using (38) from the previous step is taken as the incident field, and then the scattered and primary fields on the end surface of the new thin-slab are calculated by (31) and (37), respectively. This marching algorithm includes all the diffraction and forward scattering effects. The wave-type conversion is expressed by the terms \mathbf{U}^{SP} and \mathbf{U}^{PS} . Note that for this wide-angle forward scattering algorithm, the wavenumber coupling integrals (33) are not convolutions. Therefore the corresponding operations in space domain are not local. This shows that for wide-angle propagation, the correct scattering effect cannot be modeled with standard phase-screens. We will call the above version of our formulation represented by (31), (37), and (38) as the "thin slab" method. The thickness of the "thin-slab" should satisfy two criteria. One is from a requirement of the Born approximation. In order to keep the scattered field small compared with the incident field, roughly speaking, the phase deviation due to passage of wave through the thin-slab should be less than 1 rad, similar to equation (15) of Wu [1989b]. For $P-P$ scattering, it is

$$\frac{d\alpha}{\alpha_0} k_\alpha \Delta x < 1$$

where k_α is the maximum wavenumber of the wave field. The other criterion is that the propagation within the thin-slab should satisfy geometric optics, which requires that the Fresnel radius on S_1 due to a propagation distance Δx be smaller than

the average size of heterogeneities on S_1 . Detailed discussion will appear in future publications.

Now we estimate the amount of computation involved. The thin-slab method is a wavenumber domain marching algorithm. The model perturbations $\delta\rho$, $\delta\lambda$ and $\delta\mu$ can be transformed to the spectral domain using FFT before propagation. The computation for this transformation is negligible compared with the propagation calculation. For each step forward (propagation of Δx), we need many mappings (matrix multiplications) from the \mathbf{K}_T plane to \mathbf{K}'_T plane. For \mathbf{U}^{PP} , \mathbf{U}^{PS} , and \mathbf{U}^{SP} , we need one scalar mapping for each. \mathbf{U}^{SS} has two orthogonal components and therefore needs two mappings. Therefore, there are a total of 5 mappings for each step. The amount of computation is similar to FM91's vector phase-screen algorithm in terms of order of magnitude, though the thin-slab method has more projection calculations. However, since the slab thickness is only required to be small enough for the Born approximation to be valid, it can be larger than the step length of the screen method which makes an additional parabolic approximation, as will be discussed in next section. For 3D modeling the thin-slab method is still computationally intensive, although it is much faster than the 3D finite difference method. In the following we will make further approximations and derive a much faster *elastic complex-screen (ECS)* method.

4. SMALL-ANGLE SCATTERING APPROXIMATION: A COMPLEX SCREEN FORMULATION

The forward scattering calculations in (33) and (31) are valid for wide-angle scattering. If we consider only small-angle forward propagation, then the parabolic approximation can be used to further simplify the formulas. Here we follow the approximations made by Wales and McCoy [1983] in their derivation using displacement potentials. The goal is to "compress" the thin-slabs into "screens", then replace the wavenumber domain matrix operations with space domain point-to-point multiplications, as in the scalar wave phase-screen method. In this way, a dual-domain technique using FFTs can be applied to speed up the computation substantially.

In the wavenumber domain the parabolic approximation can be expressed as

$$\gamma = \sqrt{k^2 - K_T^2} \approx k \left(1 - \frac{K_T^2}{2k^2} \right) \quad |K_T| \ll k. \quad (39)$$

Now we make approximations to the exchange wavenumbers:

$$\mathbf{k}'_\alpha \cdot \mathbf{k}_\alpha = (\sqrt{k_\alpha^2 - K'_T^2} - \sqrt{k_\alpha^2 - K_T^2}) \hat{\mathbf{e}}_x + \mathbf{K}'_T \cdot \mathbf{K}_T \\ \approx \frac{K_T^2}{2k^2} - \frac{K'_T}{2k^2} \hat{\mathbf{e}}_x + \mathbf{K}'_T \cdot \mathbf{K}_T \approx 0 \hat{\mathbf{e}}_x + \mathbf{K}'_T \cdot \mathbf{K}_T. \quad (40)$$

Here we drop the term $(K_T^2/2k^2 \cdot K'_T/2k^2)$, since it is generally a higher order small quantity than the second order which we retain. In a similar way, we obtain

$$\mathbf{k}'_\beta \cdot \mathbf{k}_\beta \approx (k_\beta - k_\alpha) \hat{\mathbf{e}}_x + \mathbf{K}'_T \cdot \mathbf{K}_T \\ \mathbf{k}'_\alpha \cdot \mathbf{k}_\beta \approx (k_\alpha - k_\beta) \hat{\mathbf{e}}_x + \mathbf{K}'_T \cdot \mathbf{K}_T \\ \mathbf{k}'_\beta \cdot \mathbf{k}_\beta \approx 0 \hat{\mathbf{e}}_x + \mathbf{K}'_T \cdot \mathbf{K}_T. \quad (41)$$

The 3D Fourier transforms of the perturbations then can be approximated by

$$\begin{aligned}
\delta\rho(\mathbf{k}'_\alpha \cdot \mathbf{k}_\alpha) &= \int_0^{\Delta x} dx e^{-i(\gamma'_\alpha \cdot \gamma_\alpha)x} \int dS \delta\rho(x, \mathbf{x}_T) e^{-i(\mathbf{k}'_T \cdot \mathbf{k}_T) \cdot \mathbf{x}_T} \\
&\approx \int_0^{\Delta x} dx \delta\rho(x, \mathbf{k}'_T \cdot \mathbf{k}_T) = \delta\rho(0, \mathbf{k}'_T \cdot \mathbf{k}_T) \\
\delta\rho(\mathbf{k}'_\beta \cdot \mathbf{k}_\alpha) &\approx \int_0^{\Delta x} dx e^{-i(\mathbf{k}'_\beta \cdot \mathbf{k}_\alpha)x} \delta\rho(x, \mathbf{k}'_T \cdot \mathbf{k}_T) \\
&= \delta\rho(0, \mathbf{k}'_T \cdot \mathbf{k}_T) \eta(\Delta x) \\
\delta\rho(\mathbf{k}'_\alpha \cdot \mathbf{k}_\beta) &\approx \delta\rho(0, \mathbf{k}'_T \cdot \mathbf{k}_T) \eta^*(\Delta x) \\
\delta\rho(\mathbf{k}'_\beta \cdot \mathbf{k}_\beta) &\approx \delta\rho(0, \mathbf{k}'_T \cdot \mathbf{k}_T)
\end{aligned} \tag{42}$$

where

$$\delta\rho(0, \mathbf{K}_T) = \int_0^{\Delta x} \delta\rho(x, \mathbf{K}_T) dx \approx \Delta x \delta\rho(\mathbf{K}_T) \tag{43}$$

$$\eta(\Delta x) = \text{sinc}((k_\beta \cdot k_\alpha) \Delta x / 2) e^{\frac{-i}{2} (k_\beta \cdot k_\alpha) \Delta x} \tag{44}$$

with $\delta\rho(\mathbf{K}_T)$ as the 2D Fourier transform of $\delta\rho(x, \mathbf{x}_T)$ with respect to \mathbf{x}_T , and η^* as the complex conjugate of η . Similar expressions can be derived for $\delta\lambda$ and $\delta\mu$.

The scattered fields under this small-angle approximation become

$$\begin{aligned}
\mathbf{U}^{PP}(\mathbf{K}'_T, \mathbf{K}_T) &\approx \frac{i}{2\gamma'_\alpha} k_\alpha^2 u_\alpha^0 \hat{k}'_\alpha \\
&\times \left[\frac{\delta\rho(0, \tilde{\mathbf{K}}_T)}{\rho_0} - \frac{\delta\lambda(0, \tilde{\mathbf{K}}_T)}{\lambda_0 + 2\mu_0} - \frac{2\delta\mu(0, \tilde{\mathbf{K}}_T)}{\lambda_0 + 2\mu_0} \right] \\
&\approx -ik_\alpha \Delta x u_\alpha^0(\mathbf{K}_T) \frac{\delta\alpha(\tilde{\mathbf{K}}_T)}{\alpha_0} \hat{k}'_\alpha
\end{aligned} \tag{45}$$

$$\begin{aligned}
\mathbf{U}^{PS}(\mathbf{K}'_T, \mathbf{K}_T) &\approx \frac{i}{2\gamma'_\beta} k_\beta^2 u_\alpha^0(\mathbf{K}_T) [\hat{k}_\alpha \cdot \hat{k}'_\beta (\hat{k}_\alpha \cdot \hat{k}'_\beta)] \\
&\times \left[\frac{\delta\rho(0, \tilde{\mathbf{K}}_T)}{\rho_0} \eta(\Delta x) - 2 \left(\frac{\beta_0}{\alpha_0} \right) \frac{\delta\mu(0, \tilde{\mathbf{K}}_T)}{\mu_0} \eta(\Delta x) \right] \\
&\approx -ik_\beta \Delta x u_\alpha^0(\mathbf{K}_T) [\hat{k}_\alpha \cdot \hat{k}'_\beta (\hat{k}_\alpha \cdot \hat{k}'_\beta)] \eta(\Delta x) \\
&\times \left[\frac{\delta\beta(\tilde{\mathbf{K}}_T)}{\beta_0} + \left(\frac{2\beta_0}{\alpha_0} - 1 \right) \frac{\delta\mu(\tilde{\mathbf{K}}_T)}{\mu_0} \right]
\end{aligned} \tag{46}$$

$$\begin{aligned}
\mathbf{U}^{SP}(\mathbf{K}'_T, \mathbf{K}_T) &\approx \frac{i}{2\gamma'_\alpha} k_\alpha^2 (u_\beta^0(\mathbf{K}_T) \cdot \hat{k}'_\alpha) \hat{k}'_\alpha \\
&\times \left[\frac{\delta\rho(0, \tilde{\mathbf{K}}_T)}{\rho_0} \eta^*(\Delta x) - 2 \left(\frac{\beta_0}{\alpha_0} \right) \frac{\delta\mu(0, \tilde{\mathbf{K}}_T)}{\mu_0} \eta^*(\Delta x) \right] \\
&\approx -ik_\alpha \Delta x (u_\beta^0(\mathbf{K}_T) \cdot \hat{k}'_\alpha) \hat{k}'_\alpha \eta^*(\Delta x) \\
&\times \left[\frac{\delta\beta(\tilde{\mathbf{K}}_T)}{\beta_0} + \left(\frac{2\beta_0}{\alpha_0} - 1 \right) \frac{\delta\mu(\tilde{\mathbf{K}}_T)}{\mu_0} \right]
\end{aligned} \tag{47}$$

$$\begin{aligned}
\mathbf{U}^{SS}(\mathbf{K}'_T, \mathbf{K}_T) &\approx -\frac{i}{2\gamma'_\alpha} k_\beta^2 \Delta x [u_\beta^0(\mathbf{K}_T) \cdot \hat{k}'_\beta (u_\beta^0 \cdot \hat{k}'_\beta)] \\
&\times \left[\frac{\delta\rho(0, \tilde{\mathbf{K}}_T)}{\rho_0} - \frac{\delta\mu(0, \tilde{\mathbf{K}}_T)}{\mu_0} \right] \\
&\approx -ik_\beta \Delta x [u_\beta^0(\mathbf{K}_T) \cdot \hat{k}'_\beta (u_\beta^0 \cdot \hat{k}'_\beta)] \frac{\delta\beta(\tilde{\mathbf{K}}_T)}{\beta_0}
\end{aligned} \tag{48}$$

where $\tilde{\mathbf{K}}_T = \mathbf{K}'_T - \mathbf{K}_T$ is the horizontal exchange wavenumber and $\delta\alpha$, $\delta\beta$, are the P and S wave velocity perturbations, respectively. We see that for the non-coupling P and S scattered waves, the major contributions come from the P and S wave velocity perturbations. However, for wave-type conversion between P and S , only $\delta\beta$ and $\delta\mu$ have contributions. The cross-coupling term between two orthogonal S -components in (31) has been dropped in (48), since it is a higher order small quantity in forward scattering problems. It is known that the effect of shear modulus perturbation for S wave incidence is similar to a double-couple secondary source, which has its maximum amplitude of cross-coupling in the direction perpendicular to the incident direction [see Wu and Aki, 1985; Wu, 1989b]. For this reason, the cross-coupling can be neglected in the complex-screen formulation which is a formulation of small-angle scattering approximation. In order to treat the cross-coupling problem rigorously, we have to go back to the more accurate thin-slab formulation.

From (45) to (48) we can prove that the scattered waves are in the form of convolution integrals of the incident field and the perturbations in the wavenumber domain. Therefore in the space domain the perturbations will be local operators, similar to passing "screens". Let us take $P-P$ and $P-S$ scattering as examples to demonstrate how (45)-(48) can be related to space domain screen equations for the common-mode scattered waves and converted waves.

The space domain total P wave field can be obtained by Fourier transforming the first equation of (38). For the $P-P$ scattered field, from (45) we have

$$\begin{aligned}
\mathbf{U}^{PP}(x_1, \mathbf{x}_{1T}) &= \frac{1}{4\pi^2} \int d\mathbf{K}'_T e^{i\mathbf{K}'_T \cdot \mathbf{x}_{1T}} e^{i\gamma'_\alpha \Delta x} \\
&\times \frac{1}{4\pi^2} \int d\mathbf{K}_T \mathbf{U}^{PP}(\mathbf{K}'_T, \mathbf{K}_T) \\
&= -\frac{1}{4\pi^2} \int d\mathbf{K}'_T e^{i\mathbf{K}'_T \cdot \mathbf{x}_{1T}} e^{i\gamma'_\alpha \Delta x} ik_\alpha \hat{k}'_\alpha \\
&\times \frac{1}{4\pi^2} \int d\mathbf{K}_T u_\alpha^0(\mathbf{K}_T) \tilde{\alpha}(\mathbf{K}'_T - \mathbf{K}_T) \Delta x
\end{aligned} \tag{49}$$

where $\tilde{\alpha} = \delta\alpha/\alpha_0$ and $\Delta x = x_1 - x$. Let

$$\Phi(x, \mathbf{K}'_T) = \frac{1}{4\pi^2} \int d\mathbf{K}_T u_\alpha^0(\mathbf{K}_T) \tilde{\alpha}(\mathbf{K}'_T - \mathbf{K}_T) \Delta x$$

Then

$$\begin{aligned}
\mathbf{U}^{PP}(x_1, \mathbf{x}_{1T}) &= -\nabla_1 \Phi(x_1, \mathbf{x}_{1T}) \\
&= -2\nabla_1 \int_S dS \Phi(x, \mathbf{x}_T) \frac{\partial}{\partial x} g_p(x_1, \mathbf{x}_{1T}; x, \mathbf{x}_T) \\
&= -2\nabla_1 \int_S dS ik_\alpha \phi^0(x, \mathbf{x}_T) \tilde{\alpha}(x, \mathbf{x}_T) \Delta x \frac{\partial}{\partial x} g_p(x_1, \mathbf{x}_{1T}; x, \mathbf{x}_T)
\end{aligned} \tag{50}$$

where ∇_1 stands for the ∇ operation with respect to \mathbf{x}_1 , $\phi^0 = \frac{u_\alpha^0}{ik_\alpha}$, and g_p is the scalar Green's function with the P wave propagation speed, defined as

$$g_p(\mathbf{x}_1; \mathbf{x}) = \frac{1}{4\pi|\mathbf{x}_1 - \mathbf{x}|} \exp(ik_\alpha |\mathbf{x}_1 - \mathbf{x}|).$$

The primary field can be written as

$$\begin{aligned} \mathbf{u}_\alpha^0(\mathbf{x}_1, \mathbf{x}_{1T}) &= \frac{1}{4\pi^2} \int d\mathbf{K}_T e^{i\mathbf{K}_T \cdot \mathbf{x}_{1T}} e^{i\gamma_\alpha \Delta x} \mathbf{u}_\alpha^0(\mathbf{x}, \mathbf{K}_T) \\ &= \frac{1}{4\pi^2} \int d\mathbf{K}_T e^{i\mathbf{K}_T \cdot \mathbf{x}_{1T}} e^{i\gamma_\alpha \Delta x} ik_\alpha \hat{k}_\alpha \phi^0(\mathbf{x}, \mathbf{K}_T) \\ &= 2\nabla_1 \int_S dS \phi^0(\mathbf{x}, \mathbf{x}_T) \frac{\partial}{\partial \mathbf{x}} g_p(\mathbf{x}_1, \mathbf{x}_{1T}; \mathbf{x}, \mathbf{x}_T). \end{aligned} \quad (51)$$

Therefore the total field

$$\begin{aligned} \mathbf{u}^{PP}(\mathbf{x}_1, \mathbf{x}_{1T}) &= \mathbf{u}_\alpha^0(\mathbf{x}_1, \mathbf{x}_{1T}) + \mathbf{U}^{PP}(\mathbf{x}_1, \mathbf{x}_{1T}) \\ &= 2\nabla_1 \int_S dS \phi^0(\mathbf{x}, \mathbf{x}_T) [1 - ik_\alpha \tilde{\alpha}(\mathbf{x}, \mathbf{x}_T) \Delta x] \\ &\quad \times \frac{\partial}{\partial \mathbf{x}} g_p(\mathbf{x}_1, \mathbf{x}_{1T}; \mathbf{x}, \mathbf{x}_T). \end{aligned} \quad (52)$$

When Δx is not small, it is better to use the Rytov approximation instead of the Born approximation. After doing the Rytov transformation [see Ishimaru, 1978; Wu and Flatté, 1990], we have

$$\begin{aligned} \mathbf{u}^{PP}(\mathbf{x}_1, \mathbf{x}_{1T}) &= \frac{2}{ik_\alpha} \nabla_1 \int_S dS \mathbf{u}_\alpha^0(\mathbf{x}, \mathbf{x}_T) \exp[-ik_\alpha \tilde{\alpha}(\mathbf{x}, \mathbf{x}_T) \Delta x] \\ &\quad \times \frac{\partial}{\partial \mathbf{x}} g_p(\mathbf{x}_1, \mathbf{x}_{1T}; \mathbf{x}, \mathbf{x}_T). \end{aligned} \quad (53)$$

We can see that the term $\exp[-ik_\alpha \tilde{\alpha}(\mathbf{x}, \mathbf{x}_T) \Delta x]$ is the phase-screen term. In the case of weak distortion, the gradient of the wave field can be approximated by taking the gradient of only the phase term, resulting in

$$\begin{aligned} \mathbf{u}^{PP}(\mathbf{x}_1, \mathbf{x}_{1T}) &= 2\hat{p} \int_S dS \mathbf{u}_\alpha^0(\mathbf{x}, \mathbf{x}_T) \exp[-ik_\alpha \tilde{\alpha}(\mathbf{x}, \mathbf{x}_T) \Delta x] \\ &\quad \times \frac{\partial}{\partial \mathbf{x}} g_p(\mathbf{x}_1, \mathbf{x}_{1T}; \mathbf{x}, \mathbf{x}_T) \end{aligned} \quad (54)$$

where \hat{p} is the unit vector in the P wave propagation direction. In fact, (54) is in the form of the scalar Rayleigh integral of the second type, representing the free propagation from plane S to plane S_1 of the distorted wave field. The distortion is caused by a phase-screen with the amount of distortion given by $k_\alpha \tilde{\alpha}(\mathbf{x}, \mathbf{x}_T) \Delta x$.

For the P-S conversion, (46) can be rewritten as

$$\mathbf{U}^{PS}(\mathbf{K}'_T, \mathbf{K}_T) = ik_\beta \hat{k}'_\beta \times (\hat{k}'_\beta \times \hat{k}_\alpha) \mathbf{u}_\alpha^0(\mathbf{K}_T) \tilde{B}(\mathbf{K}'_T - \mathbf{K}_T) \Delta x \quad (55)$$

where

$$\tilde{B}(\mathbf{K}_T) = \eta(\Delta x) \left[\frac{\delta\beta(\mathbf{K}_T)}{\beta_0} + \left(\frac{2\beta_0}{\alpha_0} - 1 \right) \frac{\delta\mu(\mathbf{K}_T)}{\mu_0} \right]. \quad (56)$$

Therefore

$$\begin{aligned} \mathbf{U}^{PS}(\mathbf{x}_1, \mathbf{x}_{1T}) &= \frac{1}{4\pi^2} \int d\mathbf{K}'_T e^{i\mathbf{K}'_T \cdot \mathbf{x}_{1T}} e^{i\gamma_\beta \Delta x} \int d\mathbf{K}_T \mathbf{U}^{PS}(\mathbf{K}'_T, \mathbf{K}_T) \\ &= \frac{-ik_\beta}{4\pi^2 k_\beta^2} \int d\mathbf{K}'_T e^{i\mathbf{K}'_T \cdot \mathbf{x}_{1T}} e^{i\gamma_\beta \Delta x} (ik_\beta \hat{k}'_\beta) \times \\ &\quad \times \left[(ik_\beta \hat{k}'_\beta) \times \int d\mathbf{K}_T \mathbf{u}_\alpha^0(\mathbf{K}_T) \tilde{B}(\mathbf{K}'_T - \mathbf{K}_T) \Delta x \right] \\ &= \frac{2}{k_\beta^2} \nabla_1 \times \nabla_1 \times \int_S dS (-ik_\beta) \nabla \phi^0(\mathbf{x}, \mathbf{x}_T) \tilde{B}(\mathbf{x}, \mathbf{x}_T) \Delta x \\ &\quad \times \frac{\partial}{\partial \mathbf{x}} g_s(\mathbf{x}_1, \mathbf{x}_{1T}; \mathbf{x}, \mathbf{x}_T) \end{aligned} \quad (57)$$

where g_s is the scalar Green's function with the S wave propagation speed. We see that the P-S conversion is produced by the distortion of the curlless field $\mathbf{u}_\alpha^0 = \nabla \phi^0$ after passing through a screen $\tilde{B}(\mathbf{x}, \mathbf{x}_T)$. Since $\eta(\Delta x)$ is a complex number, we call the screen a "complex-screen".

The calculation would be inefficient in either the space domain or the wavenumber domain alone. The ideal way is to propagate in wavenumber domain, but interact with screens in space domain, and shuttle between these two domains using FFT. This is the dual-domain approach. In the following we change (45) - (48) into a dual-domain formulation.

Dual-Domain Implementation

For P-P scattering, from (53) we have the total field

$$\mathbf{u}^{PP}(\mathbf{x}_1, \mathbf{K}'_T) = \hat{k}'_\alpha e^{i\gamma_\alpha \Delta x}$$

$$\times \int d\mathbf{x}_T e^{i\mathbf{K}'_T \cdot \mathbf{x}_T} \mathbf{u}_\alpha^0(\mathbf{x}, \mathbf{x}_T) \exp[-ik_\alpha \tilde{\alpha}(\mathbf{x}, \mathbf{x}_T) \Delta x]. \quad (58)$$

It can be seen that the wave field interacts with the screen in the space domain, then is transformed back to the wavenumber domain and propagated to a new surface at \mathbf{x}_1 .

For P-S scattering, we can rewrite (57) as

$$\mathbf{U}^{PS}(\mathbf{x}_1, \mathbf{K}'_T) = -e^{i\gamma_\beta \Delta x} \hat{k}'_\beta \times [\hat{k}'_\beta \times \mathbf{u}_\alpha^{(1)}(\mathbf{x}_1, \mathbf{K}'_T)] \quad (59)$$

where

$$\mathbf{u}_\alpha^{(1)}(\mathbf{x}, \mathbf{K}'_T) = \int d\mathbf{x}_T e^{i\mathbf{K}'_T \cdot \mathbf{x}_T} \mathbf{u}_\alpha^0(\mathbf{x}, \mathbf{x}_T) C_B(\mathbf{x}, \mathbf{x}_T) \quad (60)$$

is the distorted P incident field after passing through the complex-screen:

$$\begin{aligned} C_B(\mathbf{x}, \mathbf{x}_T) &= -ik_\beta \eta(\Delta x) \int_x^1 d\mathbf{x}' \tilde{B}(\mathbf{x}', \mathbf{x}_T) \\ &\approx -ik_\beta \eta(\Delta x) \Delta x \tilde{B}(\mathbf{x}, \mathbf{x}_T). \end{aligned} \quad (61)$$

The complex-screen in (61) can be also replaced by a complex phase-screen:

$$H_B(\mathbf{x}, \mathbf{x}_T) = \exp[-ik_\beta \eta(\Delta x) \Delta x \tilde{B}(\mathbf{x}, \mathbf{x}_T)]. \quad (62)$$

This is because

$$\begin{aligned} &\frac{1}{4\pi^2} \int d\mathbf{K}'_T e^{i\mathbf{K}'_T \cdot \mathbf{x}_T} \hat{k}'_\beta \times \\ &\quad \times \left[\hat{k}'_\beta \times e^{i\gamma_\beta \Delta x} \int d\mathbf{x}_T e^{-i\mathbf{K}'_T \cdot \mathbf{x}_T} \mathbf{u}_\alpha^0(\mathbf{x}, \mathbf{x}_T) \right] \\ &= \frac{1}{k_\beta^2} \nabla_1 \times \nabla_1 \times \mathbf{u}_\alpha^0(\mathbf{x}_1, \mathbf{x}_{1T}) = 0. \end{aligned} \quad (63)$$

For computation, (59) can be also written as

$$\begin{aligned} \mathbf{U}^{PS}(x_1, \mathbf{K}'_T) &= e^{i\gamma_B \Delta x} \hat{k}'_B \\ &\times [\mathbf{u}_\alpha^{(1)}(x, \mathbf{K}'_T) \cdot \hat{k}'_B (\mathbf{u}_\alpha^{(1)}(x, \mathbf{K}'_T) \cdot \hat{k}'_B)] \quad (64) \end{aligned}$$

Theoretically, the replacement of the complex-screen $C_B(x, x_T)$ by a phase-screen $H_B(x, x_T) = \exp[C_B(x, x_T)]$ will have no effect on the $P-S$ scattered field. However, due to the finiteness of the Fourier representation of the field, the phase-screen calculation may produce larger errors than the complex-screen. In the following, we keep the conversion terms as produced by complex-screens.

In the same way, the $S-P$ scattered field can be calculated by

$$\mathbf{U}^{SP}(x_1, \mathbf{K}'_T) = e^{i\gamma_B \Delta x} \hat{k}'_B (\mathbf{u}_\beta^{(1)}(x, \mathbf{K}'_T) \cdot \hat{k}'_\alpha) \hat{k}'_\alpha \quad (65)$$

where

$$\mathbf{u}_\beta^{(1)}(x, \mathbf{K}'_T) = \int d\mathbf{x}_T e^{i\mathbf{K}'_T \cdot \mathbf{x}_T} \mathbf{u}_\beta^0(x, \mathbf{x}_T) C_B^*(x, x_T) \quad (66)$$

with

$$\begin{aligned} C_B^*(x, x_T) &= -ik_\alpha \eta^*(\Delta x) \int_x^{x_1} dx' \tilde{B}(x', x_T) \\ &\approx -ik_\alpha \eta^*(\Delta x) \Delta x \tilde{B}(x, x_T). \quad (67) \end{aligned}$$

Similar to the case of $P-S$, the complex-screen in (66) can be replaced by a complex phase-screen:

$$H_B^*(x, x_T) = \exp[-ik_\alpha \eta^*(\Delta x) \Delta x \tilde{B}(x, x_T)] \quad (68)$$

because

$$\begin{aligned} \frac{1}{4\pi^2} \int d\mathbf{K}'_T e^{i\mathbf{K}'_T \cdot \mathbf{x}_T} \hat{k}'_\alpha [\hat{k}'_\alpha \cdot e^{i\gamma_\alpha \Delta x} \int d\mathbf{x}_T e^{-i\mathbf{K}'_T \cdot \mathbf{x}_T} \mathbf{u}_\beta^0(x, \mathbf{x}_T)] \\ = \frac{1}{k_\alpha^2} \nabla_1 [\nabla_1 \cdot \mathbf{u}_\beta^0(x_1, \mathbf{x}_T)] = 0. \quad (69) \end{aligned}$$

For $S-S$ scattering, from (48) the in-plane $S-S$ scattered field can be rewritten as

$$\mathbf{U}^{SS}(x_1, \mathbf{K}'_T) = -e^{i\gamma_B \Delta x} \hat{k}'_B \times [\hat{k}'_B \times \mathbf{u}_\beta^{(2)}(x_1, \mathbf{K}'_T)] \quad (70)$$

where

$$\mathbf{u}_\beta^{(2)}(x, \mathbf{K}'_T) = \int d\mathbf{x}_T e^{i\mathbf{K}'_T \cdot \mathbf{x}_T} \mathbf{u}_\beta^0(x, \mathbf{x}_T) C_B(x, x_T) \quad (71)$$

is the distorted S incident field after passing through the complex-screen:

$$C_B(x, x_T) = -ik_B \int_x^{x_1} dx' \tilde{\beta}(x', x_T) \approx -ik_B \Delta x \tilde{\beta}(x, x_T) \quad (72)$$

where $\tilde{\beta} = \delta\beta/\beta_0$. Since the incident S wavefield can be written as

$$\begin{aligned} \mathbf{u}_\beta^0(x_1, \mathbf{K}'_T) &= -e^{i\gamma_B \Delta x} \hat{k}'_B \times [\hat{k}'_B \times \mathbf{u}_\beta^0(x_1, \mathbf{K}'_T)] \\ &= -e^{i\gamma_B \Delta x} \hat{k}'_B \times [\hat{k}'_B \times \int d\mathbf{x}_T e^{i\mathbf{K}'_T \cdot \mathbf{x}_T} \mathbf{u}_\beta^0(x, \mathbf{x}_T)]. \quad (73) \end{aligned}$$

Then the total $S-S$ field can be written as

$$\begin{aligned} \mathbf{u}^{SS}(x_1, \mathbf{K}'_T) &= \mathbf{u}_\beta^0(x_1, \mathbf{K}'_T) + \mathbf{U}^{SS}(x_1, \mathbf{K}'_T) \\ &= -e^{i\gamma_B \Delta x} \hat{k}'_B \times [\hat{k}'_B \times \int d\mathbf{x}_T e^{i\mathbf{K}'_T \cdot \mathbf{x}_T} \mathbf{u}_\beta^0(x, \mathbf{x}_T) H_B(x, \mathbf{x}_T)] \\ &= e^{i\gamma_B \Delta x} [\mathbf{u}_\beta^{(2)}(x, \mathbf{K}'_T) \cdot \hat{k}'_B (\mathbf{u}_\beta^{(2)}(x, \mathbf{K}'_T) \cdot \hat{k}'_B)] \quad (74) \end{aligned}$$

with

$$H_B(x, x_T) = \exp[C_B(x, x_T)]. \quad (75)$$

Computation Speed

Let us estimate the increase of computation speed of the complex-screen method versus the thin-slab method. From the above formulas, we see that for one step forward, the screen method needs 7 inverse 2D FFTs, one scalar for $u_\alpha(\mathbf{K}_T)$, two vectors for $\mathbf{u}_\alpha(\mathbf{K}_T)$ and $\mathbf{u}_\beta(\mathbf{K}_T)$, and 10 forward 2D FFTs, one scalar for u^{PS} , 3 vectors for \mathbf{U}^{PS} , \mathbf{U}^{SP} , and \mathbf{U}^{SS} . Each 2D FFT needs $2N^2/\log_2 N^2$ operations. In the space domain, the interaction between the wave field and the screen needs only N^2 operations. In the case of the thin-slab method, we need 5 mappings (matrix multiplications) in wavenumber domain for each step forward. Each mapping needs $N^2 \times N^2$ operations if all the wavenumbers are taken into account. Therefore the relative speed factor of the two methods is about

$$S_F = 5N^4/(17N^2 \log_2 N^2 + 10N^2).$$

When $N = 128$, $S_F = 330$, while for $N = 512$, $S_F = 4148$. For large 3D models, the complex-screen method can be 2 to 3 orders of magnitude faster than the thin-slab method. Of course, the amplitude information for large angle scattering from the complex-screen method is not as accurate as from the thin-slab method. If the scattering and propagation problem is for large-scale, smoothly varying inhomogeneous media, the complex-screen method is preferable in view of the huge gain in computational speed of the method.

Numerical Examples

To test our algorithm for the complex-screen method and to compare our method with the vector screen formulation of FM91, we present in this paper two 3D numerical examples. These examples serve only to demonstrate the principle and capability of our method. Detailed comparisons with other methods and discussion of accuracy and limitation of the method are deferred for future publications. Our formulation has a major difference from FM91. In our theory the $P-S$ and $S-P$ conversions are generated by S wave velocity perturbation and the shear modulus perturbation. For a Poisson solid, S wave velocity perturbation plays a major role for the $P-S$ and $S-P$ conversions under this parabolic approximation. In the special case of $\alpha_0 = 2\beta_0$, S wave velocity perturbation becomes the only factor. In contrast, the $P-S$ conversion of FM91 is determined by P wave velocity perturbation, while the $S-P$ conversion, by S wave velocity perturbation, which can cause nonphysical conversions. This can be seen in the following examples.

1. *The case of only P velocity perturbation.* The first example is the case in which only the Lam constant λ is perturbed. In this case, there should be no $P-S$ conversion, as correctly predicted by this theory and the scattering theory. However, from FM91, $P-S$ conversion would still be generated and no

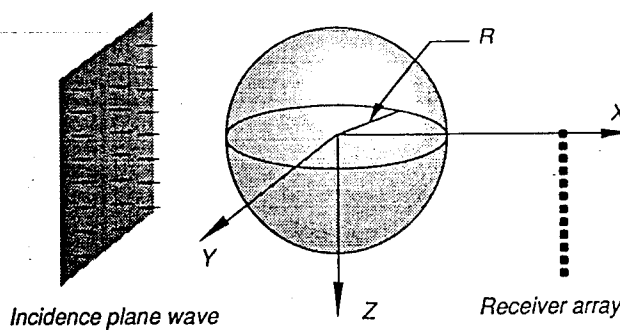


Fig. 2. The geometry of the numerical examples. A plane P wave is incident on a uniform sphere of radius R . The background velocities are P velocity α_0 , S velocity β_0 . The parameters in the two examples are (example 1) $\alpha_0 = 4.206$ km/s, $\beta_0 = 2.664$ km/s, $R = 7$ km, with 10% P velocity perturbation and (example 2) $\alpha_0 = 6.0$ km/s, $\beta_0 = 3.5$ km/s, $R = 1$ km, with 10% S -velocity perturbation.

difference could be distinguished between λ and μ perturbations. Our theory is supported by 3D finite difference calculations. The experimental geometry is shown in Figure 2. The background medium has P wave velocity of 4.206 km/s, S wave velocity of 2.664 km/s, and density of 2.14 g/cm^3 . The model is a solid sphere with 10% P velocity perturbation (a fast sphere) and no S velocity or density perturbations. The radius of the sphere is 7 km. A plane P wave is incident on the sphere along the x -axis and the receiver line parallel with z -axis is located 8 km from the center of the sphere (see Figure 2). There are 25 receivers on the receiver line with interval of 0.5 km. The source time function is of Kelly type with center frequency at 1.0 Hz. In Figure 3 a comparison between the results of 3D finite difference (FD) and the elastic complex-screen (ECS) method is shown. The 3D FD has model parameters of $nx = 128$, $ny = 96$, $nz = 96$, $dx = dy = dz = 0.25$ km, $nt = 1500$ and $dt = 0.005$ s. The calculation is performed on

the 128-node nCUBE computer at the Geophysical Center for Parallel Processing, part of the Earth Resources Laboratory of MIT by C.B. Peng. The CPU time for this example is about 29 min. Note that due to the symmetry of the problem, only one quarter of the model space is taken into FD calculation. For more general problems, no such saving of time can be achieved. The complex-screen calculation is performed on the SUN SPARC station 2 computer at the Institute of Tectonics, University of California, Santa Cruz. For this example, we use a 64×64 grid for the $y-z$ plane and variable step length in x -direction (0.5 km inside the sphere). The CPU time is less than 30 min on the SPARC station 2. In Figure 3, the distortion of the incident P wave and the diffracted P waves from the top and bottom points of the sphere are seen clearly. There are no converted S waves, consistent with the scattering theory. It is seen also that the complex-screen method agrees well with the finite difference calculation. In Figure 4a are shown ECS snapshots for the z -component of the wave field, which is composed of only scattered waves, where the generation and wave front propagation of the scattered P waves are clearly seen. In Figure 4b some of the corresponding snapshots from FD (A, $t = 1$ s; B, $t = 3$ s; C, $t = 5$ s; D, $t = 7$ s) are shown for comparison. We see that except for the lack of backscattered waves in the elastic complex-screen method, the forward wave fronts are quite similar for these two methods.

2. *The case of only S -velocity perturbation.* In this case, the major purpose is to check the $P-S$ converted waves. Since for the FD method it is difficult to separate P and S waves, we compare our results with an exact solution for a solid sphere with 10% S -velocity perturbation. The experimental geometry is similar to Figure 2, but with different parameters. The background medium has P wave velocity of 6.0 km/s, S wave velocity of 3.5 km/s, and density of 2.7 g/cm^3 . The radius of the sphere is 1 km. A plane P wave is incident on the sphere along the x -axis and the receiver line is parallel with the z -

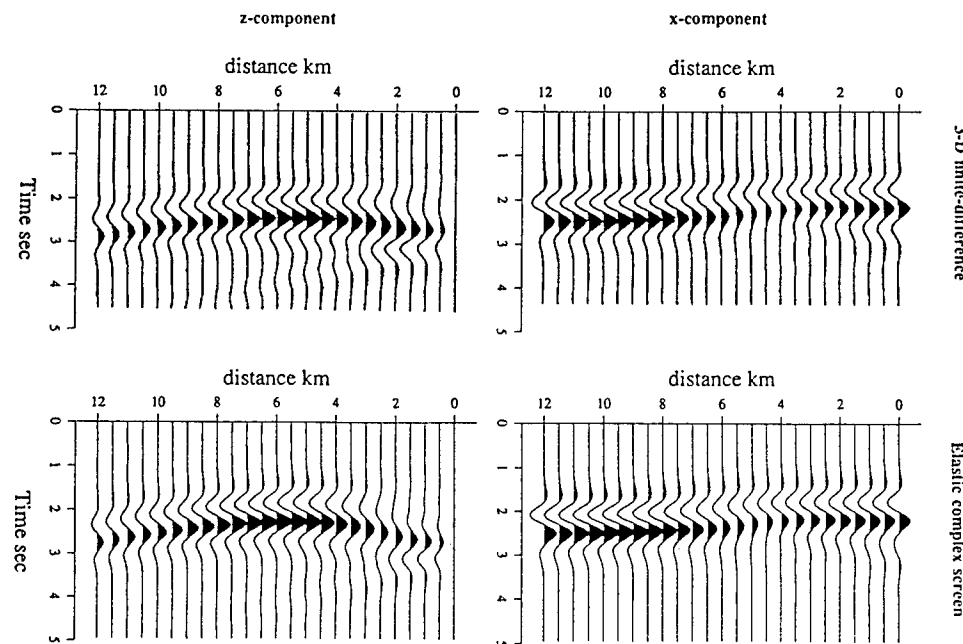


Fig. 3. Comparison of 3D elastic complex-screen (ECS) method with 3D finite difference (FD) for an elastic sphere with 10% P velocity perturbation. The receiver line is 8 km from the center of the sphere (see Fig. 2). Shown on the left are finite difference results and on the right, ECS results. The upper part are synthetic waveforms of the x -component and the lower part is for the z -component.

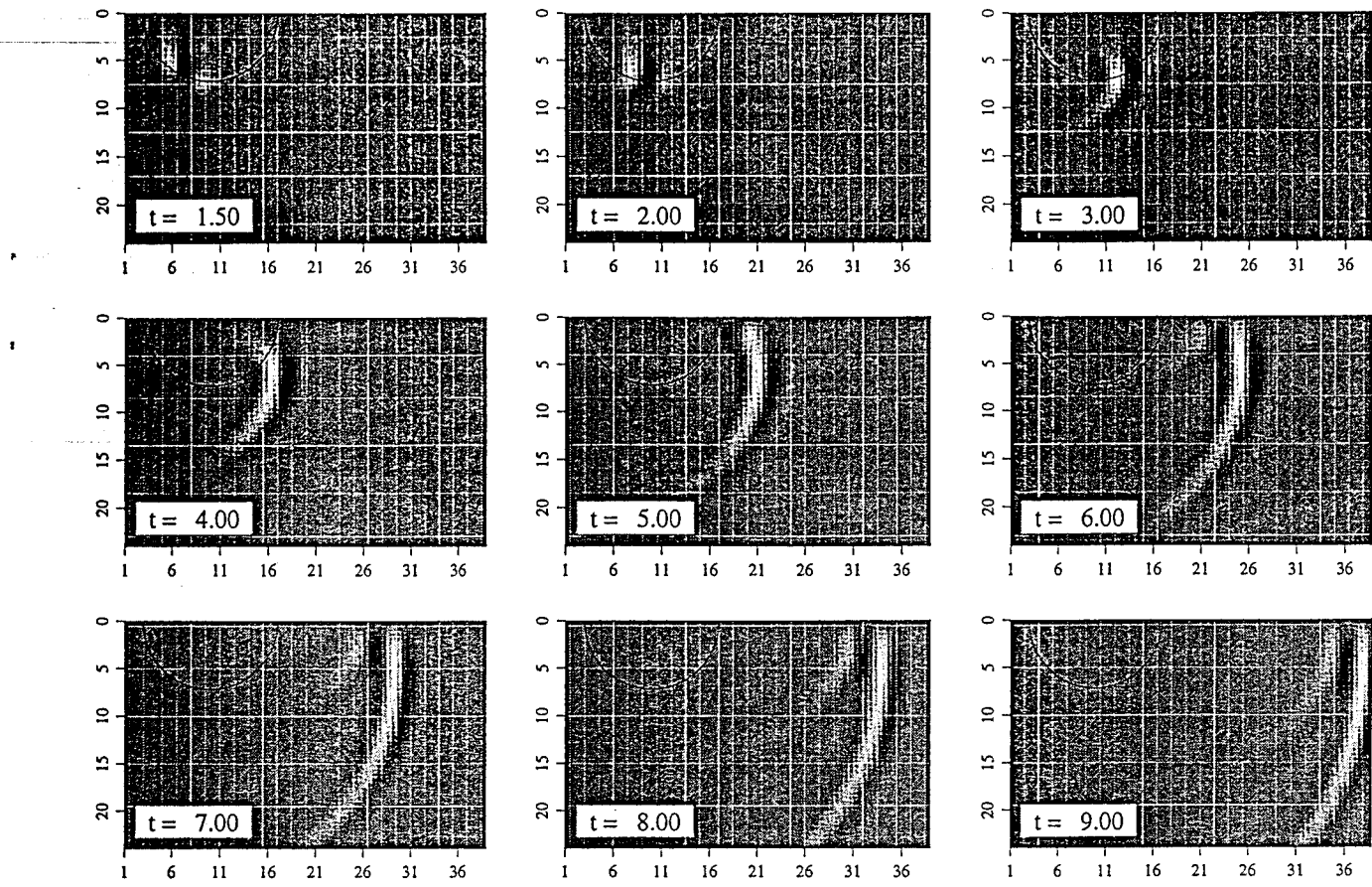


Fig. 4a. Snapshots from ECS for the z -component of scattered P waves in example 1. The position of the sphere is outlined in each snapshot. The generation and propagation of the scattered waves can be seen clearly.

axis, located 2 km from the center of the sphere (see Figure 2). There are 24 receivers on the receiver line with intervals of 0.1 km. The source time function is a Berlage impulse $f(t) = w \exp(-w/2.5) \sin w$, where $w = 2\pi f_0 t$, with center frequency f_0 at 10.0 Hz. The frequency range is from 0 to 64 Hz

with frequency interval 0.25 Hz for the exact solution, and 0.5 Hz for the complex-screen method. The exact solution is calculated using the eigenfunction expansion series [Petrashen, 1945; Ying and Truell, 1956; Korneev and Johnson, 1993] by V.A. Korneev on a Sun-Solbourne computer at the Center for

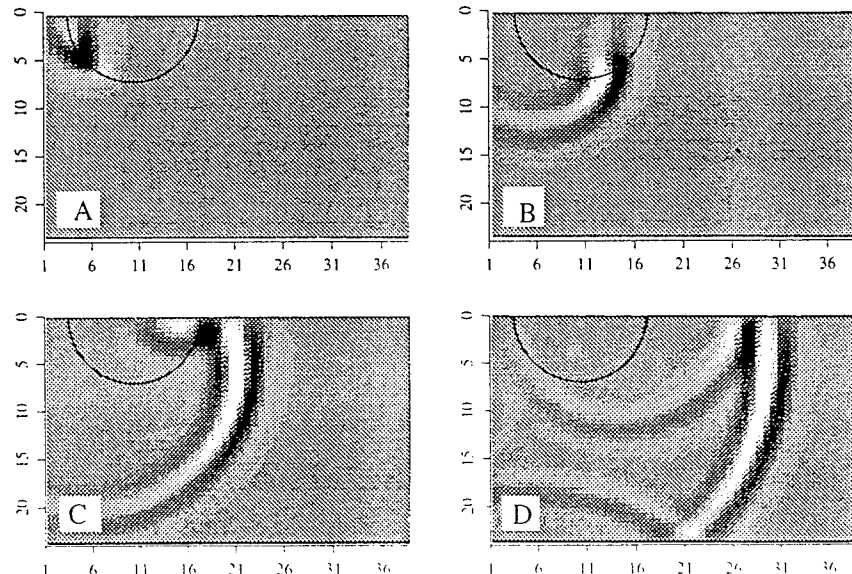


Fig. 4b. Some corresponding snapshots from FD: A, $t = 1$ s; B, $t = 3$ s; C, $t = 5$ s; D, $t = 7$ s. From comparison of Figure 4a and 4b it can be seen that except for the lack of backscattered waves in the ECS method, the forward wavefronts are quite similar for these two methods.

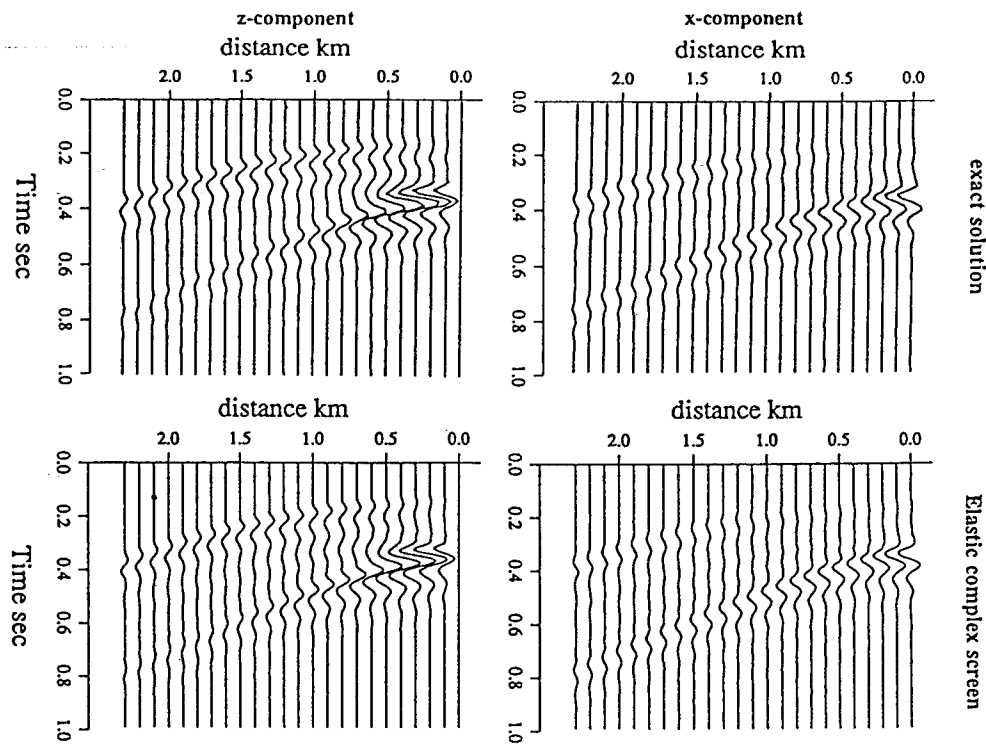


Fig. 5. Comparison of 3D elastic complex-screen (ECS) method with exact solutions for an elastic sphere with 10% S velocity perturbation. The receiver line is 2 km from the center of the sphere (see Figure 2). Showing on the left are exact solutions, and on the right, ECS results. The upper part are synthetic waveforms of the x -component and the lower part is for the z -component.

Computational Seismology, Lawrence Berkeley Laboratory, University of California, Berkeley. Both P and S scattered waves should be generated for a P wave incidence in this case. Here we compare only the $P-S$ converted waves. In Figure 5 the comparison of x - and z -components calculated by exact solution and by ECS is given. We see the two results are in very good agreement. The first S arrival is the $P-S$ scattered wave produced by the right half of the spherical surface. The second and third arrivals are the $P-S-S$ scattered waves produced by the left half of the spherical surface. We see that not only the direct $P-S$ converted waves but also the converted $P-S$ head waves can be modeled correctly by the complex-screen method. In contrast, there will be no scattered waves at all from the formulation of FM91 in this special case, showing again that the conversion is not correctly handled in their formulation.

The second difference between our complex-screen method and the vector phase-screen scheme of FM91 is that the "complex-screen" for converted waves causes not only phase distortion but also amplitude change of the incident field. The conversion coefficient is Δx dependent as a $\sin x/x$ type function. Only when Δx is much smaller than the shear wavelength does $\eta(\Delta x)$ approach a real number close to unity. We have proved that the complex-screens for converted waves can be made into complex phase-screens, but is not necessary.

For $S-S$ forward scattering under the parabolic approximation the in-plane scattered waves are generated by S wave velocity perturbations, similar to the case of $P-P$ scattering caused by P velocity perturbations. We do not test it here.

5. LIMITING CASE OF SCALAR WAVES

In the case of scalar waves, the phase-screen formulas have been derived through various approaches. The normal pro-

cedure of neglecting the higher order derivatives in the propagation direction leads to the standard PE (parabolic equation)-type phase-screen [Tappert, 1977; Flatté and Tappert, 1975; Martin and Flatté, 1988], which can be also derived by the truncated Taylor expansion of the square-root operator. Based on the symmetric splitting of the square-root operator, a wide-angle phase-screen formulation was obtained [Feit and Fleck, 1978; Thomson and Chapman, 1983], in which the square-root operator is split into a propagation term and an interaction term. The propagation term is a wide-angle free propagator, while the interaction term is a multiplication by $(n-1)$, where n is the refractive index. This wide-angle phase-screen method has better accuracy than the parabolic approximation. The other approach for improving the accuracy is to match the ray equation of the phase-screen method which is a one-way equation, with the ray equation of the two-way Helmholtz equation [Tolstoy et al., 1985; Berman et al., 1989]. In Tolstoy et al. [1985], only the interaction term is changed into $\log n$, while the propagation term remains as the standard parabolic-type propagator; in Berman et al. [1989] both the interaction and propagation terms are changed. In this section, as a limiting case of our wide-angle one-way elastic wave equations, we derive a thin-slab equation for the scalar case, which may be termed as a generalized wide-angle phase-screen equation. The equation matches the scattering in the forward direction with the two-way wave equation. The method should be more generally valid than the other phase-screen methods, since it only requires the weak scattering inside the thin slab of thickness Δx , and makes fewer approximations than the other methods. After taking the small-angle approximation for the interaction term, the thin-slab equation degenerates to the wide-angle phase-screen equation of Feit and Fleck [1978].

From equation (30) and (31), consider only the $P-P$ scattering, and set $\mu_0 = 0$, $\delta\rho = \delta\mu = 0$. The scattered displacement

field becomes

$$U(K'_T, K_T) = \frac{-ik^2}{\gamma} k' u^0(K_T) \frac{\delta\alpha}{\alpha_0} (\gamma \cdot \gamma, K'_T - K_T). \quad (76)$$

The total field is

$$u(x_1, K'_T) = e^{i\gamma\Delta x} k' \\ \times \left[u^0(x, K'_T) - i \frac{k^2}{\gamma} \int dK_T u^0(K_T) \frac{\delta\alpha}{\alpha_0} (\gamma \cdot \gamma, K'_T - K_T) \right]. \quad (77)$$

Set

$$u(K_T) = ik\hat{k}\phi(K_T)$$

where $\phi(K_T)$ is the displacement potential which satisfies the scalar wave equation, we have

$$\phi(x_1, K'_T) = e^{i\gamma\Delta x} \\ \times \left[\phi_0(x, K'_T) - i \frac{k^2}{\gamma} \int dK_T \phi_0(x, K_T) \frac{\delta\alpha}{\alpha_0} (\gamma \cdot \gamma, K'_T - K_T) \right] \\ = e^{i\gamma\Delta x} \phi_0(x, K'_T) \\ \times \left[1 - i \frac{k^2}{\gamma} \int dK_T \frac{\phi_0(x, K_T)}{\phi_0(x, K'_T)} \frac{\delta\alpha}{\alpha_0} (\gamma \cdot \gamma, K'_T - K_T) \right]. \quad (78)$$

Assuming that Δx is made up of many tiny steps, the above expression can be put into a form of phase-screen:

$$\phi(x_1, K'_T) = e^{i\gamma\Delta x} \left[\phi_0(x, K'_T) e^{-i\Delta\psi(\Delta x, K'_T)} \right] \quad (79)$$

where

$$\Delta\psi(\Delta x, K'_T) = \frac{k^2}{\gamma} \int dK_T \frac{\phi_0(x, K_T)}{\phi_0(x, K'_T)} \frac{\delta\alpha}{\alpha_0} (\gamma \cdot \gamma, K'_T - K_T) \quad (80)$$

Equations (78) and (79) are the wide-angle thin-slab formulas in the wavenumber domain. For the wave field at each wavenumber, the phase should be distorted before propagation. The amount of distortion depends on the spectrum of the heterogeneities within the slab. However, the distortion is not a local operation in the wavenumber domain. Instead, the amount of distortion of the field at one wavenumber is the summation of the contributions from the incident field at all the wavenumbers interacting with the heterogeneities. Since the interaction between the incident field and the heterogeneities is not a convolution in the wavenumber domain, the operation in space domain is not local, i.e., not a multiplication. Therefore, strictly speaking, (78) and (79) are not the standard formulas of phase-screen, but may be termed as a generalized phase-screen method. In the following we will show that under the narrow-angle approximation, these formulas approach the regular formulas of scalar phase-screen.

Following a similar procedure as for the case of P-P elastic wave scattering, (78) can be simplified using the parabolic approximation as

$$\phi(x_1, K'_T) = e^{i\gamma\Delta x} \\ \times \left[\phi_0(x, K'_T) - ik \int dK_T \phi_0(x, K_T) \tilde{\alpha}(x, K'_T - K_T) \Delta x \right] \quad (81)$$

where $\tilde{\alpha}(x, K_T)$ is the 2D Fourier transform of the slab at x . Upon transforming into the space domain we obtain a regular form of scalar phase-screen:

$$\phi(x_1, x_{1T}) = 2 \int dS \left[\phi^0(x, x_T) - ik \phi^0(x, x_T) \tilde{\alpha}(x, x_T) \Delta x \right] \\ \times \frac{\partial}{\partial x} g(x_1, x_{1T}; x, x_T) \quad (82)$$

$$\text{or} \quad \phi(x_1, x_{1T}) = 2 \int dS \phi^0(x, x_T) \exp \left[-ik \tilde{\alpha}(x, x_T) \Delta x \right] \\ \times \frac{\partial}{\partial x} g(x_1, x_{1T}; x, x_T). \quad (83)$$

Note that in the above derivation, the parabolic approximation or narrow-angle approximation is only applied to the interaction between the incident field and the heterogeneities, the free space propagation remains the wide-angle one or can be approximated by any asymptotic form. It seems arguable that these two approximations should be kept in the same order; however, these two are decoupled in some degree. The interaction, namely, the scattering process, strongly depends on the properties of the heterogeneities, mainly the smoothness and the average size of the heterogeneities. When $ka \gg 1$, where a is the average size of the heterogeneities, large-angle scattered waves have very little energy, and therefore the small-angle approximation can be applied. Of course, the scattered amplitudes of wide-angle scattered waves will carry larger errors than the small-angle ones. On the other hand, the approximation to the free propagator depends on the observation angles. The use of a wide-angle propagator will keep the correct phase (or travel time) information even though the amplitude has relatively large errors due to the small-angle approximation applied to the interaction. In fact, (83) is nearly equivalent to the wide-angle phase-screen formula of *Feit and Fleck* [Feit and Fleck, 1978; Thomson and Chapman, 1983; Wu and Huang, 1992], which has been shown to have better performance than the narrow-angle phase-screen method. However, if we want to adopt both wide-angle interaction and wide-angle propagation, the thin-slab method (78) or (79) has to be used.

6. CONCLUSION

Wide-angle one-way elastic wave propagation in arbitrarily heterogeneous media is formulated using the elastic Rayleigh integral and elastic Born scattering theory in both space domain and wavenumber domain. The wavenumber domain formulation leads to a compact solution to the one-way propagation and scattering problems. It is shown that for wide-angle scattering the scattering effects of a thin-slab cannot be equated to passage through a regular phase-screen, since the interaction between the incident wave field and the slab is not local in both the space domain and the wavenumber domain. We call this more generally valid formulation the "thin-slab" formulation. After applying the small-angle approximation, the thin-slab effect degenerates to that of an elastic complex-screen.

Compared with the scalar phase-screen, the elastic phase-screen has the following features: (1) For P-P scattering and S-S in-plane scattering, the elastic complex-screen acts as two separate scalar phase-screens for P and S waves respectively. The phase distortions are determined by the integrated P and S wave velocity perturbations respectively. (2) For P-S and S-P conversions, the screen is no longer a pure phase-screen and becomes complex (with both phase and amplitude terms); the magnitude and phase of the complex factor depend on the thickness of the thin-slab, frequency and the difference between the P and S wave velocities. Both conversions are functions of

the shear wave velocity perturbation and the shear modulus perturbation. For Poisson solids the S wave velocity perturbation plays a major role. In the special case of $\alpha_0 = 2\beta_0$, the S wave velocity perturbation becomes the only factor for both conversions. (3) For the cross-coupling between in-plane S wave and off-plane S wave, only the shear modulus perturbation $\delta\mu$ has influence. For the complex-screen method the cross-coupling term is neglected because the term is a higher order small quantity for small-angle scattering.

Comparisons with solutions from the 3D finite difference method and exact eigenfunction expansions are made for two special cases. One is for a solid sphere with only P velocity perturbation; the other is with only S velocity perturbation. The elastic complex-screen method agrees generally well with the 3D FD method and the exact solutions. Comparison of the results in this paper with that of FM91 showed that the latter method does not handle wave conversions properly, especially for the P - S conversion and the cross-coupling between differently polarized S waves.

In the limiting case of scalar waves, the derivation in this paper leads to a more generally valid new method: a scalar thin-slab method. When making the small-angle approximation to the interaction term while keeping the propagation term unchanged, the thin-slab method approaches the currently available scalar wide-angle phase-screen method.

APPENDIX A: ELASTIC WAVE GREEN'S TENSORS IN SPASE DOMAIN

For an infinite homogeneous and isotropic elastic medium, the Green's displacement tensor (dyadic) is

$$\begin{aligned} G(\mathbf{x}, \mathbf{x}') &= G_\alpha + G_\beta \\ G_\alpha &= g_\alpha \left[\hat{r}\hat{r} + \left(\frac{1}{ik_\alpha r} + \frac{1}{k_\alpha^2 r^2} \right) (\mathbf{I} - 3\hat{r}\hat{r}) \right] \\ G_\beta &= g_\beta \left[(\mathbf{I} - \hat{r}\hat{r}) + \left(\frac{1}{ik_\beta r} + \frac{1}{k_\beta^2 r^2} \right) (\mathbf{I} - 3\hat{r}\hat{r}) \right] \end{aligned} \quad (A1)$$

where $k_\alpha = \omega/\alpha_0$, $k_\beta = \omega/\beta_0$, $r = |\mathbf{x} - \mathbf{x}'|$, $\hat{r} = (\mathbf{x} - \mathbf{x}')/r$, $\alpha_0 = \sqrt{(\lambda_0 + 2\mu_0)/\rho_0}$, and $\beta_0 = \sqrt{\mu_0/\rho_0}$ are the P and S wave propagation speeds in the background medium, respectively, and

$$\begin{aligned} g_\alpha &= \frac{1}{4\pi\rho_0\alpha_0^2 r} \exp(ik_\alpha r) \\ g_\beta &= \frac{1}{4\pi\rho_0\beta_0^2 r} \exp(ik_\beta r). \end{aligned} \quad (A2)$$

The gradient of Green's displacement tensor (triadic)

$$\begin{aligned} \nabla' G(\mathbf{x}, \mathbf{x}') &= \nabla' G_\alpha + \nabla' G_\beta \\ \nabla' G_\alpha &= -g_\alpha \left[ik_\alpha \hat{r}\hat{r}\hat{r} - \frac{1}{r} \mathbf{A} + 3 \left(\frac{1}{ik_\alpha r^2} + \frac{1}{k_\alpha^2 r^3} \right) \mathbf{B} \right] \\ \nabla' G_\beta &= -g_\beta \left[ik_\beta \hat{r} (\mathbf{I} - \hat{r}\hat{r}) + \frac{1}{r} \mathbf{C} - 3 \left(\frac{1}{ik_\beta r^2} + \frac{1}{k_\beta^2 r^3} \right) \mathbf{B} \right] \end{aligned} \quad (A3)$$

with

$$\begin{aligned} \mathbf{A} &= 6\hat{r}\hat{r}\hat{r} - \hat{r}\mathbf{I} - \hat{e}_i \hat{r}\hat{e}_i - \mathbf{I}\hat{r} \\ \mathbf{B} &= 5\hat{r}\hat{r}\hat{r} - \hat{r}\mathbf{I} - \hat{e}_i \hat{r}\hat{e}_i - \mathbf{I}\hat{r} \\ \mathbf{C} &= 6\hat{r}\hat{r}\hat{r} - 2\hat{r}\mathbf{I} - \hat{e}_i \hat{r}\hat{e}_i - \mathbf{I}\hat{r} \end{aligned} \quad (A4)$$

where

$$\hat{e}_i \hat{e}_i = \sum_{i=1}^3 \hat{e}_i \hat{e}_i = \mathbf{I}.$$

Note that $\nabla' G(\mathbf{x}, \mathbf{x}') = -\nabla G(\mathbf{x}, \mathbf{x}')$.

Green's strain tensor (triadic):

$$\mathbf{E}'(\mathbf{x}, \mathbf{x}') = \frac{1}{2} \left[\nabla' G + (\nabla' G)^{213} \right] = E'_\alpha + E'_\beta$$

$$E'_\alpha = \nabla' G_\alpha$$

$$E'_\beta = g_\beta$$

$$\times \left[\frac{-ik_\beta}{2} (\hat{r}\mathbf{I} + \hat{e}_i \hat{r}\hat{e}_i - 2\hat{r}\hat{r}\hat{r}) + \frac{1}{r} \mathbf{D} - 3 \left(\frac{1}{ik_\beta r^2} + \frac{1}{k_\beta^2 r^3} \right) \mathbf{B} \right] \quad (A5)$$

with

$$\mathbf{D} = \frac{1}{2} (12\hat{r}\hat{r}\hat{r} - 3\hat{r}\mathbf{I} - 3\hat{e}_i \hat{r}\hat{e}_i - 2\mathbf{I}\hat{r}). \quad (A6)$$

Green's traction tensor:

$$\Sigma_n(\mathbf{x}, \mathbf{x}') = \lambda(\mathbf{x}) \hat{n} \cdot (\nabla \cdot G(\mathbf{x}, \mathbf{x}')) + 2\mu(\mathbf{x}) \hat{n} \cdot \mathbf{E}(\mathbf{x}, \mathbf{x}') = \Sigma_{n\alpha} + \Sigma_{n\beta}$$

$$\begin{aligned} \Sigma_{n\alpha} &= g_\alpha k_\alpha \left\{ i[\lambda \hat{n}\hat{r} + 2\mu(\hat{n} \cdot \hat{r})\hat{r}\hat{r}] + \frac{1}{k_\alpha r} [-\lambda \hat{n}\hat{r} - 2\mu \mathbf{A}_n] \right. \\ &\quad \left. - \left(\frac{1}{i(k_\alpha r)^2} + \frac{1}{(k_\alpha r)^3} \right) [6\lambda \hat{n}\hat{r} - 6\mu \mathbf{B}_n] \right\} \end{aligned}$$

$$\begin{aligned} \Sigma_{n\beta} &= g_\beta k_\beta \left\{ i[2\mu[(\hat{n} \cdot \hat{r})\mathbf{I} + \hat{r}\hat{n} - 2(\hat{n} \cdot \hat{r})\hat{r}\hat{r}] + \frac{1}{k_\beta r} [-2\lambda \hat{n}\hat{r} + 2\mu \mathbf{D}_n] \right. \\ &\quad \left. + \left(\frac{1}{i(k_\beta r)^2} + \frac{1}{(k_\beta r)^3} \right) [6\lambda \hat{n}\hat{r} - 6\mu \mathbf{B}_n] \right\} \end{aligned} \quad (A7)$$

with

$$\mathbf{A}_n = \hat{n} \cdot \mathbf{A} = 6(\hat{n} \cdot \hat{r})\hat{r}\hat{r} - (\hat{n} \cdot \hat{r})\mathbf{I} \cdot \hat{r}\hat{n} - \hat{n}\hat{r}$$

$$\mathbf{B}_n = \hat{n} \cdot \mathbf{B} = 5(\hat{n} \cdot \hat{r})\hat{r}\hat{r} - (\hat{n} \cdot \hat{r})\mathbf{I} \cdot \hat{r}\hat{n} - \hat{n}\hat{r}$$

$$\mathbf{D}_n = \hat{n} \cdot \mathbf{D} = \frac{1}{2} [12(\hat{n} \cdot \hat{r})\hat{r}\hat{r} - 3(\hat{n} \cdot \hat{r})\mathbf{I} \cdot 3\hat{r}\hat{n} - 2\hat{n}\hat{r}]. \quad (A8)$$

APPENDIX B: ELASTIC WAVE GREEN'S TENSORS IN WAVENUMBER DOMAIN

In homogeneous media, Green's displacement tensor can be expressed as

$$G(\mathbf{x}, \mathbf{x}') = \frac{1}{\rho\omega^2} \left[(k_\beta^2 \mathbf{I} + \nabla \nabla) g_p(\mathbf{x}, \mathbf{x}') - \nabla \nabla g_p(\mathbf{x}, \mathbf{x}') \right] \quad (B1)$$

where

$$g_p(\mathbf{x}, \mathbf{x}') = \frac{1}{4\pi r} \exp(ik_\alpha r)$$

$$g_s(\mathbf{x}, \mathbf{x}') = \frac{1}{4\pi r} \exp(ik_\beta r) \quad (B2)$$

with $k_\alpha = \omega/\alpha$ and $k_\beta = \omega/\beta$.

In the wavenumber domain, we know from the Weyl integral

$$\begin{aligned}
g_p(x, x') &= \frac{i}{8\pi^2} \int dK_T \frac{1}{\gamma_\alpha} e^{i\gamma_\alpha(x-x')} e^{iK_T^*(x_T-x'_T)} \\
&= \frac{i}{8\pi^2} \int dK_T \frac{1}{\gamma_\alpha} e^{ik_\alpha^* r} \\
g_s(x, x') &= \frac{i}{8\pi^2} \int dK_T \frac{1}{\gamma_\beta} e^{i\gamma_\beta(x-x')} e^{iK_T^*(x_T-x'_T)} \\
&= \frac{i}{8\pi^2} \int dK_T \frac{1}{\gamma_\beta} e^{ik_\beta^* r}
\end{aligned} \tag{B3}$$

where $r = x - x'$, $k_\alpha = \gamma_\alpha \hat{e}_x + K_T$, $k_\beta = \gamma_\beta \hat{e}_x + K_T$, and

$$\gamma_\alpha = \sqrt{k_\alpha^2 - K_T^2}, \quad \gamma_\beta = \sqrt{k_\beta^2 - K_T^2}. \tag{B4}$$

From (B3) we derive the gradients of g_p and g_s :

$$\begin{aligned}
\nabla g_p &= \frac{i}{8\pi^2} \int dK_T \frac{1}{\gamma_\alpha} e^{ik_\alpha^* r} \\
\nabla \nabla g_p &= \frac{i}{8\pi^2} \int dK_T \frac{-k_\alpha k_\alpha}{\gamma_\alpha} e^{ik_\alpha^* r} \\
\nabla \nabla g_s &= \frac{i}{8\pi^2} \int dK_T \frac{-k_\beta k_\beta}{\gamma_\beta} e^{ik_\beta^* r}
\end{aligned} \tag{B5}$$

then Green's displacement tensor,

$$\begin{aligned}
G_\alpha(x, x') &= \frac{ik_\alpha^2}{8\pi^2 \rho \omega^2} \int dK_T \hat{k}_\alpha \hat{k}_\alpha \frac{1}{\gamma_\alpha} e^{ik_\alpha^* r} \\
G_\beta(x, x') &= \frac{ik_\beta^2}{8\pi^2 \rho \omega^2} \int dK_T (I - \hat{k}_\beta \hat{k}_\beta) \frac{1}{\gamma_\beta} e^{ik_\beta^* r}
\end{aligned} \tag{B6}$$

its gradients,

$$\begin{aligned}
\nabla' G_\alpha(x, x') &= \frac{k_\alpha^3}{8\pi^2 \rho \omega^2} \int dK_T \hat{k}_\alpha \hat{k}_\alpha \hat{k}_\alpha \frac{1}{\gamma_\alpha} e^{ik_\alpha^* r} \\
\nabla' G_\beta(x, x') &= \frac{k_\beta^3}{8\pi^2 \rho \omega^2} \int dK_T \hat{k}_\beta (I - \hat{k}_\beta \hat{k}_\beta) \frac{1}{\gamma_\beta} e^{ik_\beta^* r} \\
\nabla \cdot G_\alpha(x, x') &= -\frac{k_\alpha^3}{8\pi^2 \rho \omega^2} \int dK_T \hat{k}_\alpha \frac{1}{\gamma_\alpha} e^{ik_\alpha^* r} \\
\nabla \cdot G_\beta(x, x') &= 0
\end{aligned} \tag{B7}$$

and Green's stress tensor,

$$\begin{aligned}
\Sigma(x, x') &= \lambda I (\nabla \cdot G) + \mu [\nabla G + (\nabla G)^{213}] \\
\Sigma^\alpha(x, x') &= -\frac{k_\alpha^3}{8\pi^2 \rho \omega^2} \int dK_T [\lambda I \hat{k}_\alpha + 2\mu \hat{k}_\alpha \hat{k}_\alpha \hat{k}_\alpha] \frac{1}{\gamma_\alpha} e^{ik_\alpha^* r} \\
\Sigma^\beta(x, x') &= -\frac{k_\beta^3}{8\pi^2 \rho \omega^2} \int dK_T \mu [\hat{k}_\beta I + \hat{e}_i \hat{k}_\beta \hat{e}_i + 2\hat{k}_\beta \hat{k}_\beta \hat{k}_\beta] \\
&\quad \times \frac{1}{\gamma_\beta} e^{ik_\beta^* r}
\end{aligned} \tag{B8}$$

Green's traction tensor on the surface perpendicular to the x axis with normal along the positive x direction ($\hat{e}_x = -\hat{n}$) is

$$\begin{aligned}
\Sigma_x^\alpha(x, x') &= -\frac{k_\alpha^3}{8\pi^2 \rho \omega^2} \int dK_T [\lambda \hat{e}_x \hat{k}_\alpha + 2\mu (\hat{e}_x \cdot \hat{k}_\alpha) \hat{k}_\alpha \hat{k}_\alpha] \\
&\quad \times \frac{1}{\gamma_\alpha} e^{ik_\alpha^* r} \\
\Sigma_x^\beta(x, x') &= -\frac{k_\beta^3}{8\pi^2 \rho \omega^2} \int dK_T \mu [(\hat{e}_x \cdot \hat{k}_\beta) I + \hat{k}_\beta \hat{e}_x + 2(\hat{e}_x \cdot \hat{k}_\beta) \hat{k}_\beta \hat{k}_\beta] \\
&\quad \times \frac{1}{\gamma_\beta} e^{ik_\beta^* r}.
\end{aligned} \tag{B9}$$

Acknowledgments. I am grateful to T. Lay, B.L.N. Kennett, and X.B. Xie for discussions, suggestions, and encouragement. The programming help from X.B. Xie is greatly appreciated. The two reviewers and the associate editor gave me many useful suggestions. The three-dimensional finite difference examples are run by C.B. Peng on the nCUBE computer at the Geophysical Center for Parallel Processing, part of the Earth Resources Laboratory of MIT. The examples of exact solution are provided by V.A. Korneev at the Center for Computational Seismology, Lawrence Berkeley Laboratory, UCB. C.B. Peng and V.A. Korneev's help and contributions to this work are invaluable and gratefully acknowledged. The work was supported by the Airforce Office of Scientific Research through contract F49620-92-J-0461 administered by the Phillips Laboratory of the Air Force and by the W.M. Keck Foundation. Institute of Tectonics, University of California, contribution 183.

REFERENCES

- Aki, K., and P.G. Richards, *Quantitative Seismology: Theory and Methods*, vol. 1 and 2, W.H. Freeman, New York, 1980.
- Berman, D.H., E.B. Wright, and R.N. Baer, An optimal PE-type wave equation, *J. Acoust. Soc. Am.*, 86, 228-233, 1989.
- Collins, M.D., A higher-order parabolic equation for wave propagation in an ocean overlying an elastic bottom, *J. Acoust. Soc. Am.*, 86, 1459-1464, 1989.
- Collins, M.D., Higher-order Pade approximations for accurate and stable elastic parabolic equations with application to interface wave propagation, *J. Acoust. Soc. Am.*, 89, 1050-1057, 1991.
- Feit, M.D., and J.A. Fleck, Jr., Light propagation in graded-index optical fibers, *Appl. Opt.*, 17, 3990-3998, 1978.
- Fisk, M.D., and G.D. McCartor, The phase screen method for vector elastic waves, *J. Geophys. Res.*, 96, 5985-6010, 1991.
- Fisk, M.D., E.E. Charrette, and G.D. McCartor, A comparison of phase screen and finite difference calculations for elastic waves in random media, *J. Geophys. Res.*, 97, 12,409-12,423, 1992.
- Flatte, S.M., and F.D. Tappert, Calculation of the effect of internal waves on oceanic sound transmission, *J. Acoust. Soc. Am.*, 58, 1151-1159, 1975.
- Frankel, A., A review of numerical experiments on seismic wave scattering, in *Scattering and Attenuation of Seismic Waves, Part II*, edited by R.S. Wu K. and Aki, pp. 639-686, Birkhauser Verlag, Basel, 1989.
- Frazer, L.N., Dynamic elasticity of microbedded and fractured rocks, *J. Geophys. Res.*, 95, 4821-4831, 1990.
- Greene, R.R., The rational approximation to the wave equation with bottom interaction, *J. Acoust. Soc. Am.*, 76, 1764-1773, 1984.
- Greene, R.R., A high-angle one-way wave equation for seismic wave propagation along rough and sloping interfaces, *J. Acoust. Soc. Am.*, 77, 1991-1998, 1985.
- Guberman, J.E., E. Domany, J.A. Krumbholz, and M. Huberman, The Born approximation in the theory of the scattering of elastic waves by flaws, *J. Appl. Phys.*, 48, 2812-2819, 1977.
- Hudson, A., A parabolic approximation for elastic waves, *Wave Motion*, 2, 207-214, 1980.
- Ishimaru, A., *Wave propagation and scattering in random media*, vol. 1, Academic Press, New York, 1978.
- Kennett, B.L.N., *Seismic Wave Propagation in Stratified Media*, Cambridge University Press, New York, 1983.
- Korneev, V.A. and L.R. Johnson, Scattering of elastic waves by a spherical inclusion, I. Theory and numerical results, *Geophys. J. Int.*, in press, 1993.

Landers, T., and J. F. Claerbout, Numerical calculation of elastic waves in laterally inhomogeneous media, *J. Geophys. Res.*, **77**, 1476-1482, 1972.

Martin, J.M., and S.M. Flatté, Intensity images and statistics from numerical simulation of wave propagation in 3-D random media, *Appl. Opt.*, **17**, 2111-2126, 1988.

McCoy, J. J., A parabolic theory of stress wave propagation through inhomogeneous linearly elastic solids, *J. Appl. Mech.*, **44**, 462-468, 1977.

Pao, Y. H., and V. Varatharajulu, Huygen's principle, radiation conditions and integral formulas for the scattering of elastic waves, *J. Acoust. Soc. Am.*, **59**, 1361-1371, 1976.

Petrashev, G.I., Solution of vector boundary problem of mathematical physics in the case of a sphere (in Russian), *Dokl. Acad. Nauk USSR*, **46**, no. 7, 1945.

Stoffa, P.L., J.T. Fokkema, R.M.D. Freire, and W.P. Kessinger, Split-step Fourier migration, *Geophysics*, **55**, 410-421, 1990.

Tappert, F.D., The parabolic equation method, in *Wave Propagation and Underwater Acoustics*, edited by Keller and Papadakis, Springer, New York, 1977.

Thomson, D.J., and N.R. Chapman, A wide-angle split-step algorithm for the parabolic equation, *J. Acoust. Soc. Am.*, **74**, 1848-1854, 1983.

Tolstoy, A., D.H. Berman, and E.R. Franchi, Ray theory versus the parabolic equation in a long-range ducted environment, *J. Acoust. Soc. Am.*, **78**, 176-189, 1985.

Ursin, B., Review of elastic and electromagnetic wave propagation in horizontally layered media, *Geophysics*, **48**, 1063-1081, 1983.

Wales, S.C., A vector parabolic equation model for elastic propagation, in *Ocean Seismo-Acoustics*, edited by Akal and Berkson, Plenum, New York, 1986.

Wales, S.C., and J.J. McCoy, A comparison of parabolic wave theories for linearly elastic solids, *Wave Motion*, **5**, 99-113, 1983.

Wapenaar, C.P.A., and A.J. Berkhouw, *Elastic Wave Field Extrapolation*, Elsevier, New York, 1989.

Wetton, B.T.R., and G.H. Brooke, One-way wave equations for seismoacoustic propagation in elastic waveguides, *J. Acoust. Soc. Am.*, **87**, 624-632, 1990.

Wu, R.S., Representation integrals for elastic wave propagation containing either the displacement term or the stress term alone, *Phys. Rev. Lett.*, **62**, 497-500, 1989a.

Wu, R.S., The perturbation method for elastic wave scattering, in *Seismic Wave Scattering and Attenuation*, edited by R.S. Wu and K. Aki, *Pure Appl. Geophys.*, **131**, 605-637, 1989b.

Wu, R.S., and K. Aki, Scattering characteristics of waves by an elastic heterogeneity, *Geophysics*, **50**, 582-595, 1985.

Wu, R.S., and S.M. Flatté, Transmission fluctuations of seismic waves across seismic arrays, in "Seismic Wave Scattering and Attenuation" ed. by Wu and Aki, *Pure and Applied Geophys.*, **132**, 175-196, 1990.

Wu, R.S., and L.J. Huang, Scattered field calculation in heterogeneous media using phase-screen propagator, *Expanded Abstracts of the Technical Program, SEG 62nd Annual Meeting*, pp. 1289-1292, 1992.

Ying, C.F., and R. Truell, Scattering of a plane longitudinal wave by a spherical obstacle in an isotropically elastic solid, *J. Appl. Phys.*, **27**, 1086-1097, 1956.

R.-S. Wu, Institute of Tectonics, University of California, Santa Cruz, CA 95064.

(Received November 23, 1992;
revised July 7, 1993;
accepted August 31, 1993.)

A Comparison between Phase Screen, Finite Difference, and Eigenfunction Expansion Calculations for Scalar Waves in Inhomogeneous Media

by Yin-Bin Liu and Ru-Shan Wu

Abstract Phase screen, fourth-order finite difference (FD), and eigenfunction expansion calculations of scalar wave propagation in two-dimensional (2D) inhomogeneous media are compared to assess the accuracy of the phase screen method. The phase screen method is a forward propagation (one-way wave) algorithm. The finite difference and eigenfunction expansion calculations, which are solutions of full wave equation, are chosen as references in this study. Comparison of synthetic seismograms by phase screen and finite difference methods is made for four kinds of models: (1) multi-uniform-cylinder model, (2) Gaussian random media, (3) exponential random media, and (4) flicker-noise random media. Results show good agreement for weak random media (velocity perturbations $\leq 10\%$). For discrete heterogeneities, such as the multi-uniform-cylinder model, the results agree well for up to 50% deviation in velocities. The computer CPU time of the phase screen program for a problem of grid size 1024 by 512 is 367 sec in a SUN SPARC station II, about 57 times faster than the FD program we used. For large 3D problems the time saved is expected to be much greater. For a single cylinder scatterer with and without absorption, we compare synthetic seismograms by the phase screen method and by the eigenfunction expansion method (exact solution). The agreement between the two methods demonstrates that the phase screen method can also give good results for inhomogeneous absorbing media.

Introduction

Wave propagation in inhomogeneous media has been extensively studied (Chernov, 1960; Tatarskii, 1961; Ishimaru, 1978; Wu and Aki, 1985, 1988, 1989, 1990). In theoretical studies, weak scattering approximations are assumed in many cases to make the problems tractable. For wave propagation in highly heterogeneous media, however, weak scattering approximations may not be applicable. Various numerical techniques, such as finite difference, finite element methods, and phase screen and other one-way propagation methods, are used in this case to produce synthetic seismograms.

The finite difference method can produce a full solution of the wave equation (including converted, diffracted, and normal modes). Unlike various high-frequency approximations (WKBJ, ray method), there is, in principle, no limitation on the ratio of scatterer size to wavelength, if the discretization is chosen appropriately. The basic restriction to this method is the speed and memory size of the computer. Given the grid size constraint imposed by the computer speed and memory, the

accuracy and stability considerations limit the number of wavelengths contained in the grid. So the CPU time and memory size consideration often prohibit the use of finite difference technique for many outstanding problems in seismology.

The method of "phase screen" is used as a one-way propagation method in problems involving wave propagation in smoothly inhomogeneous media. This method has been extensively used to study light transmission through the atmosphere (Ratcliffe, 1956; Mercier, 1962; Martin and Flatté, 1988), light signals in optical fibers (Feit and Fleck, 1978), radio signals through the ionosphere (Buckley, 1975; Bramley, 1977; Knepp, 1983), acoustic waves in the ocean (Flatté *et al.*, 1979; Thomson and Chapman, 1983; Thomson, 1990), and seismic waves in the earth (Stoffa *et al.*, 1990; Wu and Huang, 1992). Recently, there are efforts to extend the phase screen method to elastic wave propagation (Fisk and McCartor, 1991, 1993; Fisk *et al.*, 1992; Wu, 1994). This one-way propagation method neglects all the backscattered waves, which

should be small compared with the forward scattered waves for large scatters or smoothly heterogeneous media, but retains all the multiple forward scattered waves. Therefore, the method can model all the forward multiple scattering phenomena, including focusing and defocusing, diffraction and interference, multi-pathing, *etc.*, with a tremendous saving of computation time and data storage.

Calculating the propagation and scattering of acoustic and elastic waves by irregularly shaped objects in an exact manner is either impossible or extremely difficult (Malischewsky, 1987). However, for some simple shapes of scatterers, such as cylinders and spheres, exact solutions have been given by solving the wave equation and matching the boundary conditions (Pao and Mow, 1973; Stanton, 1988). In order to assess the accuracy of the phase screen method for absorbing media, we choose the acoustic wave scattering by an absorbing circular fluid cylinder as the reference solution.

Numerical Methods and Algorithms

Phase Screen Method

For an isotropic acoustic inhomogeneous media with propagation velocity $v(\mathbf{x})$, the displacement field $\mathbf{u}(\mathbf{x})$ satisfies the wave equation (e.g., Wu and Huang, 1992)

$$\nabla^2 \mathbf{U} = -\frac{\omega^2}{v^2(\mathbf{x})} \mathbf{u}, \quad (1)$$

with

$$v(\mathbf{x}) = v_0 + \delta v(\mathbf{x}),$$

where v_0 is the background velocity, $\delta v(\mathbf{x})$ represents the velocity perturbation relative to v_0 , ∇^2 is the Laplacian, and ω is the angular frequency of the wave field. A time factor of $e^{-i\omega t}$ and a 2D Cartesian geometry are assumed.

In the phase screen method, the effect of the velocity perturbation (absorbing media corresponding to complex velocity) within a thin slab of thickness Δz is treated by multiplying the incident wave field by position-dependent (in the 2D case, x -dependent) phase factors $e^{i\Delta}$ where

$$\Delta(x, \Delta z) = \frac{\omega}{v_0} \int_0^{\Delta z} dz \frac{\delta v(x)}{v_0}. \quad (2)$$

Here, we assume the wave is propagating in the z direction (for derivation of the phase screen method see Thomson and Chapman, 1983; Wu and Huang, 1992; Wu, 1994).

The phase screen algorithm for scalar waves may be summarized as follows for the 2D case: (1) given a 2D grid of velocity distribution, the medium can be equated to a series of phase screens; (2) the displacement field in the space domain along the x axis is transformed by

FFT to wavenumber domain and propagated to the next screen in the z direction; (3) the displacement field is transformed by IFFT back to space domain and multiplied by the screen factor; (4) the procedures of (2) and (3) are repeated for all screens until the observation line is reached.

Criteria for Phase Screen Applications. The application of the phase screen method generally requires that the screen interval satisfies the following criteria (Wu, 1988): first, the weak scattering approximations must be satisfied for each screen. Second, the scattering is predominantly of small-angle scattering in the forward direction which requires $ka > 1$, where a is the scale length of heterogeneities, $k = \omega/v_0$ is the wavenumber. Finally, the geometrical optics treatment of propagation between screens is valid, i.e., $\Lambda = \Delta z/ka^2 < 1$, where Λ is the diffraction parameter and Δz is the screen interval.

The computer program used in this study is modified from Wu and Huang (1992) to include the case of absorbing heterogeneous media.

Finite Difference Method

The finite difference method solves equation (1) numerically by replacing the derivatives in space and time by finite difference approximations. The real velocity v is a function of position. At present there is no efficient scheme for using the finite difference method to solve wave equations in heterogeneous absorbing media.

It is well known that the finite difference method has numerical grid dispersion and stability problems. These problems are caused by the discrepancy between the finite difference and analytical representations of both spatial and time derivatives. For a given frequency and model velocity distribution, this discrepancy can be reduced by decreasing the sampling intervals of both space and time. However, the reduction of sampling intervals will drastically increase the number of mesh points in representing the wave field in the spatial and time domain and thus requires substantially more core memory and computation time. A reasonable compromise is that at least five nodes per shortest wavelength are needed for a fourth-order finite difference code. The time sampling interval can then be obtained by the usual spectral analysis. The stability criterion can be stated as (Alford *et al.*, 1974)

$$\frac{v_{\max} dt}{dx} < \sqrt{\frac{3}{8}}, \quad (3)$$

where v_{\max} is the maximum velocity in the model and dx and dt are the spatial and temporal sampling intervals, respectively.

Boundary Conditions. Boundary conditions have to be applied to the four edges of the model. Three types of

boundary conditions exist. The first is Dirichlet or rigid surface condition. It requires that the displacement wave field at boundary by zero, i.e., $u_x = u_z = 0$. The second type is the stress-free condition, which may sometimes be called the Neumann or free-surface condition. The third type is the radiation condition, which may also be called the absorbing boundary or transparent condition. It makes the boundary transparent for incident waves. In this study we choose the absorbing boundary condition given by Clayton and Engquist (1977) for the four edges. The absorbing boundary condition can perfectly absorb the incident wave perpendicular to the boundary, but only

partially absorb obliquely incident waves. In order to reduce the boundary effects, we enlarge the model size so that reflected waves from the artificial boundaries come much later than the waves of interest.

The finite difference code used in this study is fourth order in space and second order in time, developed by Dr. X. B. Xie based on Alford *et al.* (1974).

Exact Solution of a Circular Cylinder

The scattering of acoustic and elastic waves by a cylinder inclusion has drawn the attention of a number of authors in connection with acoustics and seismology

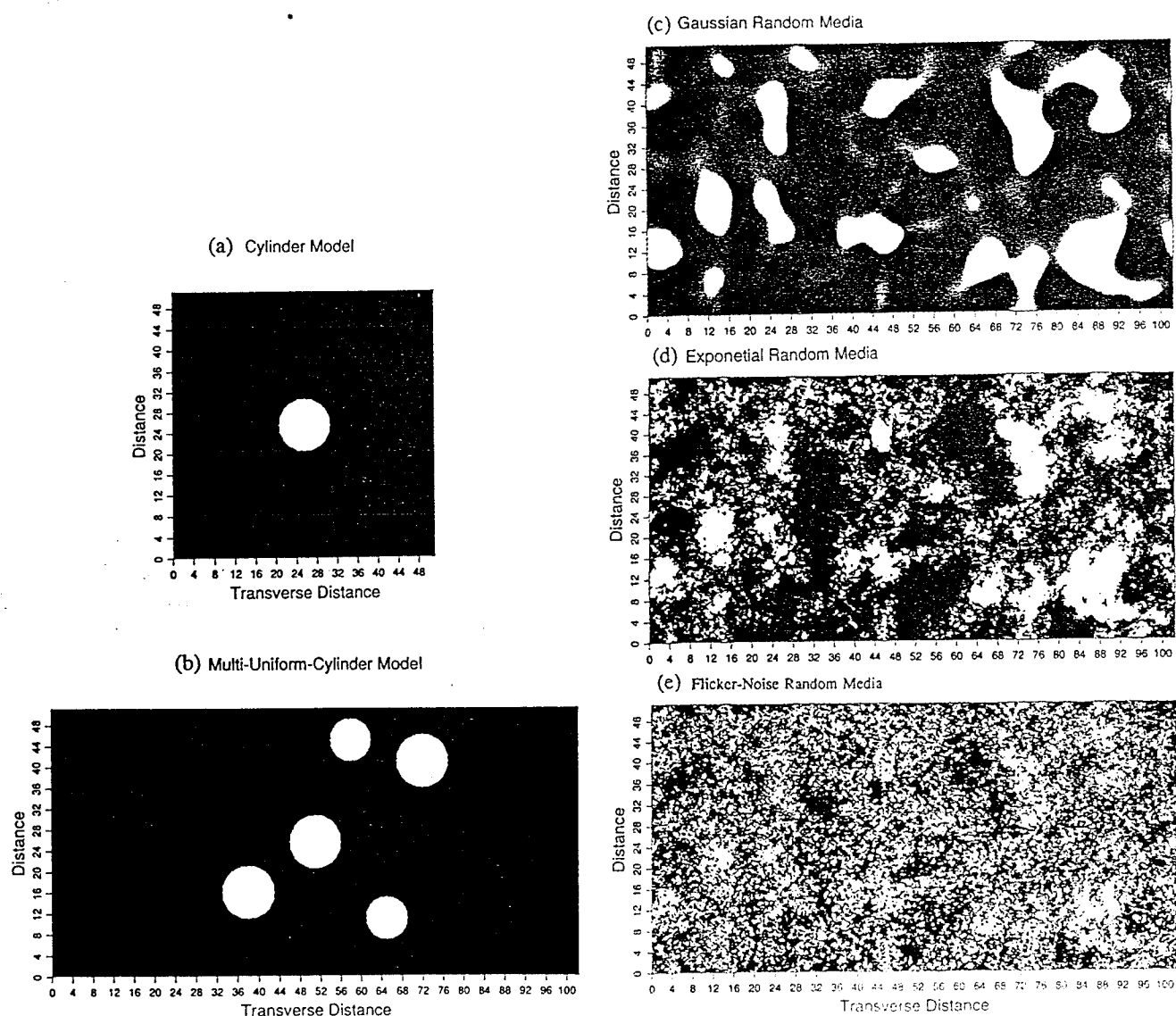


Figure 1. Velocity distributions of the five types of heterogeneities considered in this study. The size of the model space for the absorbing cylinder model is 51.2 by 51.2 km² and for the other four cases is 102.4 by 51.2 km². Models c, d, and e are constructed from the same random number seed. Areas with higher than average velocity are bright. (a) Absorbing cylinder model; (b) multi-uniform-cylinder model; (c) Gaussian random medium; (d) exponential random medium; (e) flicker-noise random medium.

Table 1
List of Models

Model	Medium	Correlation Function	2D Power Spectrum	$\epsilon = \left(\frac{\delta v}{v_0} \right)_{\text{rms}}$	Scale Length a (km)	$k_0 a$	Filter	Taper Length (Grid Points)
1a	absorbing cylinder	deterministic model		-0.2	5	10.5	Y	16
1b	cylinder models			-0.2	5	10.5	Y	16
1c				-0.3	5	10.5	Y	16
1d				+0.3	5	10.5	Y	16
1e				-0.5	5	10.5	Y	16
1f				+0.5	5	10.5	Y	16
2a	multi-uniform-cylinder	deterministic model		+0.3	4; 5	8.4; 10.5	Y	16
2b	cylinder models			-0.3	4; 5	8.4; 10.5	Y	16
2c				+0.5	4; 5	8.4; 10.5	Y	16
2d				-0.5	4; 5	8.4; 10.5	Y	16
3a	Gaussian	e^{-r^2/a^2}	$\frac{a^2}{2} e^{-k_r^2 a^2/4}$	+0.05	5	10.5	Y	16
3b	random media			+0.1	5	10.5	Y, N	16
3c				+0.15	5	10.5	Y	16
3d				+0.05	2	4.2	Y	16
4a	exponential	$e^{-r/a}$	$\frac{a^2}{(1 + k_r^2 a^2)^{3/2}}$	+0.05	5	10.5	Y	16
4b	random media			+0.1	5	10.5	Y	16
4c				+0.15	5	10.5	Y	16
4d				+0.05	2	4.2	Y	16
5a	flicker-noise			+0.05	5	10.5	Y	16
5b	random media	$K_0\left(\frac{r}{a}\right)$	$\frac{a^2}{1 + k_r^2 a^2}$	+0.1	5	10.5	Y, N	16
5c				+0.15	5	10.5	Y	16
5d				+0.05	2	4.2	Y	16

Note: $k_0 = 2\pi f_0/v_0$, where $v_0 = 6$ km/sec is the background velocity and $f_0 = 2$ Hz is the central frequency.

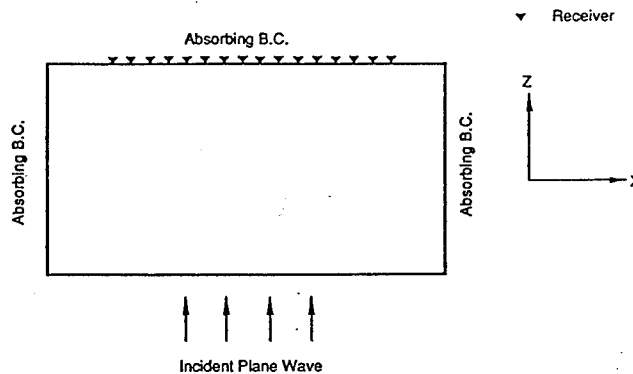


Figure 2. Schematic diagram of the 2D grid. Receivers are located at the grid points on the surface. The absorbing boundary condition is imposed to the four edges. Plane acoustic waves are incident upon the bottom of the grid and propagating toward the surface.

(Pao and Mow, 1973; Stanton, 1988). The exact solutions are known for the following cases: rigid, soft, fluid, and elastic cylinders. In this study we consider only the scattering of a plane acoustic wave by an absorbing fluid cylinder as a reference solution to compare with the phase screen method. The formulation in this article follows the approach of Stanton (1988).

General Solution of a Circular Cylinder. The pressure field p_i outside ($i = 1$) and inside ($i = 2$) the cylinder satisfy the wave equation

$$\nabla^2 p_i = \frac{1}{v_i^2} \frac{\partial^2 p_i}{\partial t^2}, \quad (4)$$

where v_i ($i = 1, 2$) are the complex compressional velocities outside and inside the cylinder, respectively. The boundary conditions require that pressure and the radial component of the particle displacement be continuous at the boundary of the cylinder,

$$p^{\text{inc}}(a) + p^{\text{scat}}(a) = p^{\text{int}}(a)$$

$$u_r^{\text{inc}}(a) + u_r^{\text{scat}}(a) = u_r^{\text{int}}(a), \quad (5)$$

where a is the radius of the cylinder, p^{inc} , p^{scat} , p^{int} , u_r^{inc} , u_r^{scat} , and u_r^{int} are the incident, scattered, and internal ($r < a$) pressures and radial components of the particle displacements, respectively. The pressure and the radial component of the particle displacement are related by

$$u_r = \frac{1}{\rho \omega^2} \frac{\partial p}{\partial r}. \quad (6)$$

Assume a normally incident plane acoustic wave with source spectrum $g(\omega)$ propagating along the z direction,

$$p^{\text{inc}} = \int_{-\infty}^{\infty} g(\omega) e^{i(k_1 z - \omega t)} d\omega. \quad (7)$$

The incident field can be expanded in terms of Bessel function

$$p^{\text{inc}} = \int_{-\infty}^{\infty} g(\omega) \sum_{m=0}^{\infty} \epsilon_m i^m \cos(m\theta) J_m(k_1 r) e^{-i\omega t} d\omega, \quad (8)$$

where ϵ_m is Neumann factor ($\epsilon_0 = 1$; $\epsilon_m = 2, m = 1, 2, \dots$), $k_1 = \omega/v_1$ is the wavenumber outside the cylinder, θ is the azimuthal angle in the plane perpendicular to the

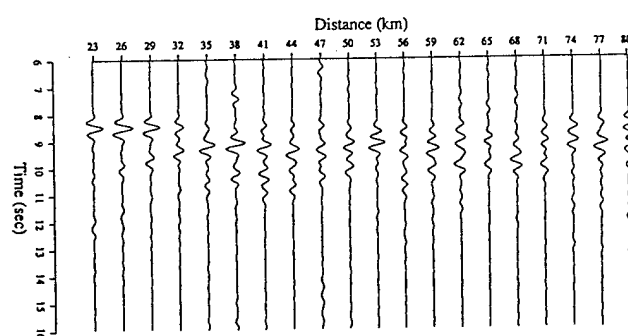
axis of the cylinder ($\theta = 0$ is the forward direction), ω is the angular frequency, $J_m(k_1 r)$ is the Bessel function of the first kind of order m . The general solution of the internal and scattered pressures are

$$p^{\text{int}} = \int_{-\infty}^{\infty} g(\omega) \sum_{m=0}^{\infty} A_m(k, \omega) \cos(m\theta) J_m(k_2 r) e^{-i\omega t} d\omega$$

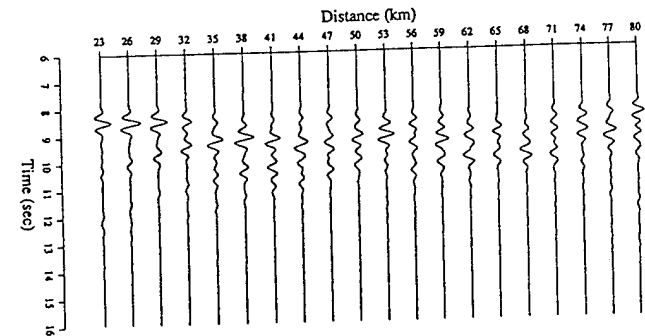
$$p^{\text{scat}} = \int_{-\infty}^{\infty} g(\omega) \sum_{m=0}^{\infty} B_m(k, \omega) \cos(m\theta) H_m^{(1)}(k_1 r) e^{-i\omega t} d\omega, \quad (9)$$

where $H_m^{(1)}(kr)$ is the first kind Hankel function, defined as $H_m^{(1)}(kr) = J_m(kr) + iN_m(kr)$, where $N_m(kr)$ is the Neumann function. The coefficients $A_m(k, \omega)$ and $B_m(k, \omega)$ are determined by boundary conditions.

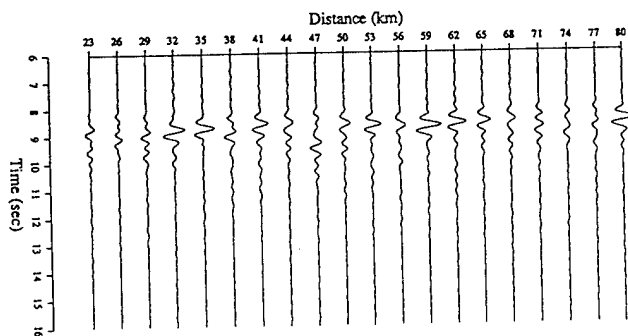
Substituting equations (8) and (9) into equation (6), we can derive the radial particle displacements,



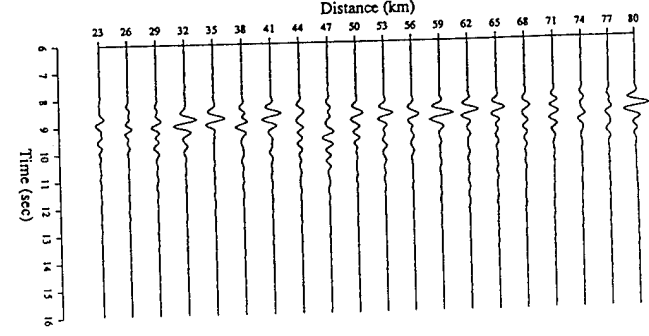
(a) Multi-Uniform-Cylinder Model ($\epsilon = -0.3$, $a = 5.0$ km)



(c) Multi-Uniform-Cylinder Model ($\epsilon = -0.3$, $\Delta z = 4, 16$)



(b) Flicker-Noise Random Media ($\epsilon = 0.1$, $a = 5.0$ km)

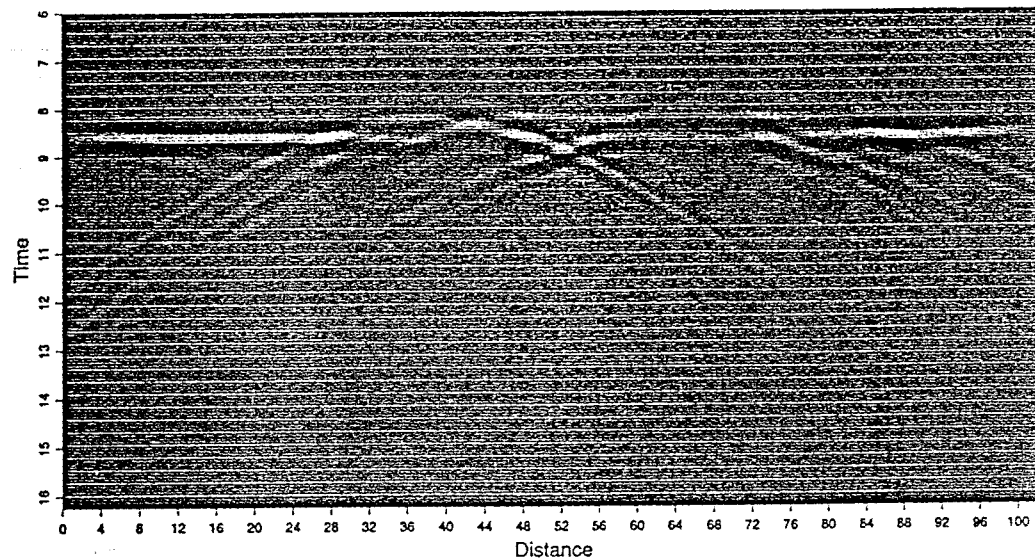


(d) Flicker-Noise Random Media ($\epsilon = 0.1$, $a = 5.0$ km, $\Delta z = 4, 16$)

Figure 3. Synthetic phase screen seismograms without wavenumber filter: (a) for model 2b and (b) for model 5b. Synthetic phase screen seismograms with wavenumber filter for different screen intervals: (c) for model 2b and (d) for model 5b.

$$\begin{aligned}
 u_r^{\text{inc}} &= \int_{-\infty}^{\infty} g(\omega) \frac{1}{\rho_1 \omega^2} \sum_{m=0}^{\infty} \epsilon_m i^m \cos(m\theta) J'_m(k_1 r) e^{-i\omega t} d\omega & u_r^{\text{scat}} &= \int_{-\infty}^{\infty} g(\omega) \frac{1}{\rho_1 \omega^2} \sum_{m=0}^{\infty} B_m(k, \omega) \\
 u_r^{\text{int}} &= \int_{-\infty}^{\infty} g(\omega) \frac{1}{\rho_2 \omega^2} \sum_{m=0}^{\infty} A_m(k, \omega) \cos(m\theta) J'_m(k_2 r) e^{-i\omega t} d\omega & \cdot \cos(m\theta) H_m^{(1)\prime}(k_1 r) e^{-i\omega t} d\omega,
 \end{aligned} \tag{10}$$

(a) Multi-Cylinder Model (FD)



(b) Multi-Cylinder Model (Phase Screen)

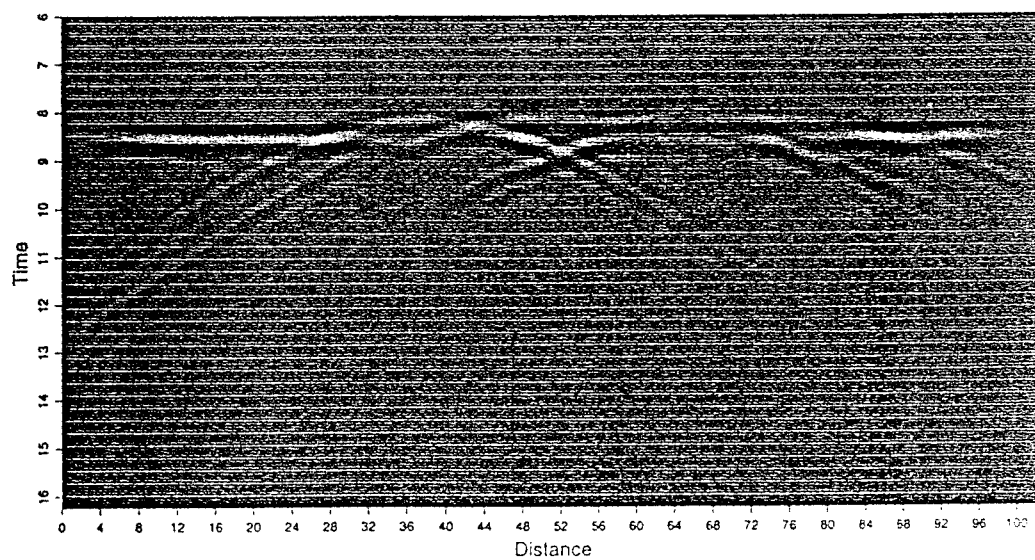


Figure 4. Comparison of gray-scale graphics of seismograms from finite difference (FD) and phase screen calculations: (a) and (b) are for model 2a (multi-cylinder model); (c) and (d) are for model 5b (flicker-noise random medium).

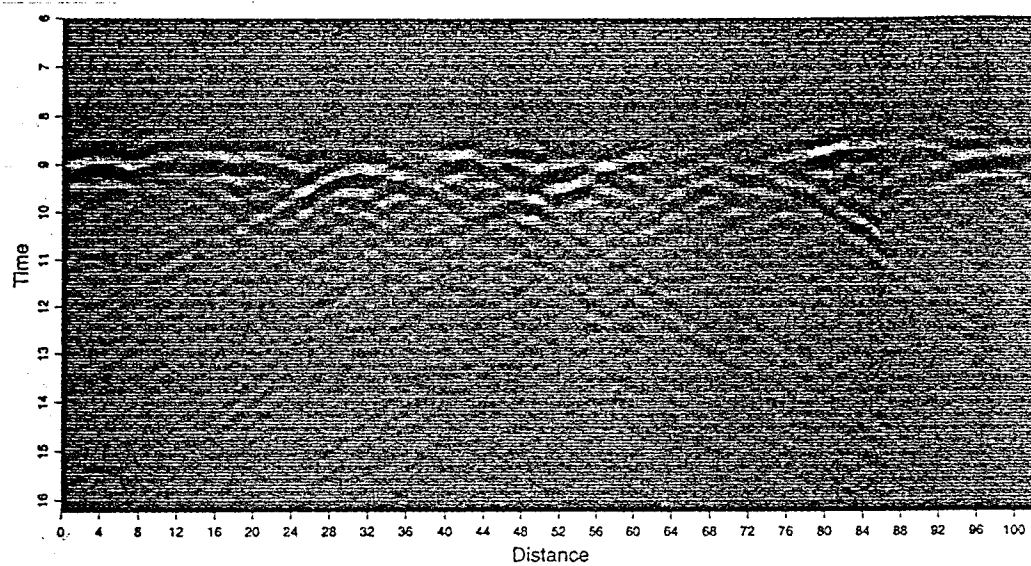
where ρ_i is the density outside ($i = 1$) and inside ($i = 2$) the cylinder and the prime on each J and H represents the derivative with respect to argument r .

Substituting equations (8), (9), and (10) into equation (5), we can solve the coefficients $A_m(k, \omega)$ of the internal field and $B_m(k, \omega)$ of the scattered field

$$A_m(k, \omega) = \frac{2g\epsilon_m i^{m+1}}{\pi a \Delta_m}$$

$$B_m(k, \omega) = \frac{\epsilon_m i^m \Delta_m}{\Delta_m}, \quad (11)$$

(c) Flicker-Noise Random Media (FD)



(d) Flicker-Noise Random Media (Phase Screen)

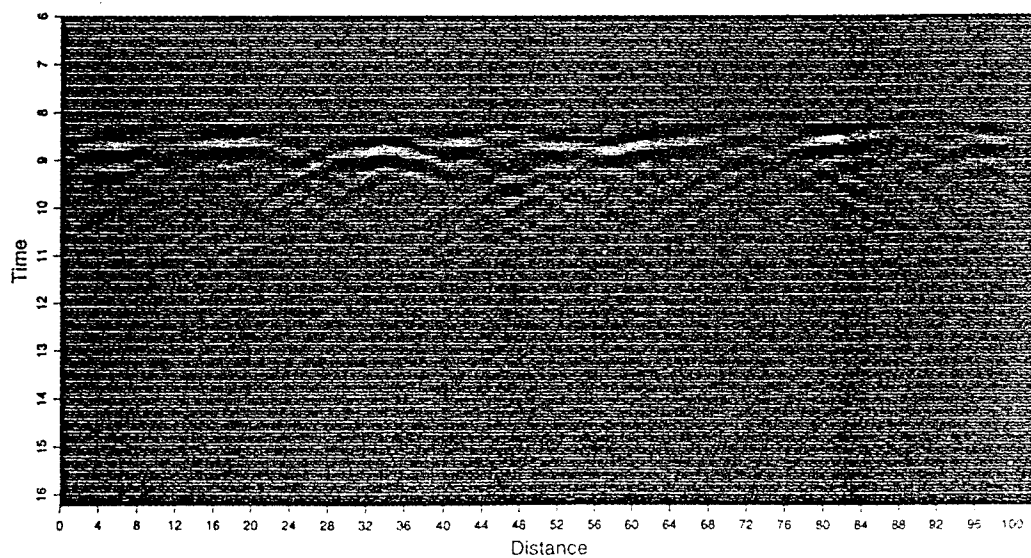


Figure 4.—Continued

where

$$\begin{aligned}\Delta_{m1} &= g k_1 J_m(k_2 a) J_{m+1}(k_1 a) - k_2 J_m(k_1 a) J_{m+1}(k_2 a) \\ &\quad - \frac{m}{a} (g - 1) J_m(k_1 a) J_m(k_2 a) \\ \Delta_m &= k_2 J_{m+1}(k_2 a) H_m^{(1)}(k_1 a) - g k_1 J_m(k_2 a) H_{m+1}^{(1)}(k_1 a) \\ &\quad + \frac{m}{a} (g - 1) J_m(k_2 a) H_m^{(1)}(k_1 a) \\ g &= \frac{\rho_2 v_2}{\rho_1 v_1}.\end{aligned}\quad (12)$$

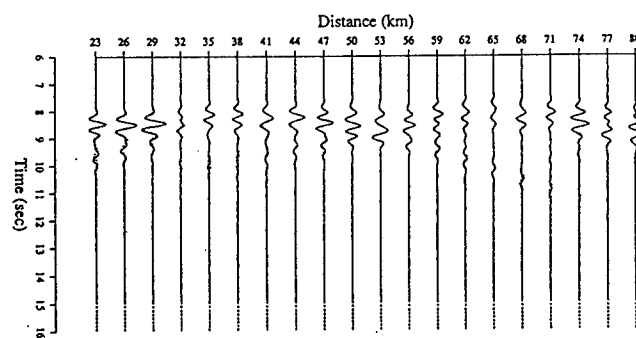
The total pressure p^{total} outside the cylinder can be written as

$$p^{\text{total}} = \int_{-\infty}^{\infty} g(\omega) \left[e^{ik_1 z} + \sum_{m=0}^{\infty} B_m(k, \omega) \cos(m\theta) H_m^{(1)}(k_1 r) \right] \cdot e^{-i\omega t} d\omega. \quad (13)$$

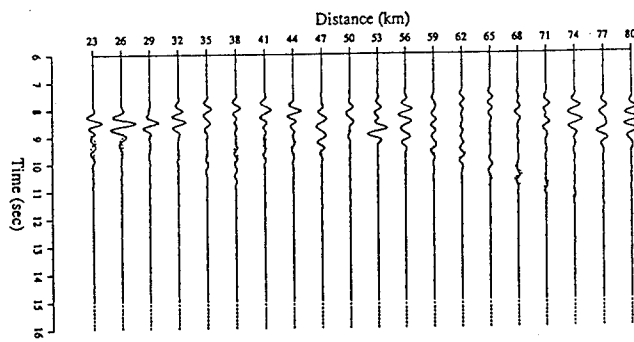
Equation (13) is the analytic solution of the acoustic wave scattering by a circular cylinder. For an absorbing circular cylinder the corresponding velocity and wavenumber become complex. The incident field can be calculated by equation (7). The rate of convergences of the series in equation (13) depends on the difference between the inner and outer refraction indexes, but is much more sensitive to the value of $k_1 a$. The higher the values of $k_1 a$ is, the slower the convergence. In this article, the number of terms retained in the series is 60. This number is more than adequate to render the truncation errors negligible in all the cases treated in the article. For each frequency loop, we stop the series summation when the relative difference between successive terms is less than 10^{-5} . We can also calculate the internal pressure p^{int} by equation (9).

Generation of Inhomogeneous Media with Absorption

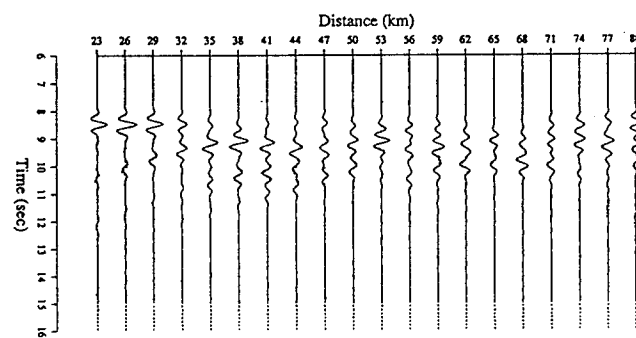
A number of inhomogeneous media were used to compare the phase screen and finite difference methods. We chose five kinds of models: (1) absorbing cylinder model, (2) multi-uniform-cylinder model, (3) Gaussian



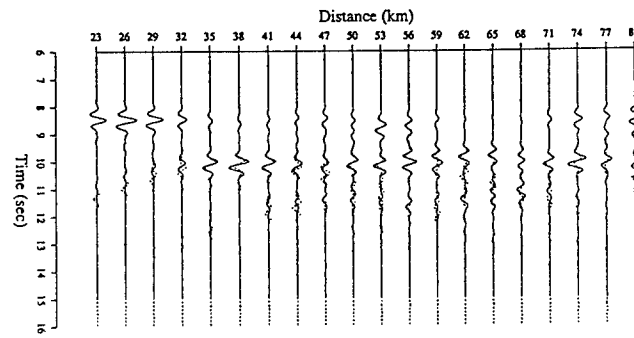
(a) Multi-Uniform-Cylinder Model ($\epsilon = 0.3$, $a = 4.0, 5.0$ km)



(c) Multi-Uniform-Cylinder Model ($\epsilon = 0.5$, $a = 4.0, 5.0$ km)



(b) Multi-Uniform-Cylinder Model ($\epsilon = -0.3$, $a = 4.0, 5.0$ km)



(d) Multi-Uniform-Cylinder Model ($\epsilon = -0.5$, $a = 4.0, 5.0$ km)

Figure 5. Comparison of synthetic seismograms for (a) model 2a, (b) model 2b, (c) model 2c, and (d) model 2d (see Table 1). Solid and dotted curves stand for the phase screen and finite difference solutions, respectively.

random media, (4) exponential random media, and (5) flicker-noise random media, which were called "self-similar random media" by Frankel and Clayton (1986). Figure 1 shows typical realizations of the velocity structure of the five kinds of models. There are considerably more small-scale structures in flicker-noise media than in exponential and Gaussian media. For the definition and generation of those three kinds of random media in the 2D case, see Frankel and Clayton (1986).

For absorbing media, we assume Azimi's attenuation law (Azimi *et al.*, 1968; Aki and Richards, 1980) is satisfied to keep the propagation causal. The corresponding complex wavenumber and complex velocity have the following dispersion relation:

$$k = \frac{\omega}{v(\omega)} + i\alpha(\omega)$$

$$\frac{1}{v(\omega)} = \frac{1}{v(\infty)} + \frac{2\alpha_0}{\pi(1 - \alpha_1^2\omega^2)} \ln\left(\frac{1}{\alpha_1\omega}\right)$$

$$\alpha(\omega) = \frac{\alpha_0\omega}{1 + \alpha_1\omega}, \quad (14)$$

where α_0 and α_1 are constants determining the absorbing properties of the media, and $v(\infty)$ is the limit of $v(\omega)$ as $\omega \rightarrow \infty$, Q has an approximate value $[2v(\infty)\alpha_0]^{-1}$.

In order to reduce the boundary effects, we choose the model space long enough in the horizontal direction and make observations only in the middle section. The model sizes are 51.2 by 51.2 km² for the absorbing cylinder model and 102.4 by 51.2 km² for the other four models. Arrays of receivers were located in the middle of the surface along the x direction. A schematic diagram of the model space is shown in Figure 2. The spacing of the grid points is $dx = dz = 0.2$ km.

Table 1 lists the parameters of the models in this study. These models are chosen to expose how the accuracy depends on the correlation function (or power spectrum), magnitude of the velocity perturbation, and the ratio of wavelength to correlation length (or scale length). The background velocity used throughout this study is $v_0 = 6.0$ km/sec. Correlation lengths of 5 km and 2 km are used. The values k_0a are given in Table 1, where k_0 denotes the wavenumber of dominant frequency (2 Hz).

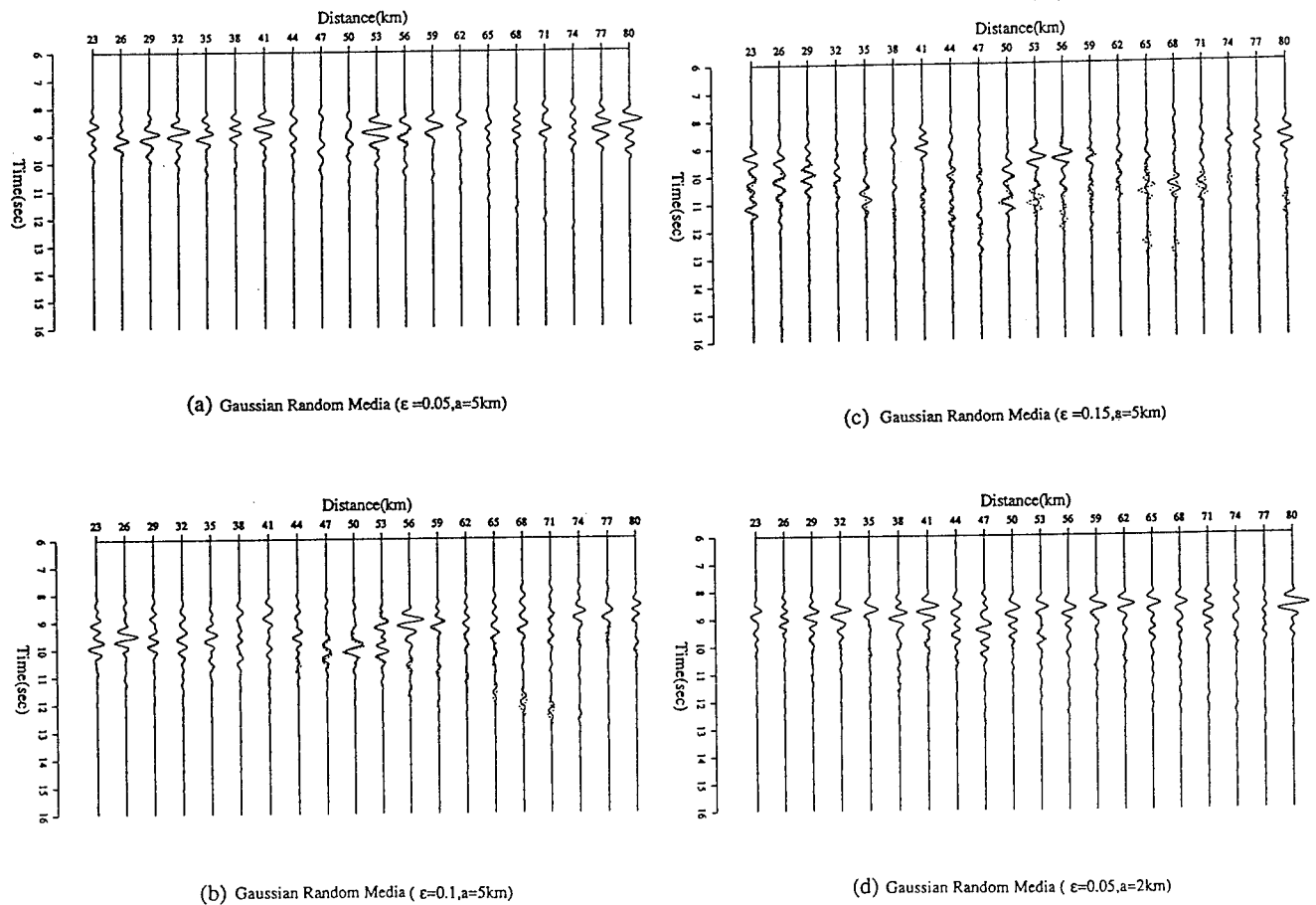


Figure 6. Comparison of synthetic seismograms for (a) model 3a, (b) model 3b, (c) model 3c, and (d) model 3d (see Table 1). Solid and dotted curves stand for the phase screen and finite difference solutions, respectively.

Source Time Function and Wavenumber Filtering

The source time function in our study is a Ricker wavelet defined by

$$g(t) = e^{-1/2f_{max}^2(t-t_0)^2} \cos [\pi f_{max}(t - t_0)], \quad (15)$$

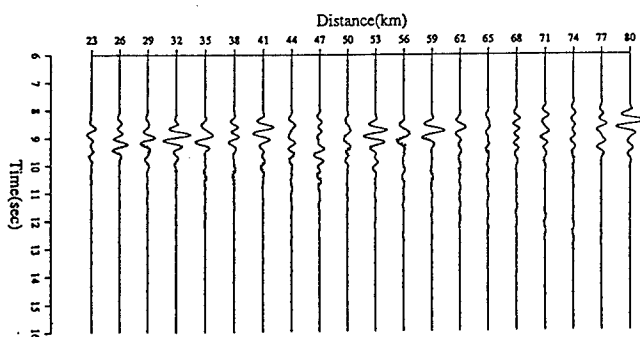
where f_{max} is the maximum frequency and t_0 defines the origin of time. The value $f_{max} = 4$ Hz was used for all simulations, corresponding to a central frequency of $f_0 = 2$ Hz. The wave is incident from the bottom of the model. The same time step $\Delta t = 0.02$ was used for the phase screen, finite difference, and eigenfunction expansion methods.

The phase screens for all of the models are uniformly spaced every 16 grid points ($\Delta z = 3.2$ km) in the z direction. This spacing is used in order to satisfy the geometrical optics condition within screen interval. Comparison between phase screen seismograms with different screen intervals has been done and showed that there was no noticeable difference between seismograms of up to 16 grid point screen intervals (see Figs. 3c and 3d). In order to reduce the artifacts due to the aliasing

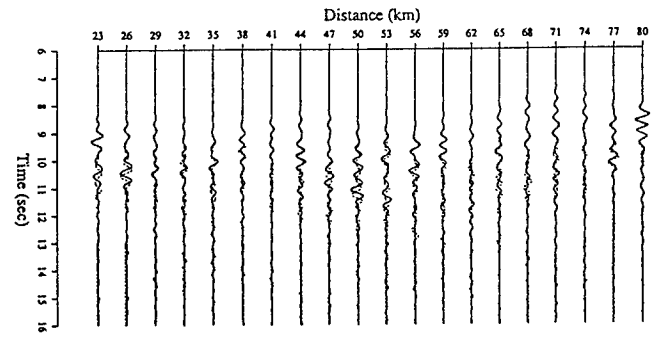
effect at very high wavenumbers, a wavenumber filter is applied to the wave field in wavenumber domain at each step (Nautiyal, 1988; Wu and Huang, 1992). Figures 3a and 3b show the synthetic seismograms without wavenumber filters for the multi-uniform-cylinder model and the flicker-noise random medium, respectively. In the figures, the wiggles before the first arrivals and in the later coda are the aliasing artifacts. After applying the wavenumber filtering, the artifacts are effectively removed (Figs. 3c and 3d). Space-domain cosine tapers are also applied to the wave field in space domain near the two side walls to reduce the side-wall boundary effect.

Comparison

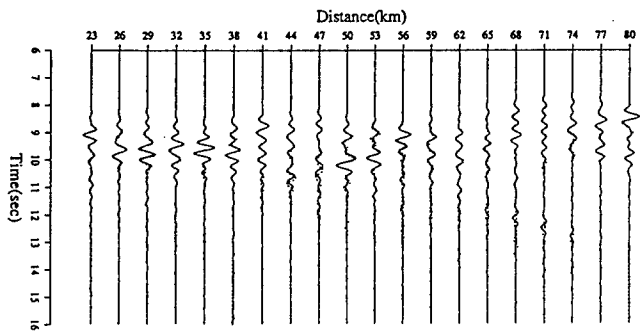
Since the finite difference and eigenfunction expansion results were used as the references in this comparison, it is important to assess the accuracy of those methods. The eigenfunction expansion is an analytic solution and can give exact results as long as enough terms are taken. To test the degree to which FD converges to the



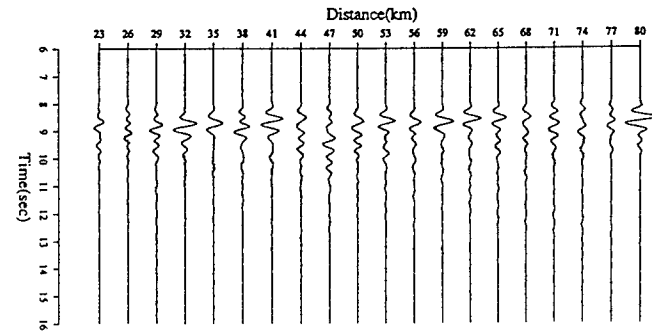
(a) Exponential Random Media ($\epsilon = 0.05, a = 5$ km)



(c) Exponential Random Media ($\epsilon = 0.15, a = 5$ km)



(b) Exponential Random Media ($\epsilon = 0.1, a = 5$ km)



(d) Exponential Random Media ($\epsilon = 0.05, a = 2$ km)

Figure 7. Comparison of synthetic seismograms for (a) model 4a, (b) model 4b, (c) model 4c, and (d) model 4d (see Table 1). Solid and dotted curves stand for the phase screen and finite difference solutions, respectively.

exact solution, we doubled the number of grid points for one of the models used in the FD calculations and found that the differences in the solutions were negligible.

Comparison of Phase Screen with Finite Difference for Multi-Cylinder Models

Figure 4 gives the gray scale graphics of synthetic seismic sections from finite difference simulation and the phase screen method for a multi-uniform-cylinder model (Figs. 4a and 4b) and for flicker-noise random media (Figs. 4c and 4d), respectively. We see that for large-scale heterogeneities, such as those in the multi-cylinder model, the agreement between phase screen and FD is excellent, because forward scattering is dominant in this case. On the other hand, the agreement deteriorates for the case of the flicker-noise medium, especially for later arrivals, since the flicker-noise medium is rich in small-scale heterogeneities that cause strong large-angle scattering. It can be also seen that because of the treatment at the boundaries (tapering, absorbing boundary condition), the amplitude of the field is distorted near the boundaries. Therefore, in the following we will only

compare the synthetic seismograms away from the vertical boundaries; i.e., in the regions of 12 to 40 km for the absorbing cylinder model and 23 to 80 km for the other four models. In this way we can also avoid the wrap-around effects due to the equivalent periodic boundary condition of the phase screen method and the boundary reflections of the FD method due to the imperfect absorbing boundary conditions.

Figure 5 shows synthetic seismograms of high- and low-velocity multi-uniform-cylinder models calculated by phase screen and finite difference for receivers located in the middle of the section. Solid and dotted curves stand for the phase screen and finite difference solutions, respectively. It can be seen that for velocity perturbations with $\epsilon = +30\%$ (Fig. 5a), $\epsilon = -30\%$ (Fig. 5b), $\epsilon = +50\%$ (Fig. 5c), and $\epsilon = -50\%$ (Fig. 5d), the phase screen results are in excellent agreement with the finite difference solutions, demonstrating that the phase screen method can give good results for strong discrete scatterers. However, as can be noticed from Fig. 5d, the strong later arrivals for the case of low-velocity cylinders have large errors compared with the FD solution.

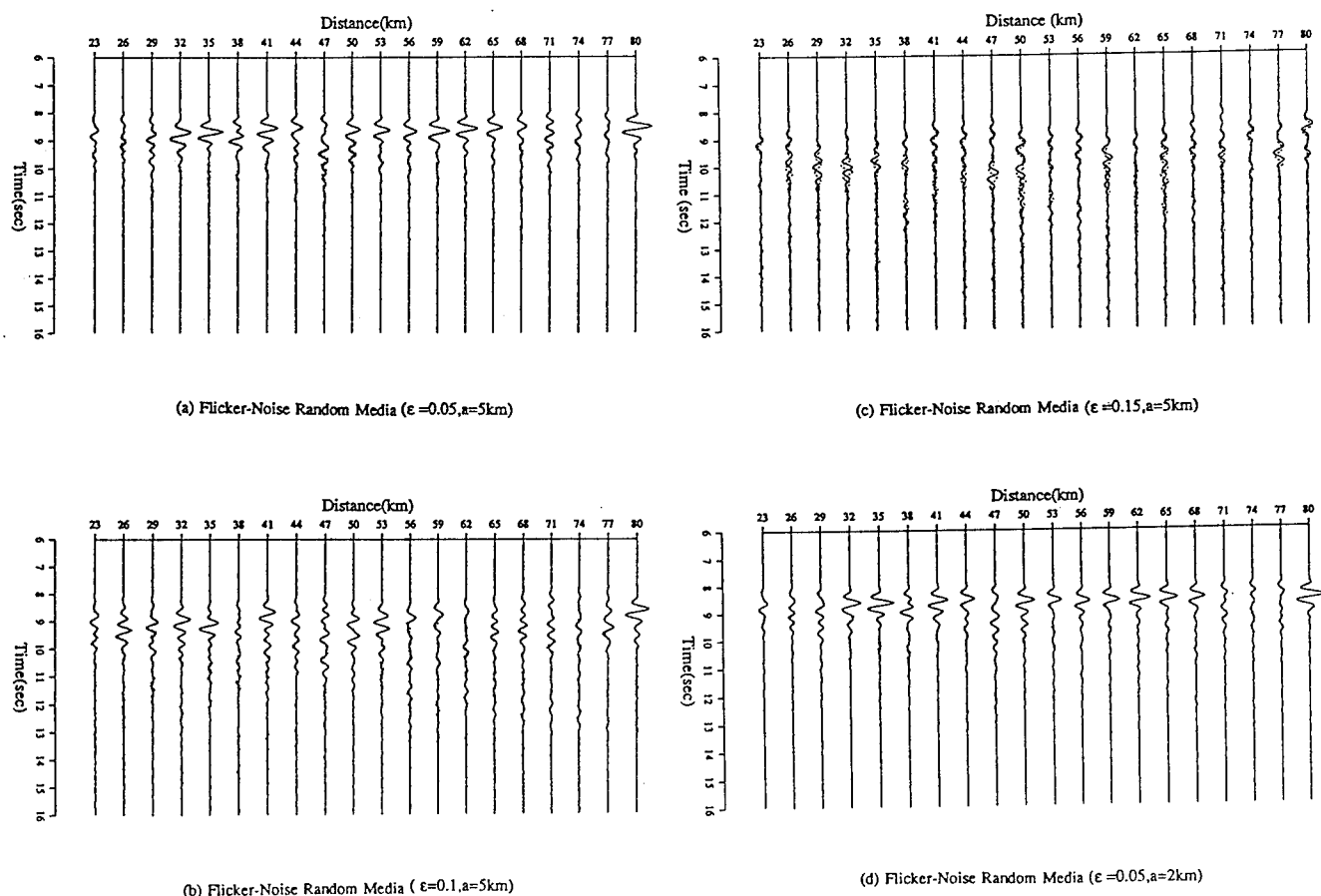


Figure 8. Comparison of synthetic seismograms for (a) model 5a, (b) model 5b, (c) model 5c, and (d) model 5d (see Table 1). Solid and dotted curves stand for the phase screen and finite difference solutions, respectively.

Comparison of Phase Screen with Finite Difference for Random Medium Models

Synthetic seismograms from phase screen and finite difference methods for Gaussian random media, exponential random media, and flicker-noise random media are shown in Figures 6 through 8. Solid and dotted curves stand for the phase screen and finite difference results, respectively. Figures 6a, 6d, 7a, 7d, 8a, and 8d are the seismograms of the three kinds of random media with velocity perturbations of $\epsilon = 5\%$ and scale lengths $a = 5$ and 2 km, respectively. The comparison shows excellent agreement in the case of weak random media ($\epsilon \leq 5\%$).

Figures 6b, 7b, and 8b are the seismograms of the three kinds of random media with velocity perturbation

$\epsilon = 10\%$, respectively. It is obvious that the agreement between the waveforms at early times is very good, but it degrades at later times. It is apparent that the coda at later times for these models come from large-angle multiple scattering.

Figures 6c, 7c, and 8c are the seismograms of the three kinds of random media with velocity perturbation $\epsilon = 15\%$, respectively. The agreement between phase screen and finite difference solutions degenerates more than that in Figures 6b, 7b, and 8b. The coda of the phase screen calculations is noticeably less than that of the finite difference results. Clearly, large-angle scattering and backscattering play significant roles in producing the larger amplitude of codas in the FD results.

To quantify the comparison between the phase screen and finite difference results. The rms differences between the phase screen and finite difference seismograms were calculated. Figures 9a ($\epsilon = 0.05$, $a = 5$ km), 9b ($\epsilon = 0.10$, $a = 5$ km), and 9c ($\epsilon = 0.15$, $a = 5$ km) show the relative rms differences of seismograms as functions of time for nine models. The rms averages are taken over the 282 receivers and normalized by the maximum amplitude of the seismograms at the correspond-

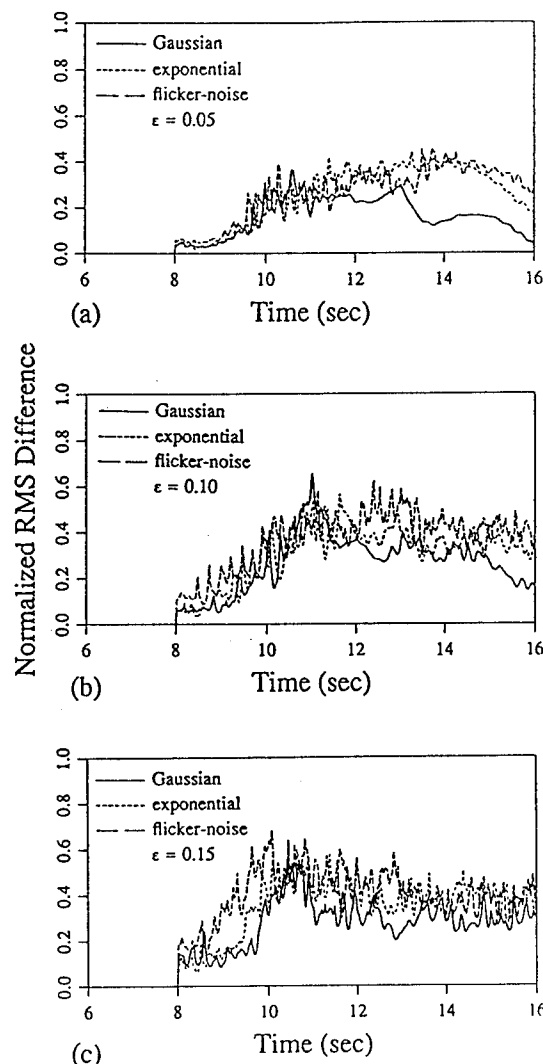
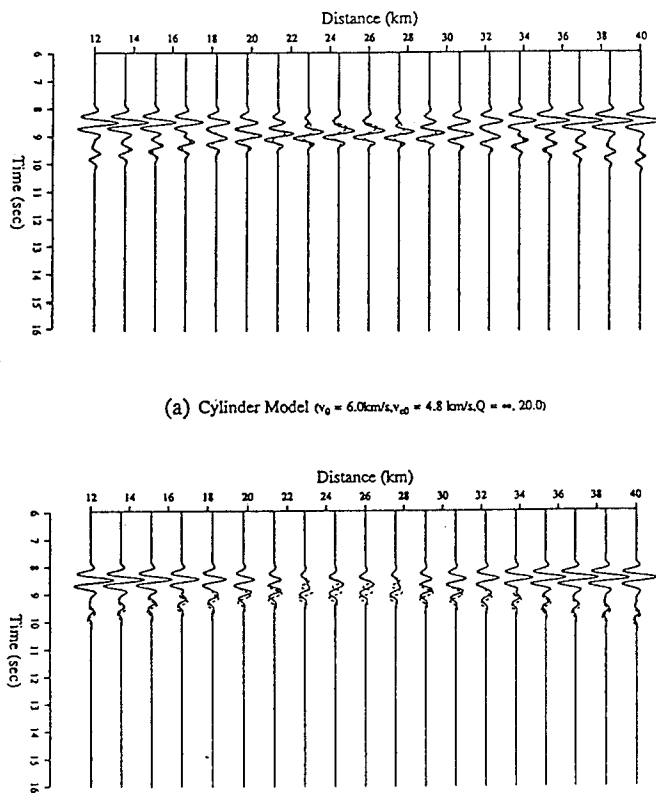


Figure 9. Root mean square differences of the phase screen and finite difference seismograms for the nine models. The rms differences are normalized by the maximum amplitude at the corresponding time for each curve.



(b) Absorbing Cylinder ($v_0 = 6.0 \text{ km/s}$, $v_{r0} = 4.8 \text{ km/s}$, $a_0 = 5.2 \times 10^{-3}$, $a_1 = 8.0 \times 10^{-4}$, $Q = 20.0$)

Figure 10. Comparison of synthetic seismograms for (a) model 1a with (dotted) and without (solid) intrinsic attenuation, (b) model 1b with (dotted) and without (solid) velocity dispersion.

ing time. It is apparent that weak random media ($\epsilon \leq 10\%$) are treated more accurately by the phase screen method than for the strong random media ($\epsilon = 15\%$), and the seismograms for earlier arrivals (from 8 to 10 sec) compare with the FD solutions more favorably for Gaussian and exponential than for flicker-noise random media. Large-angle scattering and backscattering are more significant in the latter cases.

Computation Speed

For the numerical examples calculated in this article, the grid size is 512 by 256. In a SUN IV station the CPU time for the 2D FD is 7108 sec, while for the phase screen method with screen interval of 16 grid points, the CPU time is 478 sec, about 15 times faster than the FD algorithm. We have run several examples of 1024 by 512 grid size in a SUN SPARC II station. The CPU times for FD and phase screen (with screen interval of 32 points) are 20,917 sec and 367 sec, respectively. The time sav-

ings is about 57 times. For large 3D problems, the saving in CPU time and computer storage is expected to be much greater.

Comparison of Phase Screen with Exact Solutions for an Absorbing Cylinder

Figure 10a shows the synthetic seismograms from the exact solution for a single cylinder model with and without intrinsic attenuation. Solid and dotted curves stand for the nonabsorbing and absorbing cylinder scatterers, respectively. Due to the absorption effect, the amplitudes from the absorbing cylinder are less than those from the nonabsorbing cylinder.

In order to have a causal attenuation signal, a small amount of dispersion is introduced according to the *Kramers-Krönig* relation (Aki and Richards, 1980). Figure 10b shows the synthetic seismograms from exact solution for the absorbing cylinder model with and without phase velocity dispersion. Solid and dotted curves stand

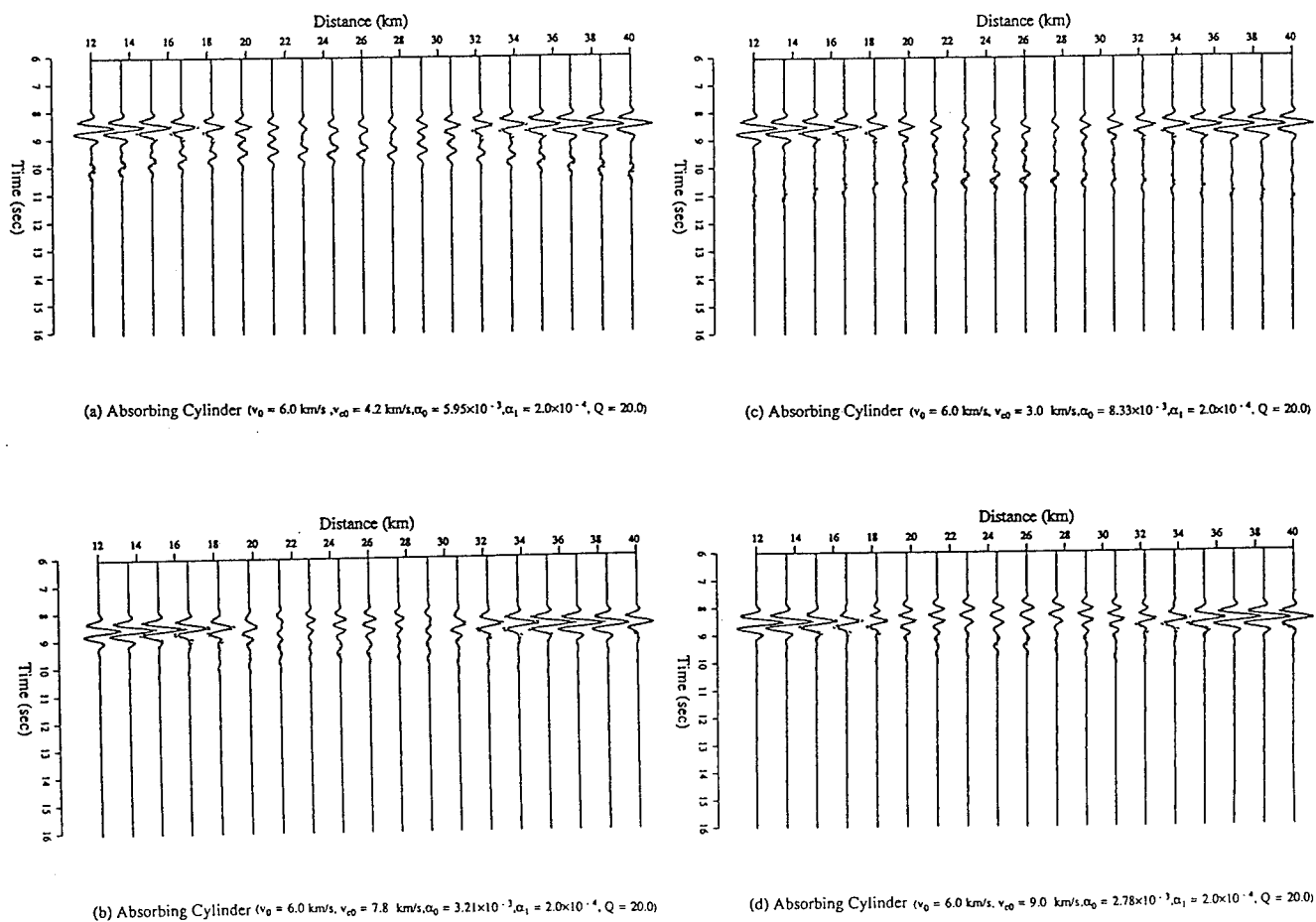


Figure 11. Comparison of PHS (phase screen) and eigenfunction expansion results for (a) model 1c with $\alpha_0 = 5.95 \times 10^{-3}$ and $\alpha_1 = 2.0 \times 10^{-4}$; (b) model 1d with $\alpha_0 = 3.21 \times 10^{-3}$ and $\alpha_1 = 2.0 \times 10^{-4}$; (c) model 1e with $\alpha_0 = 8.33 \times 10^{-3}$ and $\alpha_1 = 2.0 \times 10^{-4}$; and (d) model 1f with $\alpha_0 = 2.78 \times 10^{-3}$ and $\alpha_1 = 2.0 \times 10^{-4}$. Solid and dotted curves stand for the phase screen and exact solutions, respectively.

for the nondispersive and dispersive cylinders, respectively. It can be seen that some waveform change occurs due to the dispersion effect.

Figures 11a and 11b show the seismograms from the absorbing cylinders (with causal dispersion, $Q = 20.0$, $\rho_1 = \rho_2$) with velocity perturbations of $\epsilon = -30\%$ ($\alpha_0 = 5.95 \times 10^{-3}$, $\alpha_1 = 2.0 \times 10^{-4}$) and $+30\%$ ($\alpha_0 = 3.2 \times 10^{-3}$, $\alpha_1 = 2.0 \times 10^{-4}$), respectively. Solid and dotted curves stand for the phase screen and exact solutions, respectively. The phase screen results are in good agreement with the exact solutions.

Figures 11c and 11d show the seismograms from the absorbing cylinders (with causal dispersion, $Q = 20.0$, $\rho_1 = \rho_2$) with velocity perturbations $\epsilon = -50\%$ ($\alpha_0 = 8.33 \times 10^{-3}$, $\alpha_1 = 2.0 \times 10^{-4}$) and $+50\%$ ($\alpha_0 = 2.78 \times 10^{-3}$, $\alpha_1 = 2.0 \times 10^{-4}$). Solid and dotted curves stand for the phase screen and exact solutions, respectively. The agreement between the phase screen and exact solutions is better for the high-velocity cylinder than for the low-velocity cylinder.

Conclusions

From the comparison of the phase screen method with the exact solution for a cylinder and the FD solutions for various heterogeneous media we can draw the following conclusions. The phase screen solution can give good results for strong discrete heterogeneous media with and without intrinsic attenuation if the size of the scatterers are large compared with the wavelength. For continuous random media, the comparison of synthetic seismograms by phase screen and finite difference methods was made for three kinds of models: (1) Gaussian random media, (2) exponential random media, and (3) flicker-noise random media. Results show good agreement for weak random media (velocity perturbations $\leq 10\%$), similar to the results obtained by Fisk *et al.* (1992). The phase screen method is most accurate for the early part of the seismograms, where the arrivals have undergone only small-angle scattering. At later times, especially for the case of strong scattering, backscattering becomes more important and the phase screen method becomes less accurate compared with the finite difference method because of the neglect of backscattered waves in the phase screen formulation. Therefore, wherever the backscattered waves are insignificant or can be separated from the major wave groups of interest, the phase screen method can be used to generate synthetic seismograms with much faster computation speed than FD calculations. The other advantage of the phase screen method is the capability of modeling arbitrarily absorbing inhomogeneous media.

Acknowledgments

This work was supported by NSF Grant Number EAR-9205830 and the Airforce Office of Scientific Research Contract Number F49620-

92-J-0461 of the United States, and the Natural Sciences Foundation of China. The support from the W. M. Keck Foundation is also appreciated. We are grateful to Dr. T. Lay for his suggestions and discussions and to Dr. X. B. Xie for his help in the FD calculations. This is Contribution Number 222 from the Institute of Tectonics, University of California.

References

Aki, K. and P. G. Richards (1980). *Quantitative Seismology: Theory and Methods*, Vol. 1, W. H. Freeman, San Francisco.

Alford, R. M., K. R. Kelly, and D. M. Boore (1974). Accuracy of finite-difference modeling of the acoustic wave equation, *Geophysics*, **39**, 834–841.

Azimi, Sh. A., V. V. Kalinin, and B. L. Pivovarov (1968). Impulse and transient characteristic of media with linear and quadratic absorption laws, *Phys. Solid Earth* **2**, 88–93.

Bramley, E. N. (1977). The accuracy of computing ionospheric radio-wave scintillation by the thin-phase screen approximation, *J. Atmos. Terr. Phys.* **39**, 367–373.

Buckley, R. (1975). Diffraction by a random phase-changing screen: a numerical experiment, *J. Atmos. Terr. Phys.* **37**, 1431–1446.

Chernov, L. A. (1960). *Wave Propagation in a Random Medium*, McGraw-Hill, New York.

Clayton, R. and B. Engquist (1977). Absorbing boundary conditions for acoustic and elastic wave equations, *Bull. Seism. Soc. Am.* **67**, 1529–1540.

Feit, M. D. and J. A. Fleck, Jr. (1978). Light propagation in graded-index optical fibers, *Appl. Opt.* **17**, 3990–3998.

Fisk, M. D. and D. G. McCarter (1991). The phase screen method for vector elastic waves, *J. Geophys. Res.* **96**, 5985–6010.

Fisk, M. D., E. E. Charrette, and D. G. McCarter (1992). A comparison of phase screen and finite difference calculations for elastic waves in random media, *J. Geophys. Res.* **97**, 12409–12423.

Fisk, M. D. and D. G. McCarter (1993). Fluctuation analysis of elastic waves in random media via phase screen simulations, *J. Geophys. Res.* **98**, 685–697.

Flatté, S. M., R. Dashen, W. H. Munk, K. M. Watson, and F. Zarchariasen (1979). *Sound Transmission Through A Fluctuating Ocean*, Cambridge University Press, New York.

Frankel, A. and R. W. Clayton (1986). Finite difference simulations of seismic scattering: implications for the propagation of short-period seismic waves in the crust and models of crustal heterogeneity, *J. Geophys. Res.* **91**, 6465–6489.

Ishimaru, A. (1978). *Wave Propagation and Scattering in Random Media*, Vols. 1 and 2, Academic Press, New York.

Knepp, D. L. (1983). Multiple phase screen calculation of the temporal behavior of stochastic waves, *Proc. IEEE* **71**, 722–737.

Malischewsky, P. (1987). *Surface Wave and Discontinuities*, Elsevier, New York.

Martin, J. M. and S. M. Flatté (1988). Intensity images and statistics from numerical simulation of wave propagation in 3-D random media, *Appl. Opt.* **27**, 2111–2125.

Mercier, R. P. (1962). Diffraction by a screen causing large random phase fluctuations, *Proc. Cambridge Philos. Soc.* **58**, 382–400.

Nautiyal, A. (1988). Antialiasing methods for two-dimensional spatial wavelets in seismic modeling, *Geophysics* **53**, 1202–1206.

Pao, Y. H. and C. C. Mow (1973). *Diffraction of Elastic Waves and Dynamics Stress Concentrations*, Crane and Russak, New York.

Ratcliffe, J. A. (1956). Some aspects of diffraction theory and their application to the ionosphere, *Rep. Prog. Phys.* **19**, 190–263.

Stanton, T. K. (1988). Sound scattering by cylinder of finite length I fluid cylinder, *J. Acoust. Soc. Am.* **83**, 55–63.

Stoffa, P. L., J. T. Fokkema, R. M. D. Freire, and W. P. Kessinger (1990). Split-step Fourier migration, *Geophysics* **55**, 410–421.

Tatarskii, V. I. (1961). *Wave Propagation in a Turbulent Medium*, McGraw-Hill, New York.

Thomson, D. J. (1990). Wide-angle parabolic equation solutions to two range-dependent bench-mark problems, *J. Acoust. Soc. Am.* **87**, 1514-1520.

Thomson, D. J. and N. R. Chapman (1983). A wide-angle split-step algorithm for the parabolic equation, *J. Acoust. Soc. Am.* **74**, 1848-1854.

Wu, R. S. (1988). Seismic wave scattering, in *Encyclopedia of Geophysics*, D. E. James (Editor), Van Nostrand Reinhold, New York, 1166-1187.

Wu, R. S. (1994). Wide-angle elastic one-way propagation in heterogeneous media and an elastic wave complex-screen method, *J. Geophys. Res.* **99**, 751-766.

Wu, R. S. and K. Aki (1985). Elastic wave scattering by a random medium and the small scale inhomogeneities in the lithosphere, *J. Geophys. Res.* **90**, 10261-10237.

Wu, R. S. and K. Aki (1988, 1989, 1990). *Scattering and Attenuation of Seismic Waves*, Vols. 1, 2, and 3, Birkhauser Verlag, Boston.

Wu, R. S. and L. J. Huang (1992). Scattered field calculation in heterogeneous media using phase-screen propagator, in *62nd Annual Meeting of SEG* (extended abstract), SEG, Tulsa, 1289-1292.

University of California
Santa Cruz, California 95064

Manuscript received 13 September 1993.

Effects of Crustal Structure under the Barents and Kara Seas on Short-Period Regional Wave Propagation for Novaya Zemlya Explosions: Empirical Relations

by Tianrun Zhang and Thorne Lay

Abstract Short-period seismic recordings at regional and upper mantle distances from underground explosions at Novaya Zemlya demonstrate that propagation across the continental shelf under the Barents and Kara Seas appears to modify the partitioning of energy between L_g and S_n phases relative to purely continental paths in the Eurasian crust. While the underwater segments of the paths are relatively short, variations in bathymetric characteristics from path to path influence the regional wave field, with systematic behavior that can be used to establish empirical amplitude corrections for regional phases. We analyze a large set of Eurasian recordings to explore the relationship between regional phase energy partitioning and bathymetric characteristics. Maximum water depth along the path is the most influential factor for the Novaya Zemlya data. It has strong linear correlations with the logarithmic rms amplitude of L_g and the ratios S_n/L_g and P/L_g . The maximum water depth probably reflects the extent of necking of the crustal wave guide under the continental margin, which may disrupt L_g modes resulting in L_g to S_n scattering, but there is surprising sensitivity to small variations in bathymetry. Empirical relations like those found here may be useful for nuclear yield estimation and discrimination for regions such as the Korean Peninsula and Persian Gulf, where many seismic phases traverse water-covered continental shelf with poorly known crustal structure.

Introduction

The short-period regional seismic phase L_g , comprised of Rayleigh wave overtones or postcritical multiply reflected S waves, has long been known as a "continental phase." In fact, its first applications were for discriminating continental and oceanic crust based on the presence or absence of the L_g phase, respectively (Press and Ewing, 1952). Oliver *et al.* (1955) used such bimodal classifications to investigate the crustal structure in the Arctic, while Savarensky and Valdner (1960) studied the Black Sea region. These studies concluded that in no case does L_g propagate through crust overlain for any significant distance by water deeper than 1000 fathoms (1.8 km). Thin oceanic crust is now well known to inhibit L_g propagation (e.g., Kennett and Mykkeltveit, 1984), but the effects of transitional crustal structures are not as clear.

It was quickly recognized that propagation across a marginal sea or continental shelf does not completely quench L_g , but can reduce its amplitude. A number of studies have been conducted for L_g traversing paths under shallow water. Wetmiller (1974) investigated the

crustal structure in the Baffin Bay area, and Gregersen (1984) studied the crustal structure near Denmark and the North Sea. Kennett *et al.* (1985) then examined heterogeneity of the North Sea basin using variability of L_g transmission. Recently, Baumgardt (1990) explored L_g blockage and scattering by the Barents Sea and White Sea, recognizing the importance of energy partitioning between L_g and S_n in the regional wave field. He inferred that the presence of thick sedimentary basins plays a critical role in L_g blockage. Nuttli (1988) analyzed L_g phases on similar paths across the Barents Sea, with only moderately strong attenuation values being found for the blocked arrivals, and their relative yield-amplitude scaling appearing to be unimpaired. Theoretical studies of propagation across continental margins have been conducted by Kennett (1986), Maupin (1989), Regan and Harkrider (1989), and Cao and Muirhead (1993). The latter study used P - SV finite difference calculations to demonstrate that necking of the crust and the presence of the thin water layer can effectively block L_g . Many additional studies have examined variations in L_g and S_n

transmission efficiency in diverse continental environments (e.g., Ruzaikin *et al.*, 1977; Kadinsky-Cade *et al.*, 1981; Ni and Barazangi, 1983; Lynnes and Baumstark, 1991).

These important studies have provided insight into the complex structural controls on L_g in a heterogeneous transitional crust, but we still lack a practical means by which to account for the strong amplitude and spectral effects of underwater segments for regional arrivals. This is particularly important for efforts to monitor underground explosions of low yield and to discriminate them from earthquakes using regional phases. The strong variability of regional discriminants (e.g., Pomeroy *et al.*, 1982; Lynnes and Baumstark, 1991) mandates correction for path properties affecting regional phase amplitudes and spectral content.

The water in most parts of the North Sea, Barents Sea, and Kara Sea is shallower than 200 m. The thinning of the crustal wave guide under the shelf is small (except in the central rift of the North Sea) relative to the typical 30- to 40-km thickness of the adjacent continental crust. However, L_g waves do have highly variable transmission efficiency through these water-covered regions. This implies that there must be significant changes in the crustal structure or in the shallow sediments underlying the marginal seas that affect the regional wave field.

This study explores the influence of the bathymetric structure of the Barents Sea and Kara Sea on regional phase propagation. The approach taken is an empirical one, given that current capabilities for realistically simulating regional waveforms are quite limited, as is our detailed knowledge of the regional crustal structure. One of the major obstacles confronting nuclear nonproliferation monitoring is the variability of regional wave energy flux associated with diverse paths in the crust. If it is possible to develop reliable empirical approaches that use surface observations such as path topography or bathymetry to account for some of the wave field variability, more effective procedures for global monitoring may be achieved. For example, Zhang and Lay (1994) have recently discovered surprisingly strong empirical relationships between regional phase-amplitude ratios and along-path topography statistics for Eurasian continental paths. In this spirit, our analysis involves seeking simple path parameters that provide a basis for reducing wave field variations associated with propagation through the crustal structure underlying a shallow sea. Quantitative modeling of any such relationships will be pursued in the future.

Data

The seismic data that we use are recordings of 20 underground nuclear explosions located in the Novaya Zemlya test site near Matochkin Shar (the narrow strait that separates the northern and southern islands of No-

vaya Zemlya). The events occurred from 1964 to 1988. Short-period regional and upper mantle distance recordings from Soviet-run stations were collected and digitized for these events as part of a data exchange associated with the Joint Verification Experiment. The locations of the test site and stations providing sufficient numbers of recordings and instrument response information for our analysis are shown in Figure 1. Topography contours for Eurasia are included, derived from digital elevation data supplied at 5-min intervals from a world topography data base (ETOPO5, compiled by the National Geophysical Data Center, Boulder, Colorado). The stations range in distance from 1900 to 3600 km, and provide the most extensive data set for Novaya Zemlya explosions available from the Eurasian mainland. Most previous studies of short-period regional phases from explosions at this test site have used array data from Norway, Germany, and Finland (e.g., Baumgardt, 1990; Ringdal and Fyen, 1991) or from isolated stations in western Europe and Scandinavia (Nuttli, 1988), which sample a very restricted azimuthal range from the test site. The exchange data provide an extensive data set with broad azimuthal coverage, including paths with diverse underwater segments.

Figure 2 shows detailed bathymetry of the region around Novaya Zemlya, with the Barents Sea to the west and the Kara Sea to the east. The ray paths to the exchange stations sample different paths through these marginal seas. This provides a basis for exploring the relative waveform effects of different underwater segments. The previous work on Novaya Zemlya regional data mentioned above has primarily used paths traversing the deeper water regions of the Barents Sea (toward the west in Fig. 2).

Only vertical-component seismograms have been digitized for the exchange stations, but the general signal quality is quite good (Israelsson, 1992). Altogether, 108 waveforms from the 20 explosions recorded by eight stations are used in the analysis. The instrumentation is comparable between stations, but there are slight variations in frequency response, as well as variations with time at each station. To equalize the instrument characteristics, we deconvolved the individual instrument responses from each waveform, and then convolved the ground motion with the 1988 response of the CKM-3 seismometer at station OBN. For some of the data, portions of the records are missing; we use only the phases which are reliably digitized. Many details about the specific explosions, the exchange data set, and the signal quality are given by Israelsson (1992). We combine data from different events to characterize average path properties, and so do not dwell on the individual event information.

Our primary interest is to explore whether energy partitioning in the regional wave field is influenced by the variation in underwater path segments. To achieve

this, we require robust measurements of the short-period wave field. Previous studies have established the stability of gross averaging measures such as rms calculations for regional phases (e.g., Ringdal *et al.*, 1992; Hansen *et al.*, 1990; Israelsson, 1992; Zhang and Lay, 1994), so we use comparable measurements in this study. The rms values for different phases were calculated using the instrument-equalized traces, with bandpass filtering between 0.6 and 3.0 Hz. These frequency limits conform to routine regional phase passbands used by Hansen *et al.* (1990) and are compatible with the limitations of the hand-digitized data.

The rms amplitudes of each phase are calculated in corresponding group velocity or time windows. The L_g is assigned the window 3.1 to 3.7 km/sec, following Israelsson (1992), while the S_n window is 4.3 to 4.8 km/sec, as preferred by Kennett (1989) (see Fig. 4 for an example). We found that use of a narrower L_g window of 3.1 to 3.5 km/sec had only minor effects on the measurements in this study. We use time windows for the P waves, which at the upper mantle distances spanned by

our data have impulsive first arrivals followed by complex coda. We use both 0- to 5- and 0- to 50-sec windows from the onset of the P arrivals. The latter part of the 0- to 50-sec window contains an increasing component that is multiply reflected within the crustal wave guide, but the primary energy dives into the upper mantle. A noise correction was applied to each measurement (Zhang and Lay, 1994), obtained from the rms amplitude of the available signal prior to 5 sec preceding the manually picked P onset (usually 115 sec of data). A comparably measured data set for underground explosions at the Semipalatinsk test site, comprised of 325 waveforms for 83 explosions from the JVE exchange (Zhang and Lay, 1994) is used for comparison with the Novaya Zemlya observations. The paths associated with those data are indicated in Figure 1.

Characterization of Paths

The islands of Novaya Zemlya are an extension of the Ural mountains, commonly identified with the

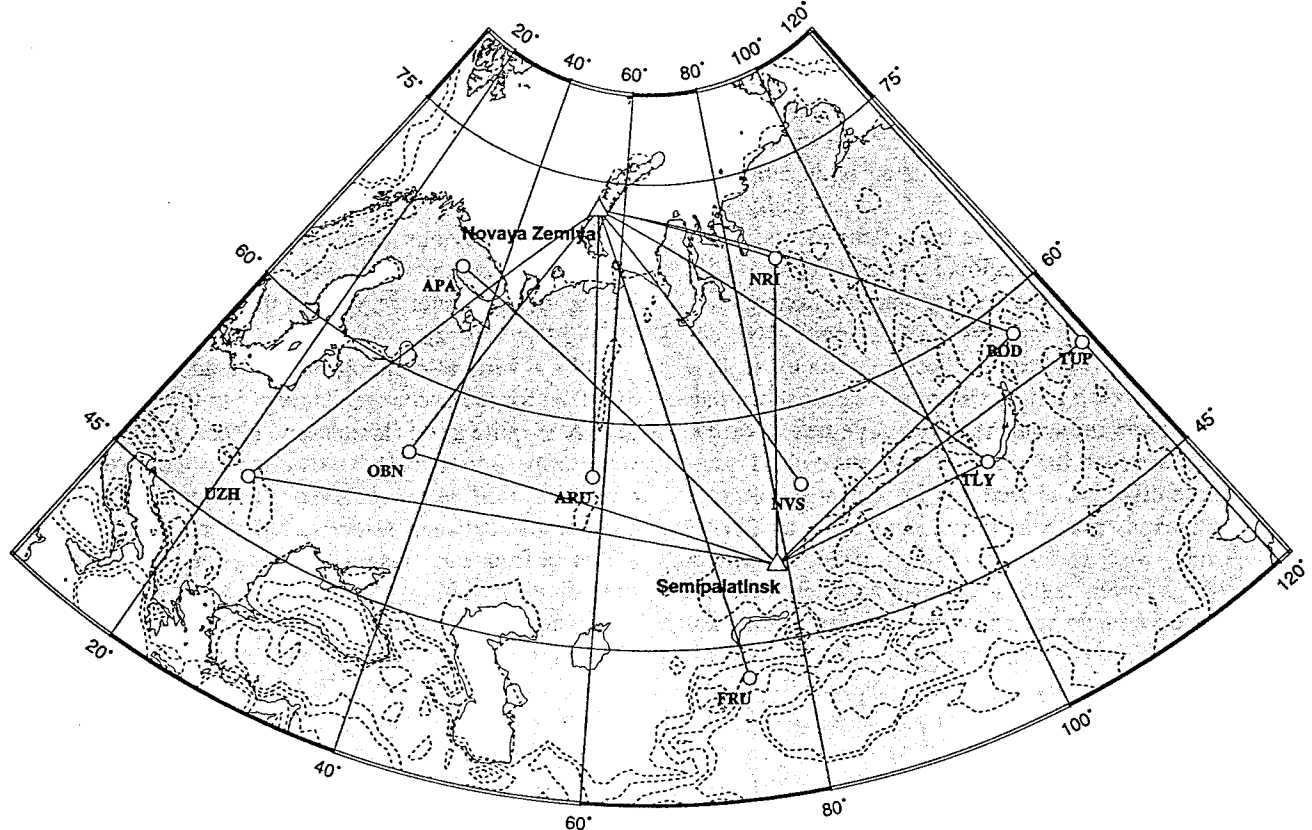


Figure 1. Map showing the locations of the Novaya Zemlya and Semipalatinsk test sites, marked with triangles, and the seismological stations used, marked with circles and indicated by their codes. The lines between the sources and receivers correspond to great-circle paths. Topography is indicated with contour intervals every 1000 m from -1000 to 3000 m above sea level, but 500 m contour is added to show Ural and other low mountains. Plotting software from Wessel and Smith (1991) is used in this and the next two figures.

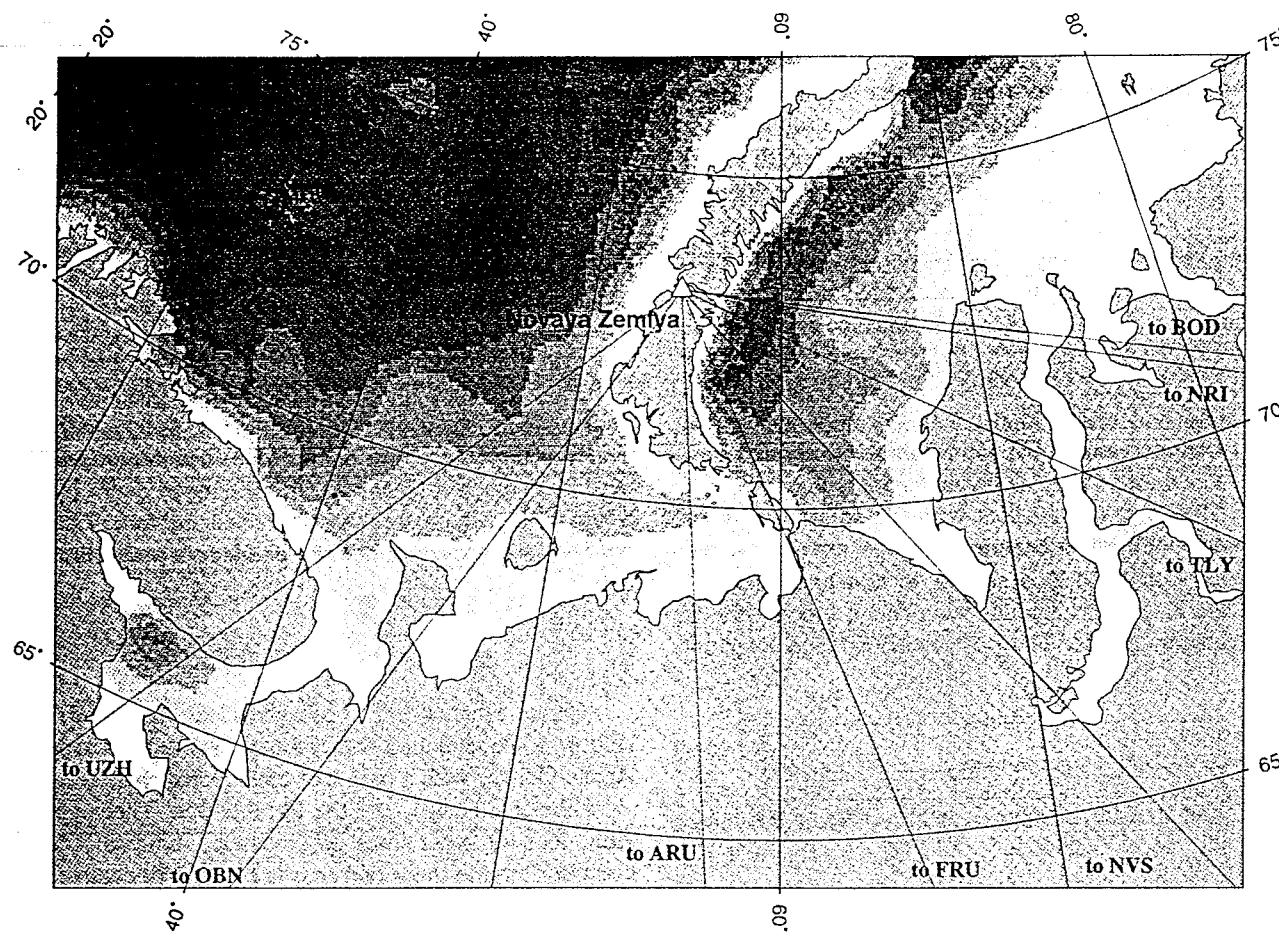


Figure 2. Map showing bathymetry around Novaya Zemlya, and great-circle paths from the test site to each Eurasian station used. The contour interval assigned to each gray-shade is 50 m. The Barents Sea is to the west of the island, and the Kara Sea to the east. The paths traverse the continental shelf with depths ranging from 50 m to a maximum of 350 m (east of the island).

Table 1
Bathymetric Statistics of the Paths

Path	Mean Depth (m)	Length (km)*	Max. Depth (m)	Area (km ²)†
BOD	111	420	341	46.9
NRI	108	420	338	45.3
TLY	126	420	278	52.8
NVS	116	590	337	68.4
FRU	220	280	340	61.6
ARU	41	230	116	9.5
OBN	6	450	129	27.1
UZH	87	710	171	61.7

*Total underwater length.

†Cross-sectional area of the underwater segment.

boundary between Europe and Asia. The eight paths from Novaya Zemlya to Eurasian stations sampled by our data are readily divided into two groups. Three paths, to UZH, OBN, and ARU, cross the southeast Barents Sea (Fig. 2), where the maximum water depth is 100 to 150 m. We call this the Barents group. There is a relatively deep-

water zone off the east coast of Novaya Zemlya, in the southern Kara Sea. Paths to FRU, NVS, TLY, NRI, and BOD traverse this deeper water, where the maximum depth is about 300 m (Fig. 2). This is the Kara group. Each path has slightly different underwater segment characteristics, which we will consider. These include mean depth, total underwater length, maximum depth, and the cross-sectional area of the underwater segment, the values for which are given in Table 1.

The entire propagation path influences the regional wave field, and in this case all of the paths have significant segments across the Russian platform. While details of the crustal structure on each path are at best very sketchy, a possible guide to relative structural characteristics is provided by surface topography. The topography profiles, from the ETOPO5 data base with 10-km lateral sampling, are shown for each path in Figure 3. The island source region is on the left of each profile and the station is on the right. There is a large vertical exaggeration, but in most cases the underwater segments

are minor features relative to the continental relief along the paths.

The path to BOD has a mean water depth of 111 m, and a maximum water depth of 341 m, similar to the other four paths in the Kara group. The pathlength across the sea is 420 km. We do not include the pathlength under shallow water bodies along this path like Obskaya bay and Yeniseyskiy gulf. The western half of the BOD on-land path is flat, on the Siberian lowland. When the path intersects the Vilyuyskoye Plateau, the altitude rises and the surface becomes quite rough. On the basis of the work by Zhang and Lay (1994), we anticipate that this topography will reflect changes in the wave guide that affect the propagation of regional phases, although possibly not as dramatically as the underwater segment. The path to NRI almost coincides with the west half of the BOD path, ending just before the rough topography begins. The path to TLY is similar to that to BOD, with the southern segment encountering rough topography in the Sayan mountains. The path to NVS has a long un-

derwater segment, as it traverses Baydaratslaya bay, the southernmost part of the Kara Sea. The on-land segment is quite flat. The path to FRU has the greatest mean water depth (220 m) and a maximum depth of 340 m (Table 1). Its on-land segment crosses the Ural mountains and then traverses the huge Siberian plane, before encountering the high-altitude Pamir mountains. Unfortunately, there is only one record available from FRU.

The paths of the Barents group have relatively shallow underwater segments. The path to ARU runs along the Ural mountains for a few hundred kilometers, which is likely to affect the regional phase propagation. The path to OBN has a very shallow mean water depth and a flat on-land path. The path to UZH has the longest underwater segment (710 km), but the mean depth is only 87 m. This path crosses the White Sea and Lake Ladoga, but we have only summed the pathlength under the Barents Sea.

Examination of Path Effects

Oliver *et al.* (1955) observed clear L_g arrivals at a station in Copenhagen from an earthquake located in the Arctic Ocean, with a path that crosses the Kara Sea, Novaya Zemlya Island, and the Barents Sea. Their conclusion, and all other lines of evidence, indicate that the crust underlying these two seas is essentially continental. The water depth between Novaya Zemlya and the Eurasian mainland is never more than 350 m, and L_g energy is not totally blocked. Yet, we find that traversing the underwater segment appears to substantially modify the energy partitioning in the short-period regional wave field, as has been previously demonstrated for paths to Europe (e.g., Baumgardt, 1990). The clearest evidence for this is provided by comparison of Novaya Zemlya recordings with Eurasian recordings of events at other Soviet test sites.

In order to evaluate the effects of the underwater paths, we compare the seismograms from Novaya Zemlya events with recordings of Semipalatinsk explosions from the same Eurasian stations. The latter involve almost entirely on-land paths (Fig. 1). Figure 4 shows representative waveforms at similar distances for recordings of a Novaya Zemlya event at station OBN (*top*) and a Semipalatinsk event at the same station (*bottom*). To emphasize the relative energy distribution in the short-period signals, the times scales are modified to have common group velocity scales from 9.0 to 2.8 km/sec. The general structural characteristics of each path, as manifested in surface topography and geologic provinces traversed, are quite similar, apart from the short underwater segment for the Novaya Zemlya data (Fig. 1). The waveform from the Semipalatinsk event has a clear L_g wave packet in the group velocity window of 3.7 to 3.1 km/sec, with a maximum near 3.5 km/sec. The S_n window has very weak energy, indistinguishable in this

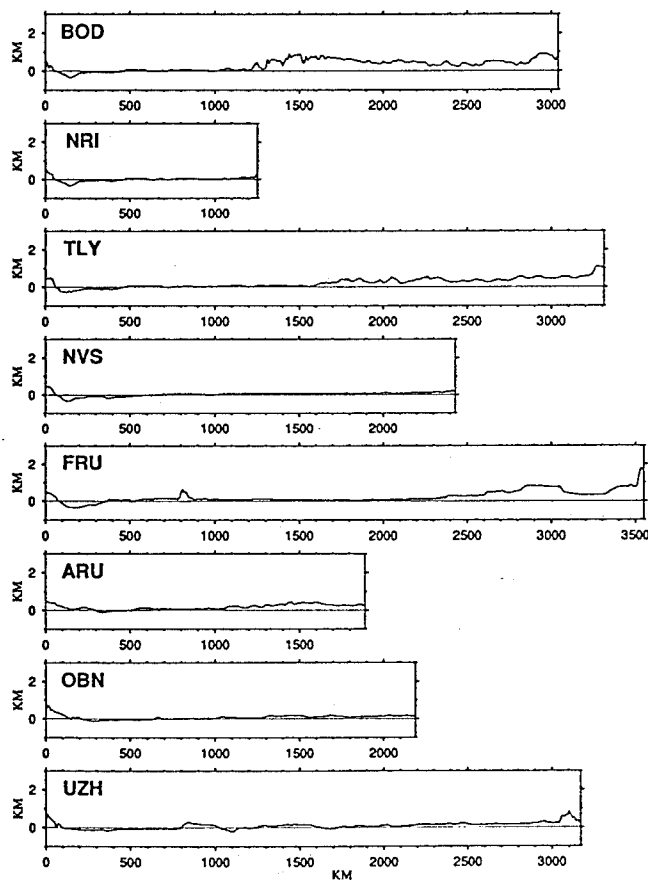


Figure 3. Profiles of surface topography from the ETOPO5 data base along paths between the Novaya Zemlya test site and the eight Eurasian stations shown in Figure 1. The units of horizontal and vertical axes are both kilometers, but the vertical scale is exaggerated by a factor of 110. The dotted lines are sea level.

passband from the P coda. The L_g window for the Novaya Zemlya event has lower signal to noise ratio but there is clearly energy in the interval. There is relatively high-amplitude energy in the latter part of the S_n window. The corresponding path traverses the shallowest water segment amongst the various Novaya Zemlya paths, but even in this case the overall difference in the short-period energy distribution is apparent.

The differences seen in Figure 4 are common to the large data sets for each test site. To illustrate this we use a simple measure, picking the group velocity at which each waveform amplitude peaks in the range 5.0 to 2.8 km/sec. Comparisons of such measurements for a large suite of explosions at the two sites are shown in Figure 5. Crosses indicate the group velocity of the peak rms amplitude in a moving 8-sec window for Semipalatinsk recordings, while circles are for Novaya Zemlya data. Almost all Semipalatinsk measurements are within the 3.7 to 3.1 km/sec range, corresponding to the L_g window. However, most Novaya Zemlya measurements are in the 4.6 to 3.8 km/sec range, which is the latter part of the S_n (4.8 to 4.3 km/sec) window, and in what Zhang

and Lay (1994) define as the S_n coda window (4.3 to 3.7 km/sec). While the separation is on average very clear, despite the variety of paths involved, there are a few interesting exceptions. For the Semipalatinsk data, the two records on the path to APA have peak amplitudes at group velocities higher than 4.0 km/sec. This path is very long and unusual in that it traverses the White Sea just before reaching the station (Fig. 1). Although the maximum depth of the White Sea is only 48 m, the fact that S_n is larger than L_g , as is observed for Novaya Zemlya records, is noteworthy. For the Novaya Zemlya data, some of the records at stations ARU and FRU have peak amplitudes at low group velocities. These paths are close to the underwater extension of the Ural mountains, where the crust is likely to be relatively thick.

The distance ranges spanned by the Semipalatinsk and Novaya Zemlya recordings are comparable, but there are some differences in the amplitude variations of the regional phases with distance. For Novaya Zemlya, the rms amplitude in the S_n window of 4.8 to 4.3 km/sec is considerably enhanced relative to Semipalatinsk data. In Figure 6, squares indicate the mean rms S_n amplitudes from Semipalatinsk, while circles are for Novaya Zemlya. The values are computed after equalizing the event

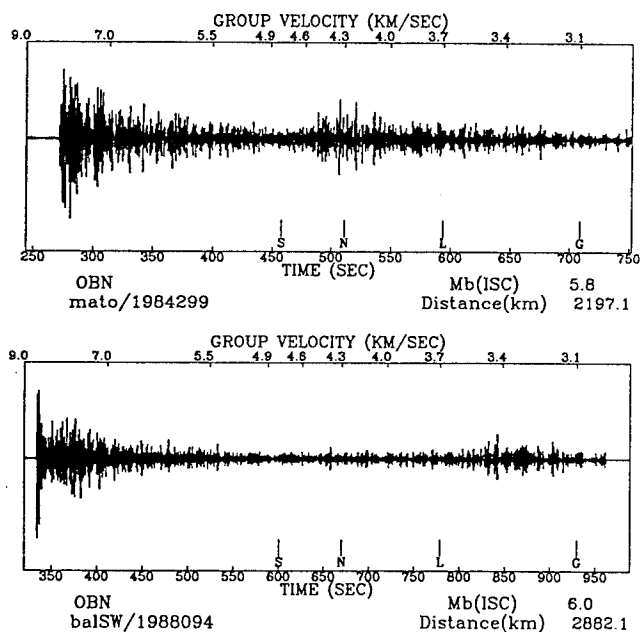


Figure 4. Representative seismograms for recordings on the Semipalatinsk-OBN path (below) and the Novaya Zemlya-OBN path (above). The waveforms are bandpass-filtered between 0.6 and 3.0 Hz. The time scales are slightly different so that the two signals, which are at different distances from the sources, can be put on the same group velocity scale (indicated at the top of each plot). The vertical lines mark the windows used to calculate rms amplitudes. The S to N interval corresponds to the S_n window of 4.8 to 4.3 km/sec, and L to G indicates the L_g window of 3.7 to 3.1 km/sec. Notice the relatively strong S_n for the Novaya Zemlya event recording.

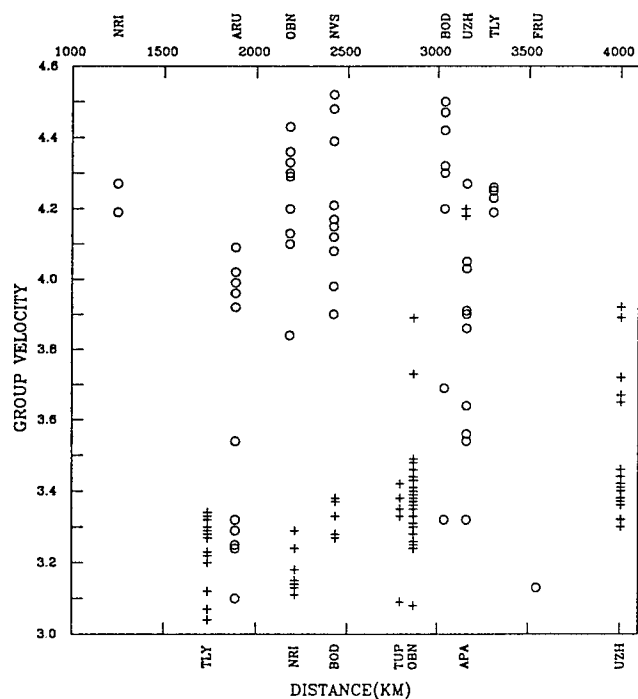


Figure 5. A summary plot indicating the group velocity at which a running average amplitude in an 8-sec window has a maximum value for each seismogram. The measurements are plotted versus distance from each test site, with circles for Novaya Zemlya data (stations are labeled at the top), and crosses for Semipalatinsk data (stations are labeled at the bottom). The group velocity range considered is from 5.0 to 3.0 km/sec.

sizes by scaling the measurements to a common teleseismic m_b of 5.0. The S_n is generally stronger for the paths that cross underwater segments. Strong S_n was observed by Kadinsky-Cade *et al.* (1981, Figs. 12, 13 of that article), for paths across the Caspian Sea and Black Sea. They found that the attenuation factors for S_n and L_g are not consistent in that region, but they did not conclude that the S_n is enhanced. Baumgardt (1990) suggests that the late S_n and S_n coda windows may be enhanced for paths traversing underwater segments due to L_g to S_n scattering, so it is possible that the Novaya Zemlya rms values are enhanced in an absolute sense. It is also clear from Figure 6 that the S_n energy for Novaya Zemlya exhibits a different distance decay. Some of the S_n observations from Semipalatinsk tend to traverse regions with rough topography associated with the Sayan mountains and lake Baikal (Zhang and Lay, 1994), thus, their amplitudes and distance behavior may be anomalous, relative to the comparatively flat paths for the Novaya Zemlya data.

Similar comparisons of mean rms L_g amplitudes on paths for Novaya Zemlya (solid circles) and Semipala-

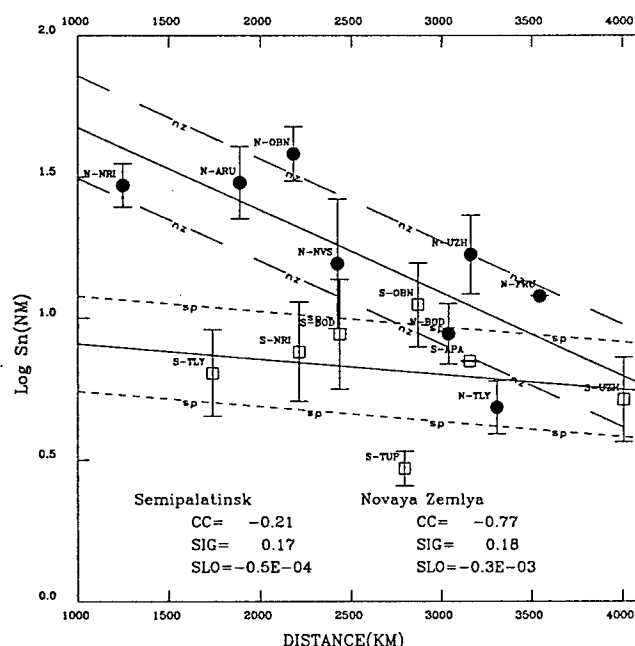


Figure 6. A plot of the mean S_n amplitudes and their standard deviations on each path versus path distance, where all events have been equalized to a common $m_b = 5.0$. Squares are for Semipalatinsk data, and circles are for Novaya Zemlya. The observed S_n amplitudes from Novaya Zemlya tend to be higher and show a stronger distance trend. Regressions for the trend with distance are shown. For each regression, CC gives the correlation coefficient, SIG the standard deviation, and SLO the regression slope. The regression curves are indicated by solid lines. Dashed lines mark the one-standard-deviation limits, $\pm \sigma$.

insk (open squares) events are shown in Figure 7. The events are again equalized to a common m_b of 5.0. The absolute amplitude levels are not systematically different overall, in contrast to the S_n measurements; however, the Novaya Zemlya data exhibit somewhat greater variability. We calculated the standard deviation of the distance trends for the L_g amplitudes for Novaya Zemlya and Semipalatinsk data separately, finding that the standard deviation for Novaya Zemlya data is about twice that for Semipalatinsk (0.29 and 0.14, Fig. 7). The long and short dashed lines indicate the standard deviations for the two data sets, respectively. Four of the Novaya Zemlya data points, for stations NRI, NVS, BOD, and TLY, are near the lower dashed line. These all belong to the "Kara group"—the deep-water group, and it would appear that on average the L_g amplitudes are reduced for these paths relative to the Semipalatinsk data. Of the four Novaya Zemlya points near the upper line, three (ARU, OBN, and UZH) are from the "Barents group"—the shallow-water group. The only exception to this grouping is FRU, for which there is only a single observation. Uncertainty in instrument gains may contribute to some of the scatter in Figures 6 and 7, since some stations tend to plot consistently high or low in each population.

While there are clearly many possible factors influencing these regional phases, we are very limited in our ability to quantitatively model almost all of them, including likely factors such as differences in excitation associated with the near-source properties at the two test sites. We will emphasize the relative, apparently path-

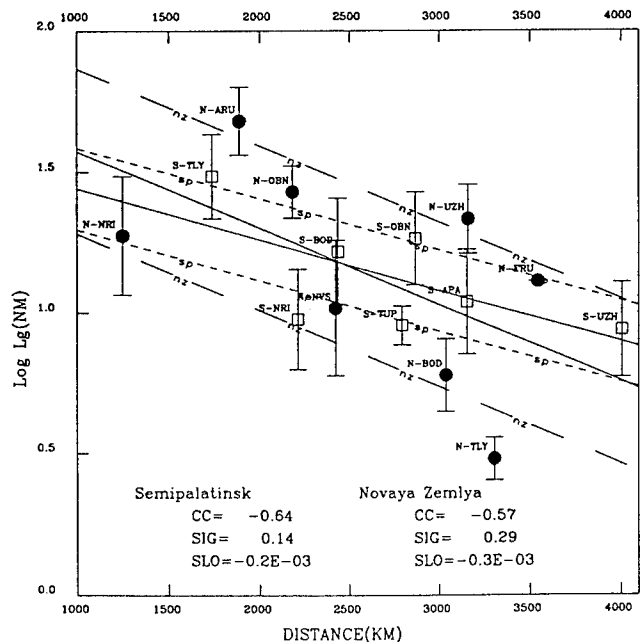


Figure 7. Similar to Figure 6, but for L_g amplitudes. The observed L_g amplitudes from Novaya Zemlya are scattered more than those from Semipalatinsk.

dependent variations, as these can be treated somewhat independently of the absolute excitation issues. In previous studies of the Semipalatinsk data set, the L_g phase has been demonstrated to be relatively stable (Israelsson, 1992; Zhang and Lay, 1994), but the ratio of S_n/L_g was found to have a strong correlation with the mean altitude and roughness of the path to each station (Zhang and Lay, 1994). Figure 8 shows the correlation of the rms amplitude ratio S_n/L_g with average path roughness (standard deviation) estimated from theETOPO5 data base, for the Semipalatinsk and Novaya Zemlya data separately. Note the very strong correlation for Semipalatinsk, and the relatively large range of roughness sampled by the different paths (details are given in Zhang and Lay, 1994). One interpretation is that the surface roughness provides a surrogate for irregularities of the crustal wave guide, which influence the energy partitioning between S_n and L_g along each path. In contrast, the Novaya Zemlya data do not show a corresponding relationship, despite the fact that many of the paths traverse similar Eurasian structure. In part, this may reflect the fact that the overall variation in path roughness is reduced for the Novaya Zemlya data set, but we suspect that a more important factor is the variability associated with the differences in underwater segments, which appears to overwhelm the on-land effects. We will test whether we can isolate any such effect.

We use the four underwater path parameters, mean depth, underwater length, maximum depth, and underwater cross-sectional area, tabulated in Table 1, to characterize the variations in shelf segment. Our strategy is to correlate the amplitudes, and amplitude ratios, of each phase with the four factors. Figure 9 shows the result for average rms L_g measurements at each station, which have been normalized to a common $m_b = 5.0$ and then corrected for distance according to power law $r^{-5/6}$ (Nuttli, 1973). The latter correction is only for geometric spreading, and ignores effects of attenuation, which will be considered later. Mean depth (Fig. 9a) and underwater area (Fig. 9d) have moderate correlation with L_g ampli-

tude variations. The length of water segment (Fig. 9b) shows no pattern. Maximum water depth (Fig. 9c) shows the strongest pattern among the four factors, with the Barents group (ARU, OBN, and UZH) clustering on the left, while the Kara group (TLY, NVS, NRI, FRU, and BOD) clusters on the right. The Kara group involves observations spanning a large distance range. A factor of 3 difference in amplitudes is involved, corresponding to the large scatter in Figure 7. Mean depth, maximum depth, and cross-sectional area are all correlated, but it appears that maximum depth is particularly important, more so than the length of the water segment. Mean depth would have a much stronger correlation if the single observation at FRU were omitted.

Very similar results are found for rms S_n amplitudes (Fig. 10). The same geometric spreading correction has been applied to the S_n data. The S_n amplitude also decreases with increasing maximum water depth, but the amplitude variations are somewhat less than for L_g .

If wave guide properties associated with water depth are in fact important for the regional wave field, we would expect there to be no correlation with rms amplitude variations in the early part of the direct P arrivals at our stations, which are at upper mantle triplication distances. The P -wave coda should involve scattered arrivals, some of which originate in the L_g and S_n windows, so there could be some sensitivity to the path properties. Figure 11 shows the varying degree of correlation between amplitudes of each phase and the maximum water depth. Because of the upper mantle distance ranges involved, no simple distance correction is realistic for the P -wave windows, so in this comparison we make no geometric spreading correction for S_n or L_g . Comparison with Figures 9 and 10 indicates that the geometric spreading corrections used for the latter two phases are actually not very significant relative to the trends found with maximum water depth. Even without any distance correction, L_g has the greatest slope and correlation coefficient with maximum depth, followed by S_n , and then the 0- to 50-sec P -wave window, which includes substantial P coda.

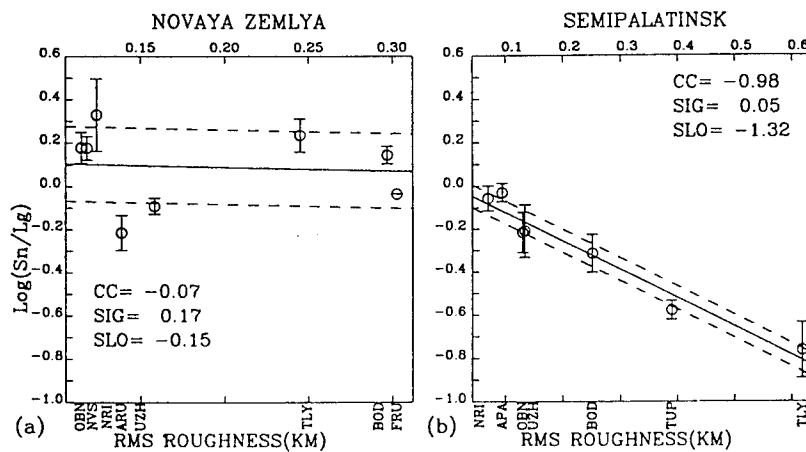


Figure 8. Empirical relation between the rms amplitude ratio of S_n/L_g versus along-path topographic roughness (variance) for observations from the Semipalatinsk source region (right) and the Novaya Zemlya source region (left). The strong trend on the right was first reported by Zhang and Lay (1994), and indicates that irregularities in the wave guide structure influence the regional phase energy partitioning. The lack of a strong trend on the left indicates that additional factors, presumably associated with the underwater segments of the paths, dominate in the Novaya Zemlya data.

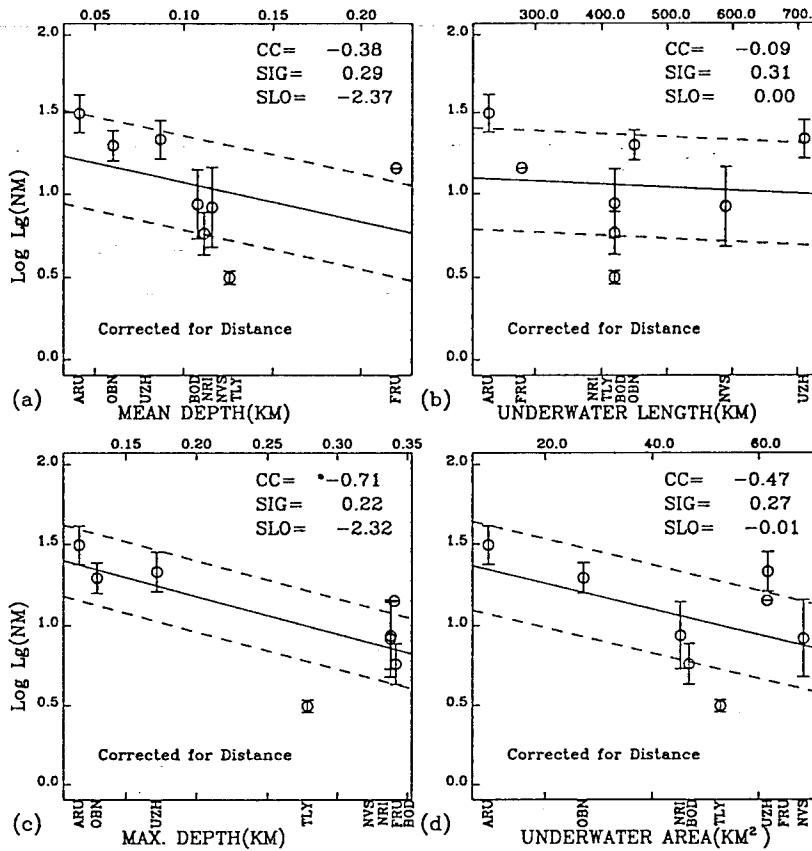


Figure 9. Correlation of rms L_g amplitudes from the Novaya Zemlya explosions with four parameters that characterize the underwater segments of each path, mean depth, underwater length, maximum depth, and underwater area. The data are mean values on each path, after equalizing the source strengths to a common $m_b = 5.0$, and correcting for distance. The geometrical spreading factor for L_g is approximated by the power law $r^{-5/6}$ (Nuttli, 1973).

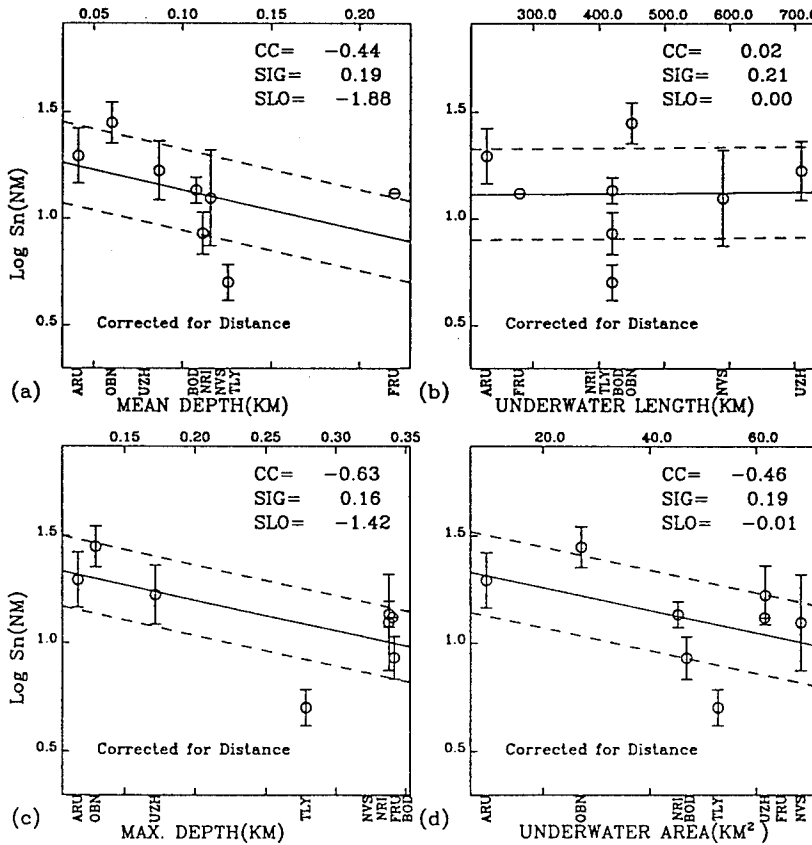


Figure 10. Similar to Figure 9 but for S_n amplitudes. The $r^{-5/6}$ correction is still used. The results are close to those in Figure 9, but the correlation and trend with maximum depth are a little weaker.

The direct 0- to 5-sec P -wave rms amplitude has no correlation with the water depth, as expected. Note that station TLY, a consistent outlier for both S_n and L_g , is also low for P , suggesting a receiver site effect or possibly an error in the instrument corrections and/or gains provided in the data exchange.

Given the complex nature of geometric spreading and path effects, we can better explore energy partitioning by examining rms ratios. Ratios are also of importance because ratios such as P/L_g are being explored as the main regional discriminant between nuclear explosions and earthquakes. We seek to establish whether such ratios are affected by the water segment. We expect that ratios for regional phases may be affected by average path properties, as shown in Figure 8, and we can explore whether applying corrections for the on-land portion of the paths enhances the sensitivity to the underwater segments. Figure 12 shows results for the S_n/L_g ratios, correlated with the four underwater parameters. The S_n/L_g has a fairly strong relationship with maximum depth, which can be attributed to the stronger trend in Figure 9 versus Figure 10. Note that the elimination of any site effect for TLY tightens up the trend. Also note that the single observation at FRU should be down-weighted.

From Figure 1 it is clear that the on-land path segments are much longer than the underwater segments.

We use the correlations between S_n/L_g and P/L_g and on-land topographic roughness of the path found in our previous study (Zhang and Lay, 1994) to make corrections for on-land roughness for the Novaya Zemlya data. Since the range in path roughness is relatively small (see Fig. 8), these corrections are not very large, but one should observe an improvement in the correlations with underwater properties if the on-land contributions are in fact suppressed. The results for S_n/L_g after correction for roughness (relative to the path to ARU) are shown in Figure 13. The correlations of S_n/L_g ratios with mean depth, maximum depth, and water area are all actually improved, lending credibility to the influence of the underwater segment. The strong effect associated with water depth does in fact appear to be responsible for the poor correlation with overall path roughness for these data found in Figure 8.

Since L_g shows a trend with underwater properties, while the 0- to 5-sec P window does not, the presence of correlations in the P/L_g ratio (Fig. 14) is no surprise. Because the Semipalatinsk data span comparable distance ranges, it is possible to use the relationship found by Zhang and Lay (1994) for P/L_g versus continental path roughness to make a correction, but this effectively corrects only for the L_g wave. It is interesting to see (Fig. 15) that application of this correction does in fact reduce the scatter in the relationship with the underwater path

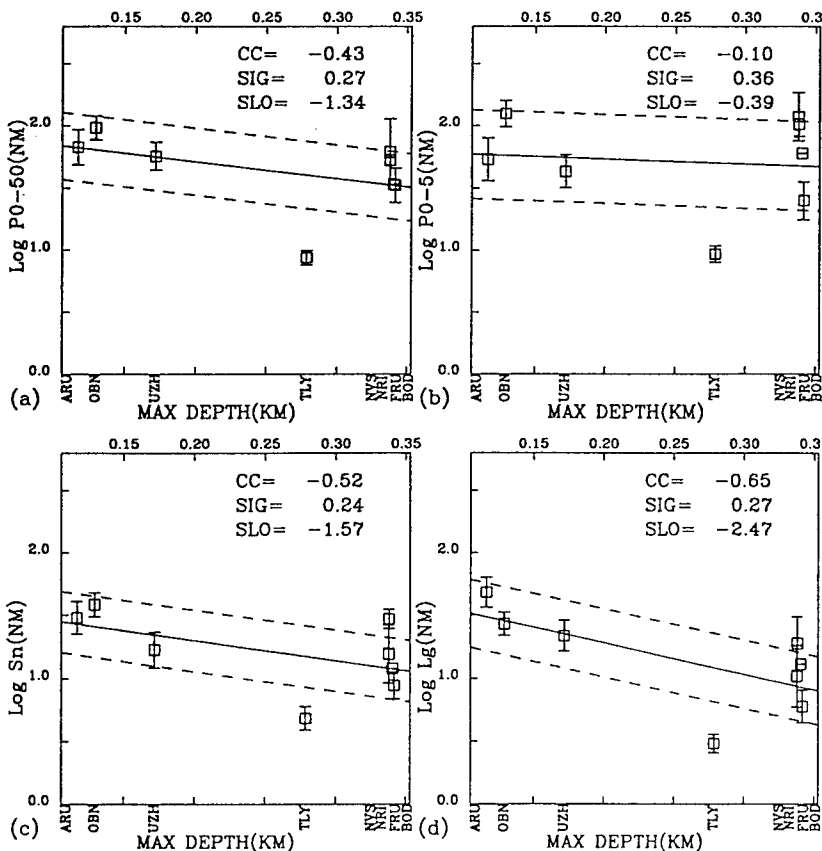


Figure 11. (a) through (d) Comparison of relationships between rms amplitude measurements for different phases in the short-period signals and maximum water depth on each path. No distance corrections are applied to any of the phases in this case. The direct P window, measured for the first 5 sec of the waveform, is shown in (b), and no relationship to the water depth is seen. A weak trend is found for a long, 0- to 50-sec P window, which includes substantial coda, and stronger trends are found for S_n and L_g .

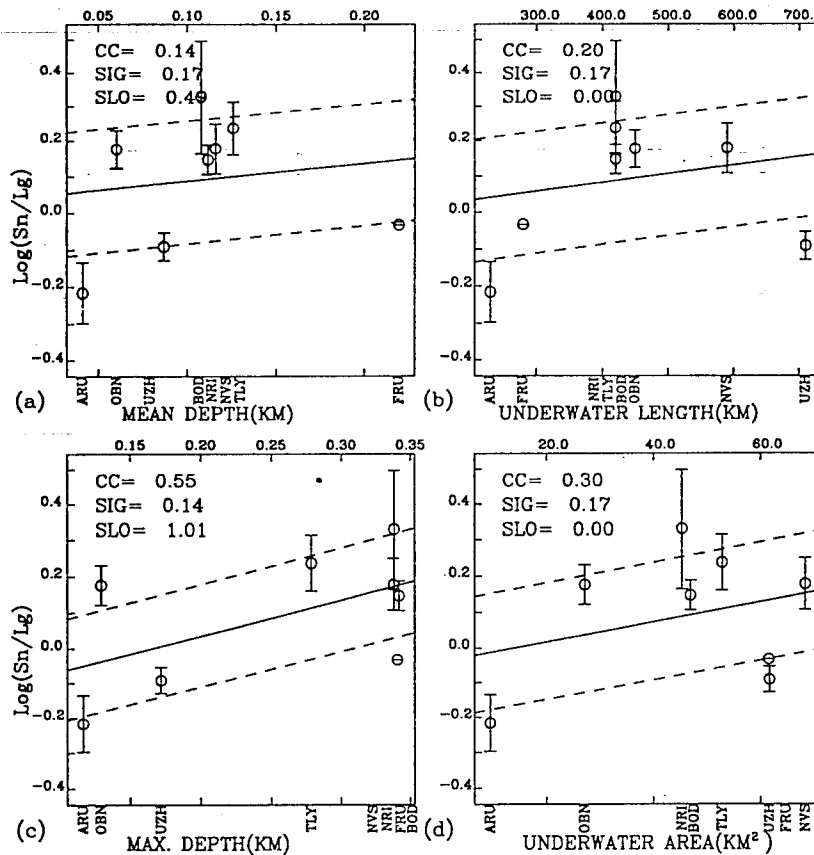


Figure 12. Correlations between S_n/L_g ratios and the four underwater path parameters.

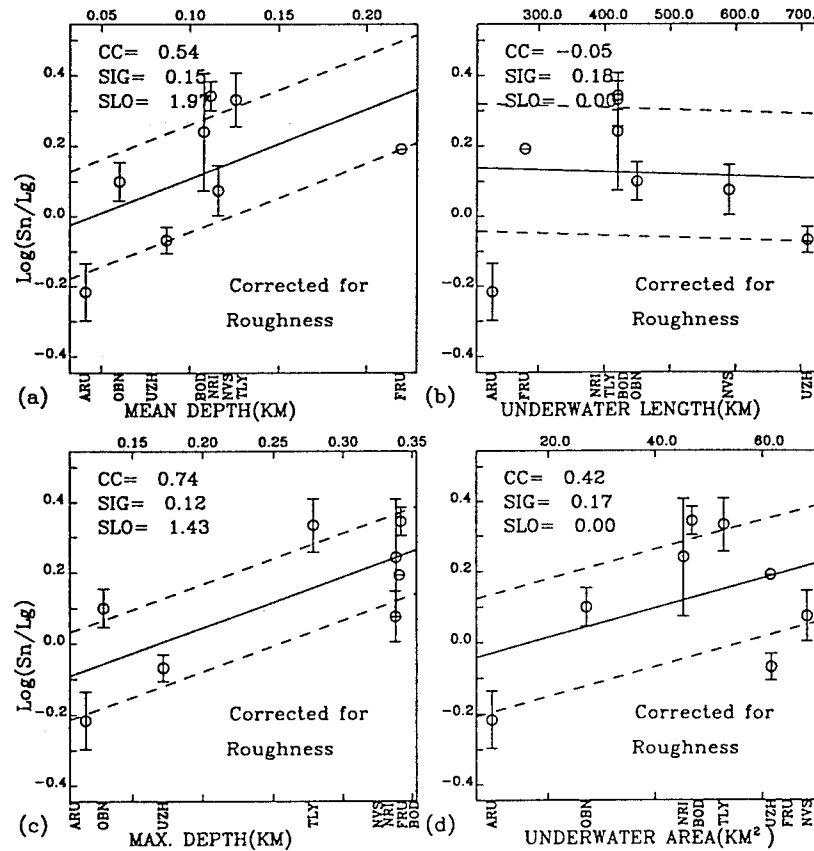


Figure 13. Similar to Figure 12, but now the S_n/L_g ratios have been corrected for relative path roughness, using the continental path correlations found for Semipalatinsk data by Zhang and Lay (1994).

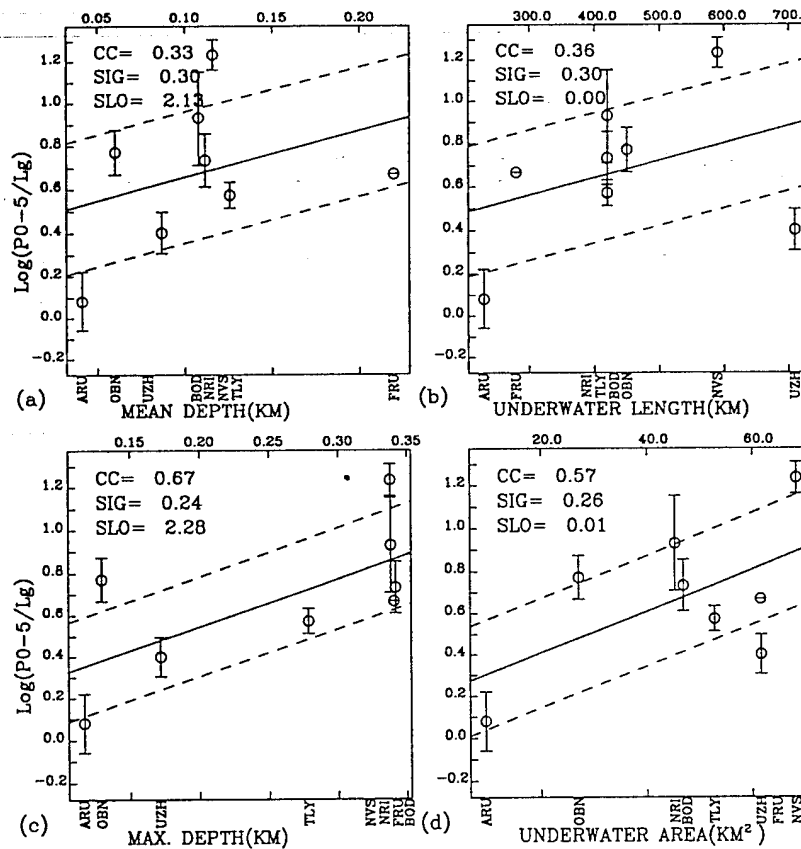


Figure 14. Correlations between P/L_g and the four underwater path parameters.

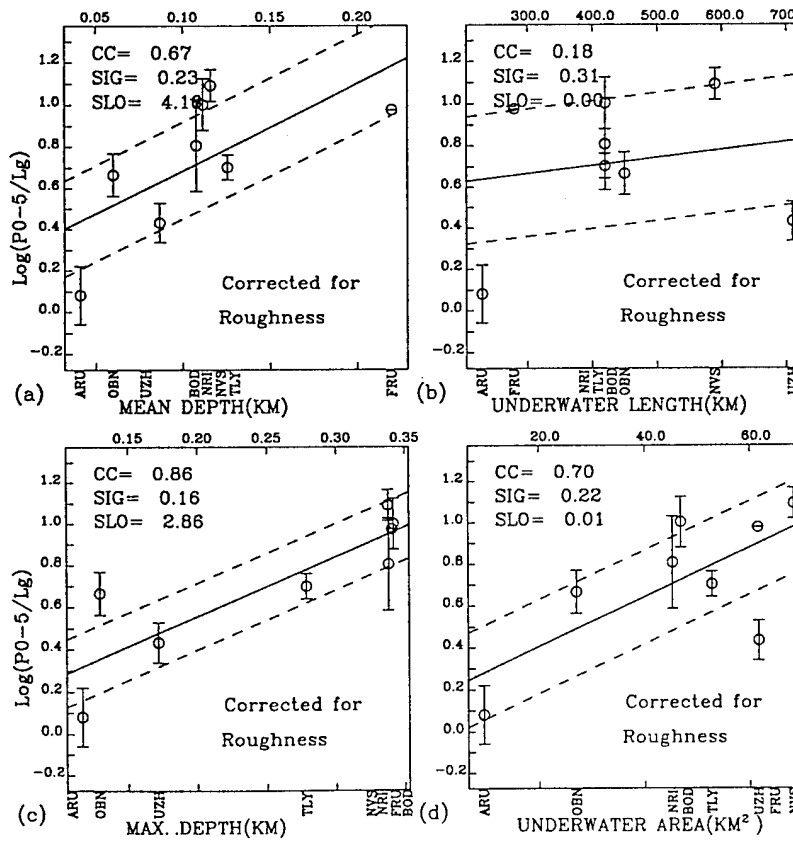


Figure 15. Similar to Figure 14, but now the P/L_g ratios have been corrected for relative path roughness, using the continental path correlations found for Semipalatinsk data by Zhang and Lay (1994).

properties, with the best correlation again being with maximum depth. Similar results are found for the 0- to 50-sec P -wave window. While these data are at larger distances than conventionally used in regional discrimination efforts (based on Pn/L_g), these results hold much promise for comparable efforts to reduce scatter in discriminant ratios used for nonproliferation monitoring.

Discussion and Conclusions

This study indicates that L_g energy is lost when traversing an underwater continental margin, possibly accompanied by a corresponding increase in S_n energy. Studies by Isacks and Stephens (1975), Chinn *et al.* (1980), and Ni and Barazangi (1983) have discussed so-called "early L_g " phases in the S_n coda, which arrive several seconds ahead of the 3.5 km/sec group velocity arrival time. Baumgardt (1990) also observed early L_g in his study of data at NORESS and Graefenburg arrays for Novaya Zemlya sources. He argues that the primary mechanism for energy partitioning is L_g -to- S_n and S_n -to- L_g scattering. Our study emphasizes the important role played by the underwater path, and we agree that L_g -to- S_n and S_n -to- L_g scattering probably plays some role in the propagation. This could explain the enhanced S_n/L_g ratios of the Novaya Zemlya observations relative to Semipalatinsk data. However, it is important to note that the trends in S_n/L_g and P/L_g ratios versus bathymetric parameters in Figures 13 and 15 may be primarily an L_g effect. Moreover, it is not possible for us to confidently isolate the location of any conversions that do take place, other than to say that it must be in the general vicinity of the source or receivers, given our gross group velocity windowing procedure.

The Barents Sea and Kara Sea are similar shallow basins. Gramberg (1988) identifies two defining characteristics of the central Barents basin. One is thinning of the crust by about 10 km (Fig. 16b). Another is the "missing granitic layer." The data that Baumgardt (1990) analyzes traverse the central Barents Sea, where significant crustal thinning is expected. In our data set the three paths sampling the Barents Sea cross the Pechora plate, in the southeast region of the basin, where the crustal thickness is about 35 km. Bogolepov *et al.* (1990) studied the structure of the Kara Sea basin with a combination of magnetic, gravitational, and seismic refraction data. They find similar characteristics in the center of south Kara syncline (Fig. 16c) to the central Barents Sea. The depth of the Moho varies from 32 to 35 km in the near-shore region to 26 to 28 km in the central Kara syncline. The depth of the Conrad discontinuity varies from 30 to 22 to 25 km. In the central region, the crystalline granitic complex is replaced by a gabbroic complex. Another characteristic is the complex geometry of the granitic basement, with extensive folding, metamorphism and imbricate structure. Four of our paths, to

BOD, NRI, TLY, and NVS cross the central Kara Sea basin, while the last two, to FRU and ARU, traverse the Ural–Novaya Zemlya fold belt. We observe significant reductions in L_g amplitudes for the paths across the Kara Sea.

The L_g phase can be viewed as a guided wave in the crust, very dependent upon the lateral continuity of the wave guide. Given that disruptions of the wave guide are expected near continental margins, and even within tectonically active continental regions, there are many concerns about the reliability of L_g in discrimination measurements (e.g., Kennett, 1989), independent of its remarkable relative stability on a given path for relative yield estimation (e.g., Ringdal *et al.*, 1992; Hansen *et al.*, 1990). Crustal thinning apparently can reduce L_g

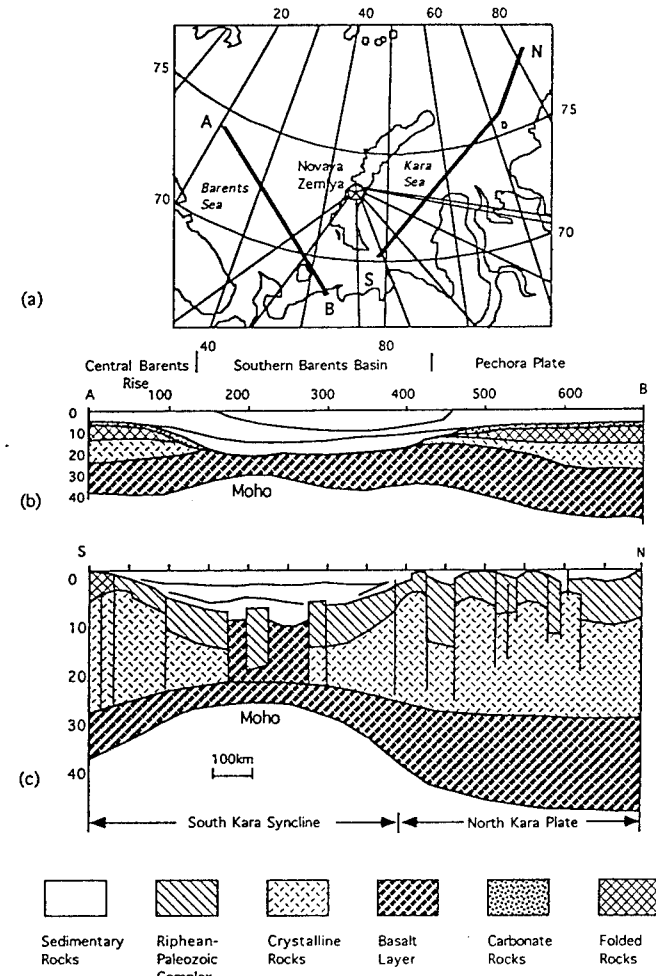


Figure 16. (a) Map of the adjacent region of the islands of Novaya Zemlya, showing two lines of cross section and eight paths. (b) NW-SE cross section, labeled A-B in (a), across the southeast part of the Barents Sea basin (after Gramberg, 1988). (c) NE-SW cross section of the Kara Sea basin (after Bogolepov *et al.*, 1990), labeled N-S in (a), across the North Kara plate and south Kara syncline.

amplitude (Cao and Muirhead, 1993). Thus, we may explain the systematic trends between the Barents group and Kara group as a result of variable degree of blockage associated with thinning of the crustal wave guide. However, the precise mechanisms involved are subject to debate.

It is quite possible that sediment thickness variations in the basins influence L_g blockage, but we do not have a robust procedure for separating the effects of crustal thinning and sediment thickness, which are strongly correlated. Maximum water depth, the parameter yielding the strongest relationships with L_g amplitudes, is strongly affected by near-surface geology, such as the sediment thickness in the basins. Some information is available about the thickness of sedimentary basins, along with Moho depth along the paths sampled by our data, mainly from Deep Seismic Sounding and seismic reflection profiling as well as other geological and geophysical data (Kunin and Sheykh-Zade, 1983; Kunin, 1986). This information has been digitized and made available by the Cornell Institute for Studies of the Continents, with 0.25° resolution. Figure 17 shows the relationships between L_g amplitudes, corrected for geometric spreading, and maximum water depth (Fig. 17a), minimum crustal thickness (Fig. 17b), and maximum sedimentary layer thickness (Fig. 17c) along each path. While the data set is limited, the strongest variation is found with water depth, and no

trend is apparent with minimum crustal thickness, which basically measures the necking of the crust along the continental margin. However, the latter parameter is not well sampled by our particular data set. For other data sets (Zhang, Schwartz, and Lay, 1994), crustal necking does appear to strongly affect L_g amplitudes. Sediment layer thickness is associated with a weak trend, but the statistical significance is low. The precise mechanism by which the L_g energy is lost requires further study. The complex structure of the crystalline basement may account for some of the observed behavior, such as the low amplitudes of both L_g and S_n along the path to TLY (Fig. 11).

The foregoing discussion has emphasized the possible elastic scattering effects of the disrupted wave guide. There is no question that attenuation is very important for L_g and S_n phases as well, and it would be very attractive to correct our data for attenuation variations on the different paths. Many efforts have evaluated frequency-dependent attenuation of L_g in western Europe (e.g., Nicolas *et al.*, 1982; Campillo *et al.*, 1985; Campillo, 1987) and Eurasia (Nuttli, 1980, 1981; Chun *et al.*, 1992). Analysis of L_g coda also provides constraints on the L_g quality factor (e.g., Xie and Mitchell, 1990, 1991; Pan *et al.*, 1992; Mitchell *et al.*, 1993). The L_g coda Q values agree well with L_g Q values in some cases (Mitchell *et al.*, 1993). We use the Eurasian L_g coda Q

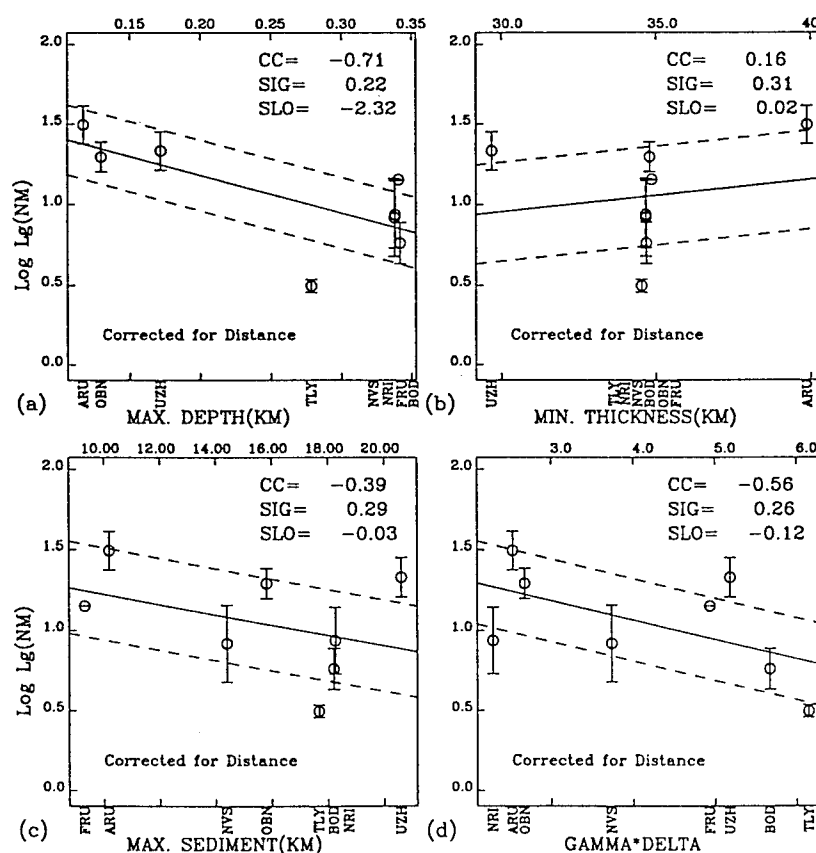


Figure 17. The relationships between L_g amplitudes, corrected for geometric spreading, and (a) maximum water depth, (b) minimum crustal thickness, (c) maximum sedimentary layer thickness, and (d) the attenuation term $\gamma\Delta$ along each path.

map of Pan *et al.* (1992) to determine the exponential attenuation term $\gamma\Delta$ (Nuttli, 1986) for a frequency of 1 Hz for each of our paths (Fig. 17d). There is a clear correlation with $\log L_g$, as expected, but the trend is quite a bit weaker than expected (the expected slope is $-\log(e) = -0.43$). If we apply the attenuation corrections, using the simplifying approximation that our rms values are representative of the 1-Hz amplitudes, the L_g amplitudes no longer show any trend with bathymetric properties. However, our feeling is that the Q model has the right geographic pattern, but it overpredicts attenuation variations on the different paths, when applied to L_g directly, as suggested by the low slope seen in Figure 17d. Thus, we have not used corrected L_g amplitudes in our attempt to detect underwater path effects. We found that S_n amplitudes show a strong trend with the L_g coda Q variations for Novaya Zemlya, but the S_n/L_g ratios do not vary with $\gamma\Delta$ for either test site, so it is not likely that attenuation plays a key role in the strong patterns seen in Figure 8. It is not clear how to correct the S_n data for attenuation, but there is a clear suggestion that S_n attenuation is linked to the L_g coda Q variations. This suggests coupling of upper mantle and crustal attenuation, and raises the possibility that the L_g coda Q model may include a mantle component that overcorrects the L_g phases. Until we have independent models for S_n attenuation we cannot proceed further, but it is clear that attenuation is an important factor influencing the regional phase-amplitude ratios, and significant progress is being made in mapping out the attenuation variations (Pan *et al.*, 1992).

Since we generally lack detailed knowledge of crustal structure for paths traversed by regional phases used in nonproliferation monitoring, we have explored the possibility of developing empirical path calibration procedures. Water depth proved to be the most effective elastic path characteristic for the Novaya Zemlya data set, presumably since it serves as a surrogate for the deep structure of the shallow sea basin. Relative to the reference data set provided by Semipalatinsk recordings, almost all Novaya Zemlya data exhibit a shift of the peak energy toward the S_n window, whether the maximum water depth is 100 or 300 m. This indicates that an amplitude correction is generally needed for wave paths that cross marginal seas. In addition, 200-m water-depth differences can reflect variations in crustal thickness and sediment thickness, causing L_g amplitudes to vary. Using empirical corrections should enable significant reduction in the scatter of both S_n/L_g and P/L_g amplitude ratios. Combined with empirical corrections for topography along the on-land paths and corrections for laterally varying attenuation models in the crust and upper mantle, reduced scatter in such measurements may improve nonproliferation monitoring efforts in diverse crustal environments.

Acknowledgments

The waveform data set used here was made available by Dr. Alan Ryall. We thank Dr. Hans Israelsson for extensive information about the instrument responses, and Dr. Susan Schwartz for helping to resolve some problems with the data. Dr. Douglas Baumgardt and an anonymous reviewer provided helpful comments on the manuscript. Dr. Xie and Dr. Pan kindly allowed us to use their L_g coda Q model. This research was supported by the W. M. Keck Foundation, the Air Force Office of Scientific Research, under Grant Number F49620-92-J-0461, and the Defense Advanced Research Projects Agency, under Contract Number F29601-91-K-DB21. This is contribution number 212 of the Institute of Tectonics and the C. F. Richter Seismological Laboratory.

References

- Baumgardt, D. R. (1990). Investigation of teleseismic L_g blockage and scattering using regional arrays, *Bull. Seism. Soc. Am.* **80**, 2261–2281.
- Bogolepov, A. K., V. A. Zhuravlev, E. U. Shipilov, and A. Y. Yudin (1990). New data on the deep structure of the Kara Sea (from results of complex geological and geophysical study), *Dokl. Akad. Nauk SSSR* **315**, 159–162 (in Russian).
- Campillo, M., J. L. Plantet, and M. Bouchon (1985). Frequency-dependent attenuation in the crust beneath central France from L_g waves: data analysis and numerical modeling, *Bull. Seism. Soc. Am.* **75**, 1395–1411.
- Campillo, M. (1987). L_g wave propagation in a laterally varying crust and the distribution of the apparent quality factor in central France, *J. Geophys. Res.* **92**, 12604–12614.
- Cao, S. and K. J. Muirhead (1993). Finite difference modeling of L_g blockage, *Geophys. J. Int.* **116**, 85–96.
- Chinn, D. S., B. L. Isacks, and M. Barazangi (1980). High-frequency seismic wave propagation in western South America along the continental margin, in the Nazca Plate and across the Altiplano, *Geophys. J. R. Astr. Soc.* **60**, 329–344.
- Chun, K.-Y., T. F. Zhu, and X. R. Shih (1992). Time domain analysis of L_g wave attenuation in Eurasia, in *Regional Wave Attenuation in Eurasia, Scientific Report No. 2, DARPA/NMRO, Arlington, Virginia*, 3–12.
- Gramberg, I. S. (1988). The Barents Shelf Plate, Vol. 196, *Nedra, Leningrad, USSR*, 218, (in Russian).
- Gregersen, S. (1984). L_g wave propagation and crustal structure differences near Denmark and the North Sea, *Geophys. J. R. Astr. Soc.* **79**, 217–234.
- Hansen, R. A., F. Ringdal, and P. G. Richards (1990). The stability of RMS L_g measurements and their potential for accurate estimation of the yields of Soviet underground nuclear explosions, *Bull. Seism. Soc. Am.* **80**, 2106–2126.
- Isacks, B. L. and C. Stephens (1975). Conversion of S_n to L_g at a continental margin, *Bull. Seism. Soc. Am.* **65**, 224–235.
- Israelsson, H. (1992). RMS L_g as a yield estimation in Eurasia, Final Technical Report for AF Phillips Laboratory, Hanscom AFB, Massachusetts.
- Kadinsky-Cade, K., M. Barazangi, J. Oliver, and B. Isacks (1981). Lateral variations of high-frequency seismic wave propagation at regional distances across the Turkish and Iranian Plateaus, *J. Geophys. Res.* **86**, 9377–9396.
- Kennett, B. L. N. (1986). L_g waves and structural boundaries, *Bull. Seism. Soc. Am.* **76**, 1133–1141.
- Kennett, B. L. N. (1989). On the nature of regional seismic phases—I, phase representations for P_n , P_g , S_n , L_g , *Geophys. J. Int.* **98**, 447–456.
- Kennett, B. L. N. and S. Mykkeltveit (1984). Guided wave propa-

gation in laterally varying media—II, L_s -waves in north-western Europe, *Geophys. J. R. Astr. Soc.* **79**, 257–267.

Kennett, B. L. N., S. Gregersen, S. Mykkeltveit, and R. Newmark (1985). Mapping of crustal heterogeneity in the North Sea basin via the propagation of L_s -waves, *Geophys. J. R. Astr. Soc.* **83**, 299–306.

Kunin, N. Ya. and E. R. Sheykh-Zade (1983). New data on lateral inhomogeneities in the upper mantle under western Eurasia, *Dokl. Akad. Nauk. USSR.* **273**, 1087–1091.

Kunin, N. Ya. (1986). The basic morphostructures on the surface of the upper mantle under the Asiatic continent, *Izv. Akad. Nauk USSR. Earth Phys.* **22**, 349–357.

Lynnes, C. and R. Baumstark (1991). Phase and spectral ratio discrimination in North America, Final Technical Report, PL-TR-91-2212(II) Phillips Laboratory, Hanscom, AFB, Massachusetts.

Maupin, V. (1989). Numerical modeling of L_s wave propagation across the North Sea central graben, *Geophys. J. Int.* **99**, 273–283.

Mitchell, B. J., J. Xie, Y. Pan, and J. Ni (1993). L_s Q , L_s coda Q and yield estimation in Eurasia, in *Proc. of the 15th Annual PL/arpa Seismic Research Symposium*, Phillips Laboratory, Hanscom AFB, Massachusetts, 277–283.

Ni, J. and M. Barazangi (1983). High-frequency seismic wave propagation beneath the Indian Shield, Himalayan Arc, Tibetan Plateau and surrounding regions: high uppermost mantle velocities and efficient S_n propagation beneath Tibet, *Geophys. J. R. Astr. Soc.* **72**, 665–689.

Nicolas, O. W., B. Mechler, and M. Bouchon (1982). Attenuation of regional phases in western Europe, *Bull. Seism. Soc. Am.* **72**, 2089–2106.

Nuttli, O. W. (1973). Seismic wave attenuation and magnitude relations for eastern North America, *J. Geo Phys. Res.* **78**, 876–885.

Nuttli, O. W. (1980). The excitation and attenuation of seismic crustal phases in Iran, *Bull. Seism. Soc. Am.* **70**, 469–485.

Nuttli, O. W. (1981). On the attenuation of L_s waves in western and central Asia and their use as a discriminant between earthquakes and explosions, *Bull. Seism. Soc. Am.* **71**, 249–261.

Nuttli, O. W. (1986). Yield estimates of Nevada test site explosions obtained from seismic L_s waves, *J. Geophys. Res.* **91**, 2137–2151.

Nuttli, O. W. (1988). L_s magnitudes and yield estimates for underground Novaya Zemlya explosions, *Bull. Seism. Soc. Am.* **78**, 873–884.

Oliver, J., M. Ewing, and F. Press (1955). Crustal structure of the Arctic regions from the L_s phase, *Bull. Geolo. Soc. Am.* **66**, 1063–1074.

Pan, Y., B. J. Mitchell, J. Xie, and J. Ni (1992). L_s coda Q across northern Eurasia, in *Proc. of the 14th Annual PL/Darpa Seismic Research Symposium*, PL-TR-92-2210, Phillips Laboratory, Hanscom AFB, Massachusetts, 311–317.

Pomeroy, P. W., W. J. Best, and T. J. McEvilly (1982). Test ban treaty verification with regional data—a review, *Bull. Seism. Soc. Am.* **72**, S89–S129.

Press, F. and M. Ewing (1952). Two slow surface waves across North America, *Bull. Seism. Soc. Am.* **42**, 219–228.

Regan, J. and D. G. Harkrider (1989). Seismic representation theorem coupling: synthetic SH mode sum seismograms for non-homogeneous paths, *Geophys. J. R. Astr. Soc.* **98**, 429–446.

Ringdal, F. and J. Fyen (1991). RMS L_s analysis of Novaya Zemlya explosion recordings, Semiannual Technical Summary, 1 October 1990–31 March 1991, *NORSAR Scientific Report No. 2-90/91*. NTNF/NORSAR, Kjeller, Norway.

Ringdal, F., P. D. Marshall, and R. W. Alewine (1992). Seismic yield determination of Soviet underground nuclear explosions at the Shagan River test site, *Geophys. J. Int.* **109**, 65–77.

Ruzaikin, A. I., I. L. Nersesov, V. I. Khalturin, and P. Molnar (1977). Propagation of L_s and lateral variations in crustal structure in Asia, *J. Geophys. Res.* **82**, 307–316.

Savarensky, E. and N. Valdner (1960). Observations of L_s and R_s waves from the Black Sea basin earthquakes, *Ann. Geofis.* **13**, 129–134.

Wessel, P. and W. H. F. Smith (1991). Free software helps map and display data, display, *EOS* **72**, 441, 445–446.

Wetmiller, R. J. (1974). Crustal structure of Baffin Bay from earthquake generated L_s phases, *Can. J. Earth Sci.* **11**, 123–130.

Xie, J. and B. J. Mitchell (1990). A back-projection method for imaging large-scale lateral variations of L_s and coda Q with application to continental Africa, *Geophys. J. Int.* **100**, 161–181.

Xie, J. and B. J. Mitchell (1991). L_s coda Q across Eurasia, in *Yield and Discrimination Studies in Stable Continental Regions*, Technical Report PL-TR-91-2286. ADA 251590.

Zhang, T. and T. Lay (1994). Analysis of short-period regional phase path effects associated with topography in Eurasia, *Bull. Seism. Soc. Am.* **84**, 119–132.

Zhang, T., S. Y. Schwartz, and T. Lay (1994). Multivariate analysis of waveguide effects on short-period regional wave propagation in Eurasia and its application in seismic discrimination, *J. Geophys. Res.* (submitted for publication).

University of California
Santa Cruz, California 95064

Manuscript received 28 June 1993.

Multivariate analysis of waveguide effects on short-period regional wave propagation in Eurasia and its application in seismic discrimination

Tian-Run Zhang, Susan Y. Schwartz, and Thorne Lay

Institute of Tectonics, University of California, Santa Cruz

Abstract. Four data sets characterizing gross crustal waveguide configuration and attenuation properties in Eurasia (surface topography, Moho depth, sediment thickness, and L_g coda Q value) are used to examine path influences on short-period regional P/L_g ratios. Linear regressions show considerable correlations between $\log P/L_g$ and waveguide properties for both earthquake and explosion data. This is of interest because P/L_g ratios are considered to be promising regional discriminants for which it is desirable to reduce scatter caused by propagation effects. To develop a comprehensive and stable model describing the path effects, multivariate regression is applied to the data set. The waveguide properties considered are highly correlated with each other, causing collinearity in the regression process. After backward elimination, we obtain a final model with statistically significant regression coefficients, which involves two independent variables: the path attenuation term $\gamma\Delta$ and maximum sediment thickness on each path. These two factors are associated with (1) the overall intrinsic and scattering attenuation in the waveguide and (2) the localized blockage effects caused by waveguide geometry, respectively. Using the final model to correct the observed P/L_g measurements reduces the variances for separate earthquake data and explosion data by 40% and 27%, respectively. This correction slightly enhances the performance of the discriminant for periods near 1 s.

Introduction

The manner in which regional P_n , P_g , S_n , and L_g phases are affected by passing through different geological structures is not clearly established in terms of the geometrical characteristics and internal properties of the crust. Since L_g is a guided wave in the crustal waveguide, lateral variations of the waveguide structure should affect its propagation. Either thinning or thickening of the waveguide should result in a portion of the L_g mode energy leaking out, as illustrated using ray diagrams by *Kennett* [1986]. However, it has been hard to verify this qualitative inference with numerical simulations. *Campillo* [1987] compared synthetic seismograms computed in crustal models with variations of Moho depth and sediment thickness with those computed in a flat-layered model. He found that the wave shapes are sensitive to the presence of the irregularities but the overall amplitude decay was not. *Maupin* [1989] performed numerical modeling of L_g propagation in a simplified model of the North Sea graben. This model did not predict the severe L_g attenuation observed in this area. On the contrary, the synthesized L_g wave train appears surprisingly robust when crossing a zone where its waveguide is strongly deformed. *Regan and Har krider* [1989] simulated the extreme cases of transitions from continent to ocean crust and vice versa, for

transverse-component L_g propagation. In this case, the L_g amplitude did decrease, but the attenuation is not sufficient to explain observed values. The strongest attenuation predicted involves a reduction of a factor of 2-3 in amplitude. However, it is well known that L_g is totally eliminated when traversing oceanic crust [Press and Ewing, 1952]. Thus other factors and/or more complex structures must be considered to explain the observed attenuation of L_g . Recently, *Cao and Muirhead* [1993] successfully modeled L_g blockage with a P - SV finite difference method after introducing a water layer above the free surface. The water layer strongly attenuates R_g , the short-period fundamental mode Rayleigh wave, but has less effect on L_g . However, interpretation of the influence of variable waveguide structure without water-covered segments is still open.

The most important factor with predictable effect on L_g other than the waveguide structure is the quality factor Q , accounting for both intrinsic attenuation and scattering losses. Many investigations of Q using the decay of L_g amplitude with epicentral distance have been conducted in western Europe [e.g., *Nicolas et al.*, 1982; *Campillo et al.*, 1985] and Eurasia [e.g., *Nuttli*, 1980, 1981; *Chun et al.*, 1992]. Another way to evaluate waveguide Q is from frequency dependent decay of L_g coda [e.g., *Xie and Mitchell*, 1990; *Pan et al.*, 1992; *Mitchell et al.*, 1993]. The Q obtained in this way is called L_g coda Q . L_g Q values sometimes agree well with L_g coda Q values in the same region [*Mitchell and Hwang*, 1987; *Mitchell et al.*, 1993]. However, they may have significantly different values in some regions [*Campillo*, 1990]. Both geometrical blockage and

waveguide attenuation affect L_g , but it is difficult to clearly separate these effects observationally. Indeed, distortions of the waveguide are likely to be associated with tectonic factors influencing intrinsic attenuation, so the effects may often be coupled.

It is desirable to quantitatively identify the respective roles played by large-scale structural heterogeneities and by the attenuation properties of the crust, but at present, doing this requires empirical approaches. Because of the lack of information about the lower crust and upper mantle, *Zhang and Lay* [1994a] first used surface topography as a manifestation of the varying crustal structure. They found a surprisingly strong correlation between S_n/L_g ratios for Eurasian explosions and roughness or mean altitude of the topography along the path to each station. *Zhang and Lay* [1994b] found that the maximum water depth along each path correlates with the L_g and S_n amplitudes for signals traversing the Kara and Barents Seas. *Jih* [1993] has demonstrated strong scattering of R_g phases by surface topography which explains why R_g seldom propagates to large distances. R_g to L_g scattering may produce some correlation between L_g behavior and surface topography characteristics.

Topography only indirectly reflects the properties of the crust; to further explore the nature of regional seismic wave propagation in crustal waveguides in this paper, we use four data sets that grossly characterize the crustal structure and attenuation properties: surface topography, Moho depth, sediment thickness, and L_g coda Q values. Although each characterization of the crust has limited resolution, complete representations are available for Eurasia. We seek a model to define the relative importance of various waveguide characteristics for regional phases using P/L_g amplitude ratios for earthquake and explosion recordings in Eurasia. Only a few such data have overlapping paths in Eurasia, so we treat large populations of paths rather than focusing on a single region. Not surprisingly, many factors appear to influence the data, so multivariate analysis is used to assess their importance and correlation. For example, in a study of regional wave propagation in northern Eurasia, weak L_g amplitude is related to thinner crust [*Zhang and Lay*, 1994b]. However, in the Tibetan Plateau, where the L_g amplitudes are also weak, the crust is the thickest in the world. If the low crustal Q in the Tibetan Plateau is accounted for, the low L_g amplitudes can be explained. A multivariate description is thus needed to predict regional phase effects. A first generation model is obtained here.

P/L_g amplitude or spectral ratios are the most promising regional distance seismic discriminants. However, strong path effects on the ratios have so far restricted their use to nearly common propagation paths [*Baumgardt and Young*, 1990; *Bennett et al.*, 1992]. Reduction in P/L_g variance by correcting this ratio for empirically derived propagation effects may remove the restriction of common paths for explosion and earthquake data. This would greatly enhance the possibility of discrimination in the context of nonproliferation monitoring, where no prior explosion population may be available. This provides further motivation for the empirical approach of this paper.

Data

Our explosion data are recordings from Soviet-run stations that were collected and digitized as part of a data exchange associated with the Joint Verification Experiment. We use 211 recordings of 77 underground nuclear tests located in the Semipalatinsk test site, a subset of the data used by *Zhang and Lay* [1994a] after exclusion of the data lacking P or L_g . Seventy-two recordings of 20 underground nuclear tests located in the Novaya Zemlya test site near Matochkin Shar are extracted from the data used by *Zhang and Lay* [1994b]. The earthquake data set consists of 34 digital waveforms for 17 events between 1988 and 1992 recorded at IRIS/IDA (Incorporated Research Institutions for Seismology/International Deployment of Accelerometers), CDSN (Chinese Digital Seismograph Networks) and ASRO (Abbreviated Seismic Research Observatory) stations in Eurasia. Almost all of the explosion data are in the distance range 14° to 36° , while the earthquake data range from 4° to 35° . The explosion data are short-period, while the earthquake data are mostly broadband. For all data, the instrument responses are equalized to the 1988 response of the CKM-3 seismometer at station OBN, and waveforms are bandpass filtered from 0.6 to 3.0 Hz (following the procedure of *Israelsson* [1992]). RMS P wave amplitudes are measured for a 0-50 s time window (following *Bennett et al.* [1992]), and RMS L_g amplitudes are calculated for a 3.7-3.1 km/s group velocity window [*Israelsson*, 1992]. A noise correction is applied to each RMS measurement [*Zhang and Lay*, 1994a]. We average the $\log P/L_g$ ratio values of the explosion data along each path, yielding 16 path-averaged explosion $\log P/L_g$ values.

The surface topography data are from the 5 arc min interval ETOPO5 data set compiled by the National Geophysical Data Center, Boulder, Colorado. Figure 1 shows our explosion data path coverage superimposed on the topography of northern Eurasia. The earthquake data path coverage is shown in Figure 2 superimposed on the crustal thickness information. Unfortunately, the explosion and earthquake data do not sample the same region. The Moho depth (Figure 2) and sediment thickness (Figure 3) information were compiled by *Kunin and Sheyk-Zade* [1983], and *Kunin* [1987] from a large number of deep seismic sounding (DSS) profiles and other data. The compiled crustal parameters were digitized and gridded at Cornell University using a 1/4 degree interval [*Fielding et al.*, 1992]. The accuracy of these maps is difficult to assess, but at least they provide a guide as to gross crustal structure.

L_g coda Q values across Eurasia (Figure 4) were computed by tomographic inversion of explosion and earthquake data by *Pan et al.* [1992]. We use this model as a guide to gross attenuative properties of the crust, recognizing that some effects of waveguide irregularity may be folded into the Q values.

For each path from source to receiver, great circle variations of each of the four crustal properties are analyzed. Examples of variations in these profiles along three different paths from an earthquake (September 17, 1989) in the middle of the Caspian Sea to stations OBN, ARU, and ANTO are shown in Figure 5. Topography,

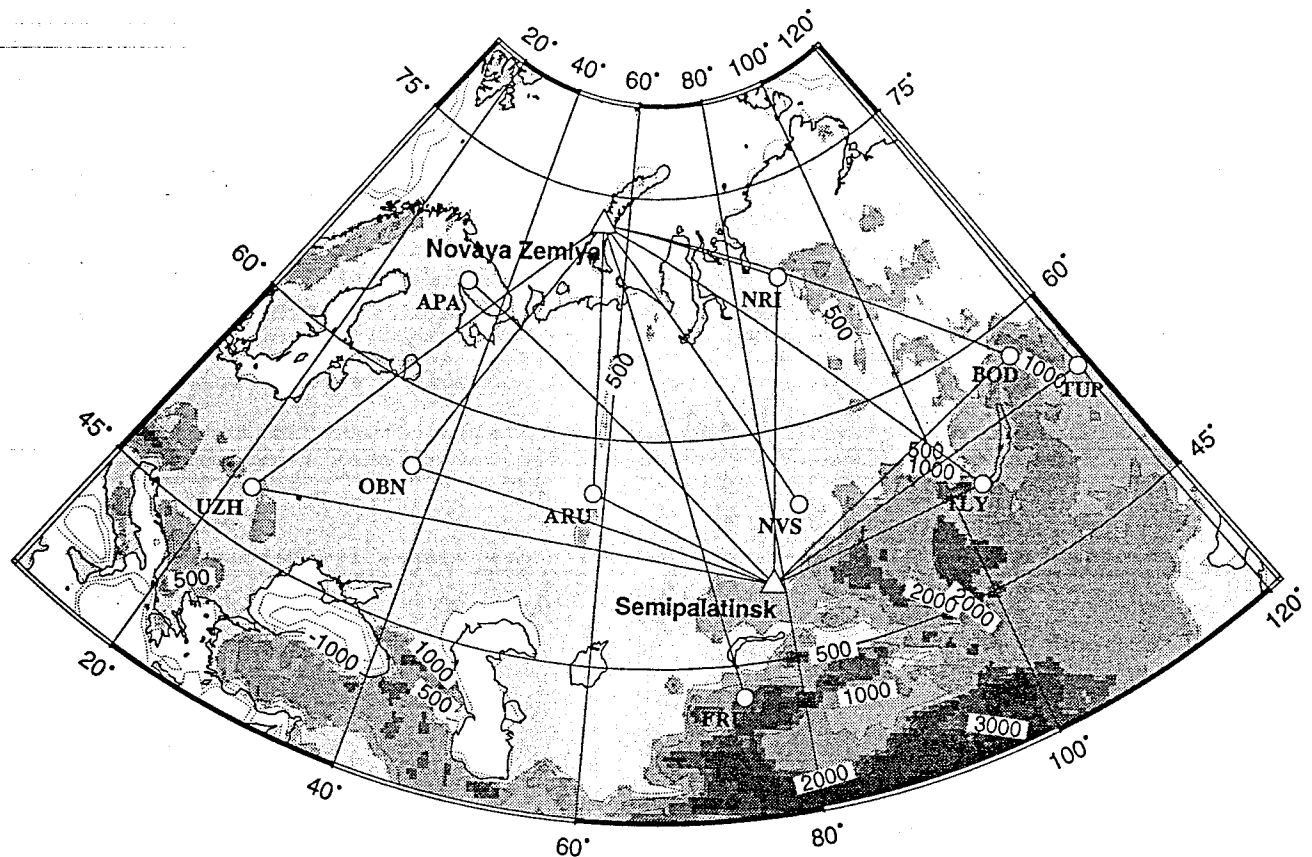


Figure 1. Map showing the locations of the former Soviet Union test sites at Novaya Zemlya and Semipalatinsk, marked with triangles, and the seismological stations, marked with circles and indicated by their codes. The lines between the triangles and the circles correspond to great circle paths. Topography is indicated with contour intervals every 1000 m from -2000 to 3000 m above sea level. In order to outline the Ural Mountains and other low plateaus, 500-m contours are also shown. Map software is from *Wessel and Smith* [1991].

Moho depth, and sediment thickness are drawn together on profiles with a 10-km lateral sampling interval for each path (Figure 5a). The L_g coda Q profiles are shown in Figure 5b with a 100-km lateral sampling interval. Since deterministic modeling of regional phases along these complex waveguides is not currently viable, we parameterize the path properties and attempt to relate summary parameters to the observed wave field characteristics, as manifested in the logarithmic ratios of RMS P /RMS L_g .

Linear Regression of Waveguide Parameters

We first explore the individual correlations between waveguide parameters and observed P/L_g amplitude ratios for our explosion and earthquake data sets. The results for earthquake data are summarized in Figures 6 and 7. Those for Novaya Zemlya explosion data are in Figures 8 and 9. Those for Semipalatinsk explosion data are in Figures 10 and 11.

Topography

Surface topography variations are small relative to crustal thickness but to some degree do reflect fluctuations in crustal thickness through isostasy. Topography is also affected by lateral variations in thermal structure of the crust and upper mantle. These considerations suggest that topography may influence regional phases both directly as a source of scattering and indirectly as a manifestation of waveguide structure and thermal variations. Surface topography is also widely available with high precision, so it is important to establish its influence, if any, on regional phases.

We examine the correlation of $\log P/L_g$ ratio along each source-receiver path with corresponding values of both minimum and mean altitude. The results for earthquakes (Figures 6a and 6b), and for explosions at Novaya Zemlya (Figures 8a and 8b), and Semipalatinsk (Figures 10a and 10b) all indicate similar trends with decreasing $\log P/L_g$ ratios as minimum or mean altitude increases. All correlations are statistically significant with the exception of mean altitude for the Novaya Zemlya data, which has the smallest range in mean altitude among the three data sets. Because of the smaller range in topography sampled by both explosion data sets compared with the earthquakes, the slope of the best fit line is most reliably determined by the earthquakes.

The results in Figure 6 are the first to indicate statistical topographic influence on regional phases from earth-

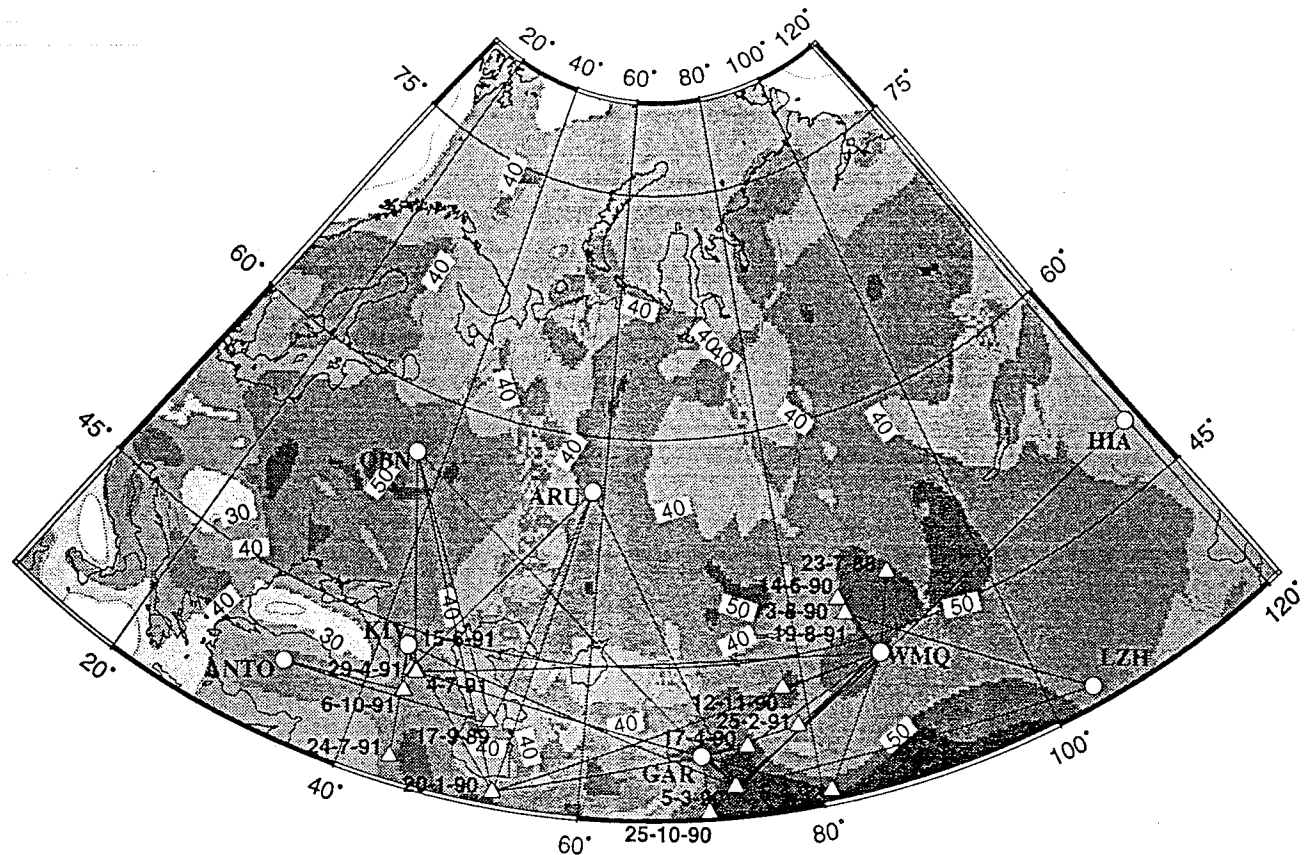


Figure 2. Map showing the locations of 17 earthquakes in Central Asia, the Caucasus, and the Middle East, marked with triangles, and the seismological stations used, marked with circles. Contours indicate variations in Moho depth, digitized at Cornell, from a Soviet map compiled by N. Kunin [Kunin and Sheykh-Zade, 1983; Fielding et al., 1992]. Moho topography is indicated with 10-km contour intervals.

quakes. This pattern is consistent with the previous results found by *Zhang and Lay* [1994b] using explosion data from Novaya Zemlya, although they measured the RMS P wave amplitude in a 0-5 s window rather than our 0-50 s window and they correlated this with maximum water depth rather than mean and minimum altitude. The observed trends are most reasonably attributed to L_g propagation, since much of the P wave energy at these distances dives into the upper mantle. *Zhang and Lay* [1994a] considered topographic influences on regional phases in the Semipalatinsk data, finding results like those in Figure 10b, although we include an additional station, ARU, here which does reduce the correlation. The earlier study limited the distance range used whereas here we include all observations. The *Zhang and Lay* [1994a] study reveals strong trends for S_n/L_g ratios versus mean altitude, as well as for measures of average roughness of the path. *Zhang and Lay* [1994b] indicated that the variability associated with the differences in underwater segments appears to overwhelm any effects of surface roughness for Novaya Zemlya data. In this study we find that the correlations of $\log P/L_g$ with the roughness of surface topography and variance of crustal thickness are also poor for the earthquake data (not shown). This is somewhat surprising as one might expect blockage effects to be controlled by variability of the crustal thickness. The reason will be

explored in future studies, along with alternate parameterizations of crustal characteristics.

Crustal Thickness

Crustal thickness is an important property of the crustal waveguide expected to profoundly affect propagation of regional waves. Thinning of the crust can strongly reduce L_g amplitude [Cao and Muirhead, 1993; *Zhang and Lay*, 1994b]. We correlate both minimum and mean crustal thickness with $\log P/L_g$ ratios to explore whether variations in L_g amplitude are due to average crustal structure or maximum thinning at restricted locations. The crust thins dramatically in several regions of our study area. In particular, the paths from Novaya Zemlya to Eurasian stations traverse the thin crust of the Barents and Kara Seas (Figure 1). The thinnest part of the crust below the Barents Sea occurs near 50°E, 70°N, where the thickness is less than 30 km. To the south, the great circle paths connecting earthquakes to stations cross four thin crustal regions, the southern, central, and northern Caspian Seas and the Aral Sea (Figure 2).

Correlations of $\log P/L_g$ with crustal thickness for earthquake data (Figures 6c and 6d), and for explosions from Novaya Zemlya (Figures 8c and 8d), and Semipalatinsk (Figures 10c and 10d) are generally stronger than those with topography, suggesting that direct measures of

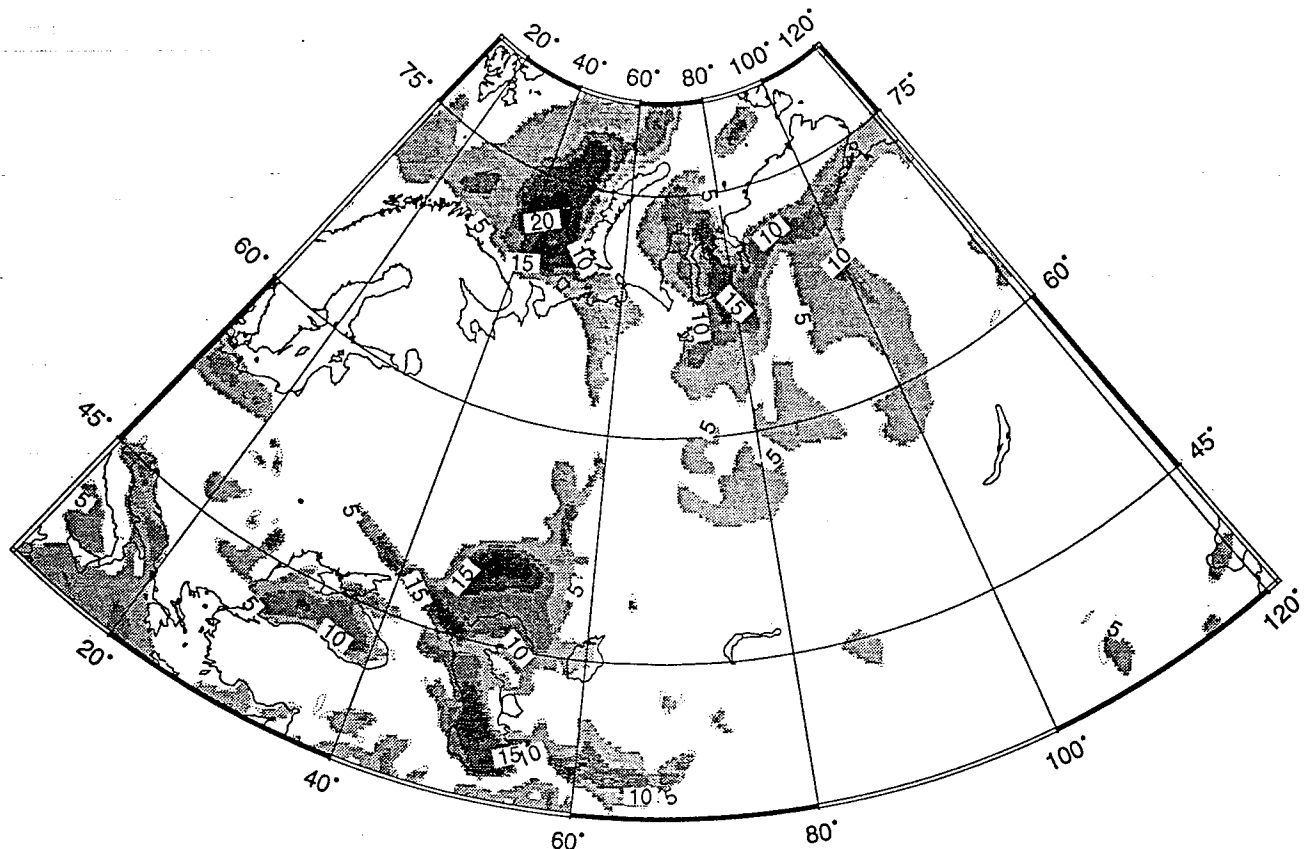


Figure 3. Map showing the sediment thickness, or basement depth variations of Eurasia. The data were digitized at Cornell from a Soviet map compiled by N. Kunin [Kunin, 1987; Fielding *et al.*, 1992]. The sediment depth is indicated with 5-km contour intervals.

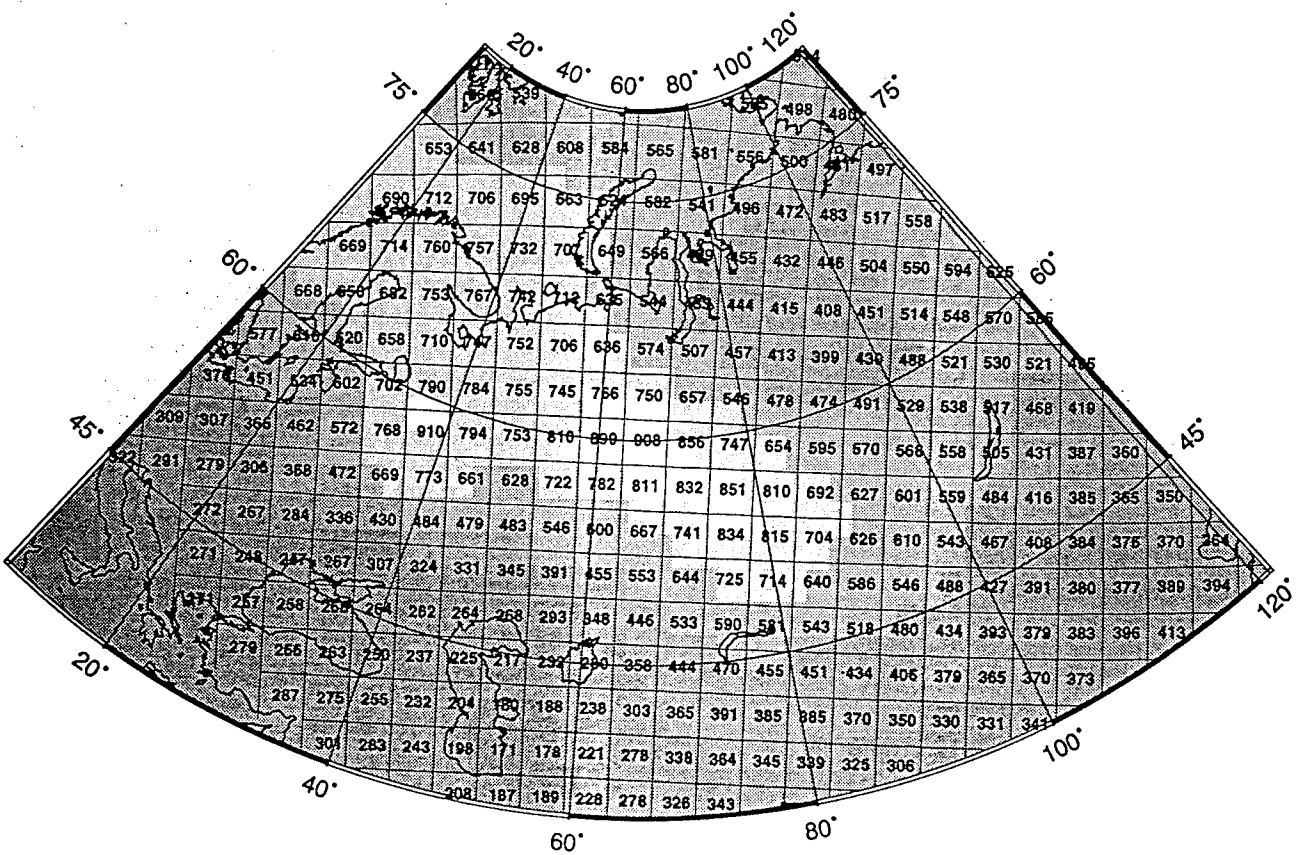


Figure 4. Map showing the L_g coda Q values of Eurasia at $f = 1$ Hz. These tomographic results are from *Pan et al.* [1992].

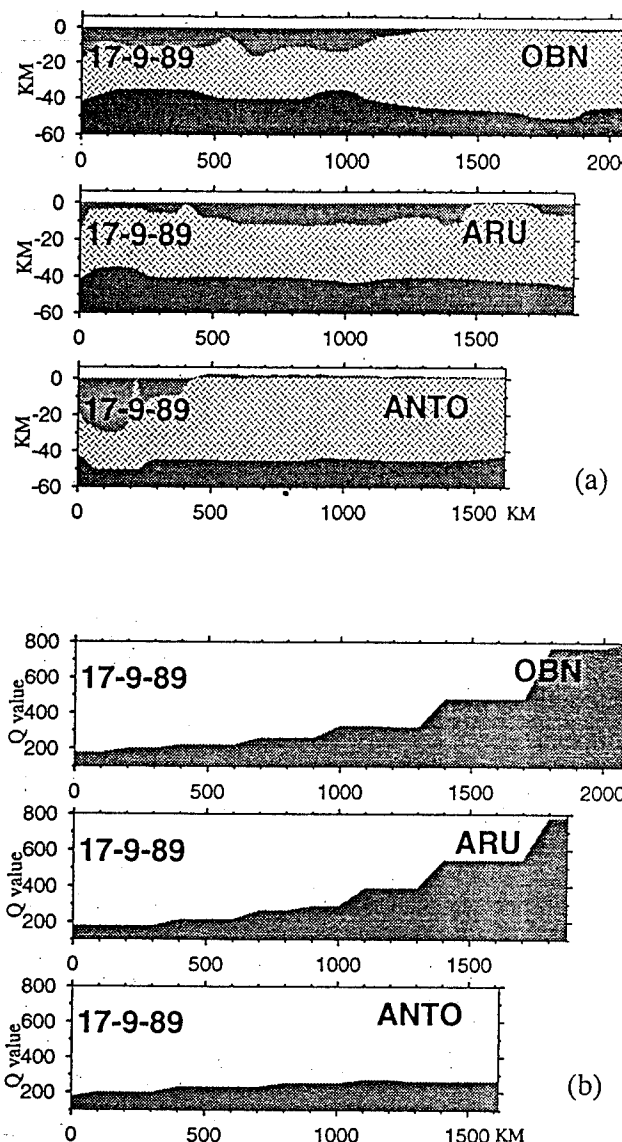


Figure 5. Examples of great circle characteristics of the path variables to three stations for event September 17, 1989, which occurred in the middle of the Caspian Sea. (a) The three curves in each panel indicate altitude, sediment depth, and Moho depth from top to bottom at a 10-km horizontal interval. (b) The curves indicate L_g coda Q values at a 100-km horizontal interval.

crustal thickness better reflect the nature of the waveguide than surface topography. The shortcoming of crustal thickness variables, however, is that their accuracy and reliability are not as good as for topography, especially in remote areas or beneath the seas.

Sediment Thickness

Sediment thickness variations are believed to have strong blockage effects on L_g and perhaps S_n propagation [Mitchell and Hwang, 1987; Baumgardt, 1990]. Our study area samples a few thick sedimentary basins (Figure 3), such as in the South Caspian depression (sediment thickness of 25-30 km) and South Barents depres-

sion (20-23 km). Such large sedimentary sections have not been identified in other continents or beneath the oceans [Kunin, 1987]. On the other hand, much of the remaining area in Eurasia has little to no sediment cover. Thus we might expect large variations in path effect. As for crustal thickness, the accuracy and reliability of sediment thickness data are not as good as for surface topography.

We find relatively strong correlations between $\log P/L_g$ ratios and along path sediment thickness for earthquake (Figures 7a and 7b) and explosion data (Figures 9a, 9b, 11a, and 11b). We evaluated both maximum and mean sediment thickness and both show comparable correlations. The slopes are consistent with reduced L_g amplitudes for thicker sediments along the path.

Attenuation

The L_g coda Q distributions for the northern and southern regions of the study area are quite different. High Q values are found in the north and much lower values in the south (see Figure 4). The lowest value is found south of the Caspian Sea. The regional differences make the attenuative properties for our three data sets very different. Without correction for variations in attenuation, it is unlikely that discrimination can be achieved in a region with a wide range of crustal Q .

Figures 7c, 7d, 9c, 9d, 11c, and 11d show correlations of $\log P/L_g$ ratio with minimum Q value and the path-integral $\gamma\Delta$ value. The definition of γ follows Nuttli [1986]:

$$\gamma(f) = \frac{\pi f}{UQ(f)},$$

where U is the group velocity, taken as 3.5 km/s, f is the wave frequency, taken as 1 Hz, and $Q(f) = Q_0 f^n$. We use the γ value at $f = 1$ Hz; thus the L_g coda Q at 1-Hz frequency given by Pan *et al.* [1992] is used directly. Δ is epicentral distance in kilometers.

The $\gamma\Delta$ value has a strong correlation with $\log P/L_g$ ratio for earthquake data, but the correlations are not as significant for explosion data. In part this may again be due to the reduced range of $\gamma\Delta$ sampled by the explosion paths. Semipalatinsk data cluster near $\gamma\Delta = 4$, which may preclude finding any correlation. The minimum Q variable (Figures 7c, 9c, and 11c) also has moderate correlations with $\log P/L_g$ ratios. Localized regions of strong attenuation may effectively reduce L_g amplitudes, but the earthquake data suggest that overall path attenuation has stronger correlation with $\log P/L_g$ ratios.

These linear regressions indicate that all four crustal characterizations are at least weakly correlated with the $\log P/L_g$ ratio. We would like to develop path corrections to reduce the variance in the measured ratios, as this may be key to effective discrimination. However, we need to consider which parameters to use in developing any path corrections. The four crustal factors considered have rather strong correlations amongst themselves. It is possible that a limited number of factors play the main role in the path effect, with others correlating with $\log P/L_g$ mathematically, but not physically.

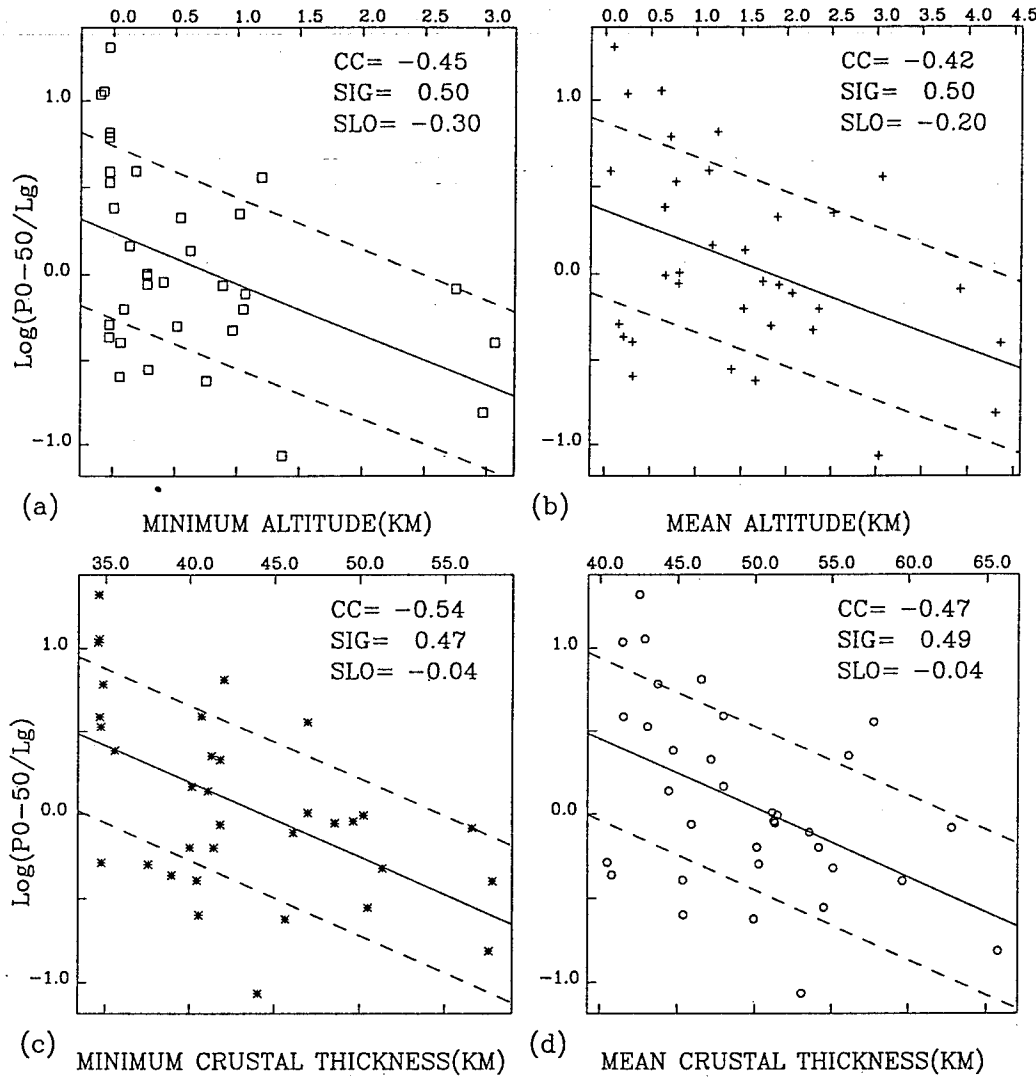


Figure 6. The $\log P/L_g$ ratio variations with (a) minimum and (b) mean altitude, and (c) minimum and (d) mean crustal thickness for earthquake data. CC stands for correlation coefficient, SIG is standard deviation of linear correlation, SLO is the slope of the linear regression. "P0-50" refers to RMS amplitude in 50-s window beginning with P onset.

In order to evaluate each factor, to obtain a reasonable and stable model for the overall path effect, we use multivariate regression.

Multivariate Analysis

We have shown that topography, crustal thickness, sediment thickness, and $\gamma\Delta$ computed from L_g coda Q and distance have correlations with $\log P/L_g$ ratios. A multivariate model is now developed for the relationship between the $\log P/L_g$ ratios and these factors. For topography and crustal thickness, we include both minimum and mean values for the purpose of identifying whether local properties or mean properties play a more important role.

Our goal is a unified model for both earthquake and nuclear test data. The $\log P/L_g$ ratios are systematically lower for earthquakes than for explosions, which is the basis of the $\log P/L_g$ discriminant. In order to combine

the data sets, we subtract an average value from each of the three data sets to emphasize the path effect. The explosion data involve 16 paths, and the earthquake data involve 34 paths. We regress the three data sets together with $n = 6$ explanatory variables and $m = 50$ observations, 16 of which are path averaged.

Table 1a lists the correlation matrix of $\log P/L_g$ ratios (Y) and six parameters that we choose to characterize the crust and Table 1b lists the result of multivariate regression. The definitions of the crustal parameters are $x(1)$, minimum altitude; $x(2)$, mean altitude; $x(3)$, minimum crustal thickness; $x(4)$, mean crustal thickness; $x(5)$, maximum sediment thickness; and $x(6)$, $\gamma\Delta$, the attenuation term.

Under the assumption that the $\log P/L_g$ ratios are a linear function of the six explanatory variables $x(1)$ to $x(6)$, we postulate the model

$$\vec{Y} = B_0 + \sum_{j=1}^6 B_j \vec{x}(j) + \vec{\epsilon}$$

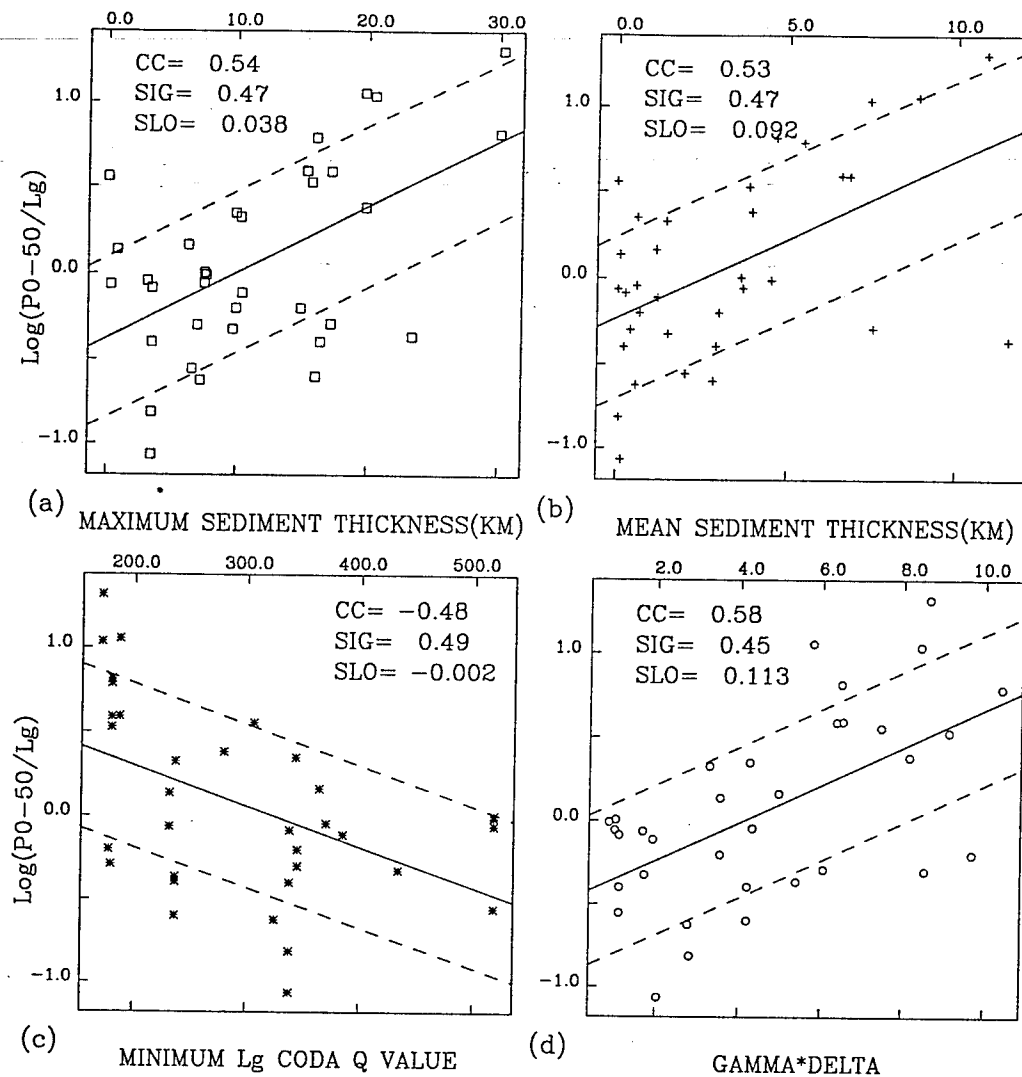


Figure 7. The $\log P/L_g$ ratio variations with (a) maximum and (b) mean sediment thickness, and (c) minimum Q value and (d) the attenuation term $\gamma\Delta$ for earthquake data.

where \vec{Y} , $\vec{x}(j)$, $j = 1, \dots, 6$, and \vec{e} are all vectors with 50 components. B_j , $j = 1, \dots, 6$ are the regression coefficients and B_0 is the intercept term. The random errors e_i , $i = 1, \dots, 50$ are assumed to be mutually independent and to follow a normal distribution with zero mean. In the following steps, we examined e_i and found they are in fact close to random variables with zero mean.

The correlation between minimum altitude and mean altitude, $x(1)$ and $x(2)$, is 0.939, and that between minimum and mean crustal thickness, $x(3)$ and $x(4)$, is 0.887 (Table 1a). This means that the local path properties and mean path properties are coupled in our data sets. High correlations among these variables imply that multicollinearity exists, which may cause false parameter estimation and instability of the model. The last row in Table 1a gives the correlations of $\log P/L_g$ ratios (Y) with each factor, essentially combining the data from Figures 6 to 11. The last two factors, $x(5)$, maximum sediment thickness and $x(6)$, $\gamma\Delta$, have the highest corre-

lations with Y . This anticipates the final model we obtain later.

A measure of the overall collinearity of independent variables in multiple regression analysis can be obtained by computing the condition number of the correlation matrix. The condition number is defined as the square root of the ratio of the maximum eigenvalue to the minimum eigenvalue of the correlation matrix. A large condition number provides evidence for strong collinearity. The onset of instability in a regression model due to collinearity has been empirically determined to occur when condition numbers exceed 15 [Chatterjee and Price, 1991]. In our case, the condition number of the correlation matrix is found to be 10.782. This large condition number supports our contention of collinearity; however, it is not so severe as to adversely affect our analysis. Another index to measure collinearity is the sum of the reciprocals of the eigenvalues (SRE). As a rule of thumb, if SRE is greater than 5 times the number of explanatory variables in the problem, the variables are

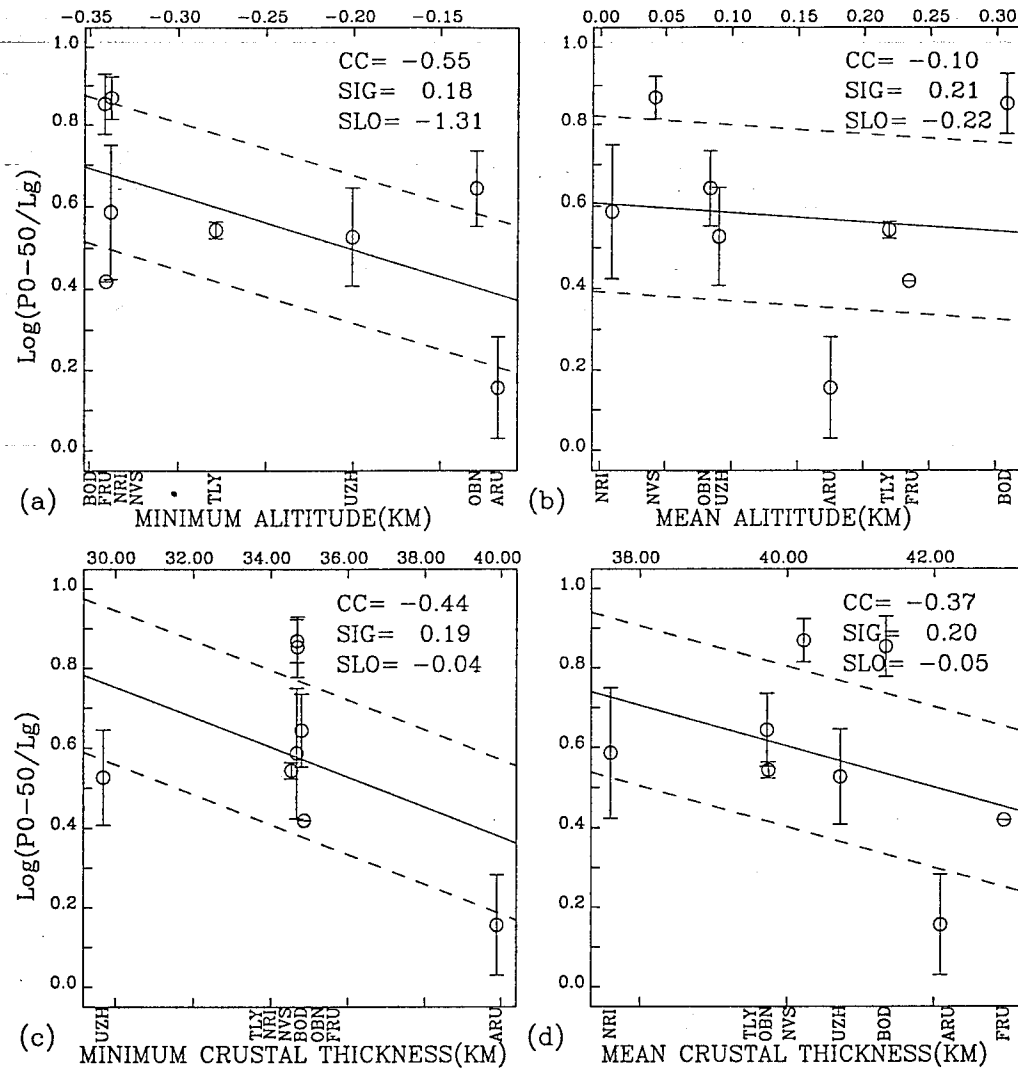


Figure 8. The log P/L_g ratio variations with (a) minimum and (b) mean altitude, (c) minimum and (d) mean crustal thickness for Novaya Zemlya explosion data.

collinear [Chatterjee and Price, 1991]. In our case the SRE value of 50.065 is larger than 30 (5×6), again confirming the existence of variable collinearity. The presence of collinearity requires us to assess the contribution of each independent variable to the regression to establish its importance. We proceed with a backward elimination method that begins with all independent variables and successively drops one at a time, based on their redundancy.

The regression results for all six parameters are shown in Table 1b, where B_j are the regression coefficients for each variable and S.E. are the standard errors associated with each coefficient. The coefficient of determination R^2 is used to assess the fit. Its definition is

$$R^2 = 1 - \frac{\sum_{i=1}^m (y_i - \hat{y}_i)^2}{\sum_{i=1}^m (y_i - \bar{y}_i)^2}$$

where \hat{y}_i are predicted values of the dependent variable, \bar{y}_i is the average value and m is the number of

observations. This quantity can be interpreted as the proportion of the variability of Y explained by the regression on variables $x(1), \dots, x(6)$. In Table 1b, $R^2 = 0.387$, which says that 38.7% of the variance of Y is accounted for by the variables $x(1)$ to $x(6)$. We do not want the value of R^2 to significantly decrease as we successively eliminate variables. Another quantity R_a^2 (adjusted R squared) is also used [Chatterjee and Price, 1991] to assess goodness of fit:

$$R_a^2 = 1 - \frac{\sum_{i=1}^m (y_i - \hat{y}_i)^2 / (m-n-1)}{\sum_{i=1}^m (y_i - \bar{y}_i)^2 / (m-1)}$$

where n is the number of independent variables. This parameter is the coefficient of determination adjusted to account for the number of variables in the regression relation. We use both R^2 and R_a^2 to provide stopping criteria in our backward elimination of the variables. Here $R_a^2 = 0.031$, which is very low, and we want to maximize its value as we eliminate parameters.

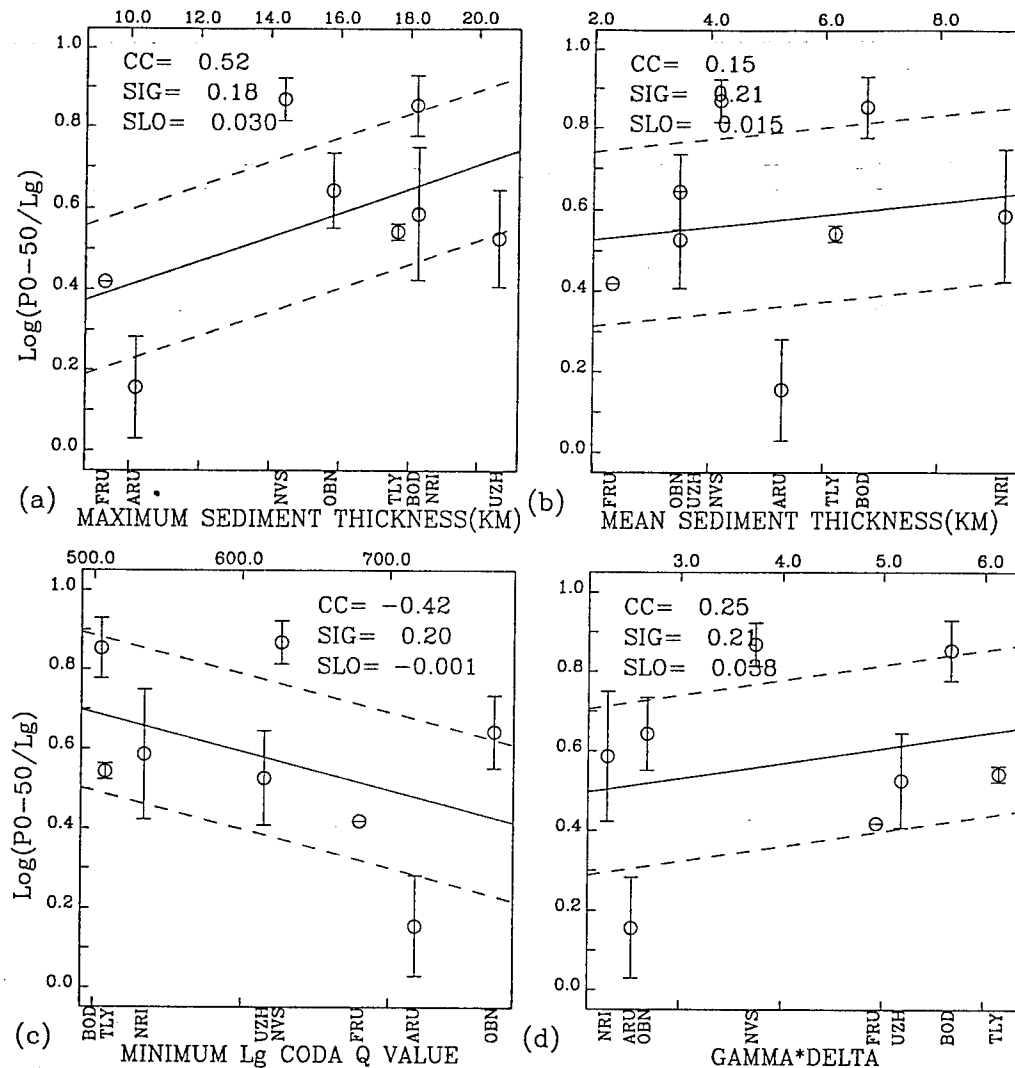


Figure 9. The $\log P/L_g$ ratio variations with (a) maximum and (b) mean sediment thickness, (c) minimum Q value and (d) attenuation term $\gamma\Delta$ for Novaya Zemlya explosion data.

To assess the significance of the model that accounts for 38.7% of the variation, we use the overall F value, which has the F distribution with n and $(m-n-1)$ degrees of freedom, as the test statistic [Chatterjee and Price, 1991]. Here n is the number of explanatory variables and m is the number of observations. The null hypothesis is all the coefficients B_j , $j = 1, 6$ are zero. This implies that there is no linear relationship between $\log P/L_g$ ratios and any of the path variables. The value of overall F computed from the six variable regression model is 4.5. The 1% right-tail point of the F distribution for 6 and 43 degrees of freedom is 3.25. Since the observed F value is larger than this, the null hypothesis is rejected at the 99% significance level: all the coefficients cannot be taken as zero. There is a linear relationship between $\log P/L_g$ ratio and at least one of the path variables.

To determine which of the independent variables is the most significant in the regression, partial F tests are performed with 1 and $m-n-1$ degrees of freedom. In the case of the partial F test, the null hypothesis is that one

coefficient, B_j , equals zero and that a linear relationship exists between the dependent variable and the remaining $n-1$ independent variables. The last column of Table 1b lists values for the partial- F statistic $F(B_j = 0)$. Only the value for $x(6)$ requires the null hypothesis to be rejected at the 95% confidence level, because $F(B_6 = 0)$ is 5.023, which is larger than 4.07, the 5% right-tail point of the F distribution for 1 and 43 degrees of freedom. Therefore any of the coefficients, except $x(6)$ can be zero. The F statistic of $x(2)$ is the lowest (0.002), so we decide to eliminate $x(2)$, mean altitude, to reduce the collinearity in the first step. The variable to be eliminated is marked with \leftarrow MPF (minimum partial F) in Table 1b, and subsequent tables.

After deleting $x(2)$, we perform the regression again with the five remaining variables. The result is in Table 2. Now the collinearity is substantially reduced. The condition number (7.40) is 32% less than before, and the sum of the reciprocals of eigenvalues (SRE = 25.078) is reduced 50.4%, however, the value is still greater than 25, five times the number of variables. Having removed

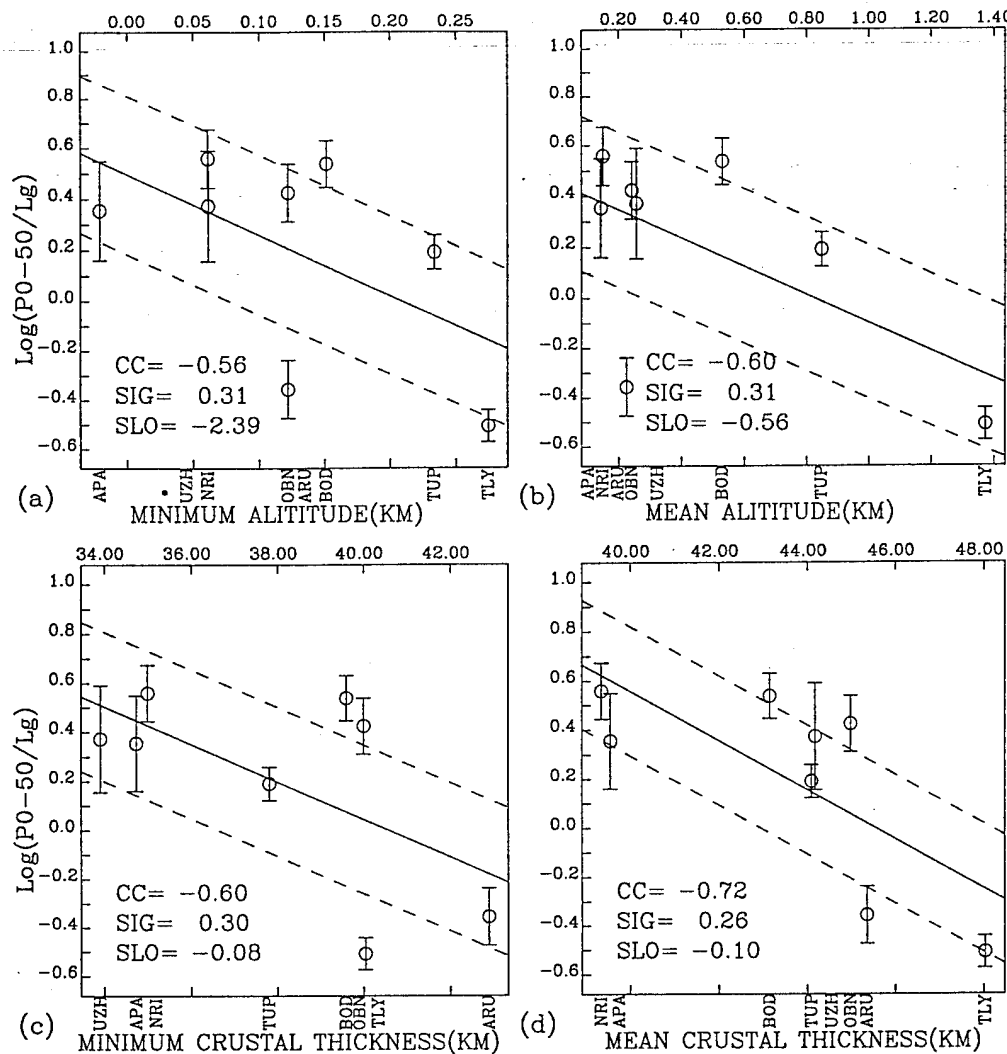


Figure 10. The $\log P/L_g$ ratio variations with (a) minimum and (b) mean altitude, (c) minimum and (d) mean crustal thickness for Semipalatinsk explosion data.

variable $x(2)$, R^2 does not decrease, which means the fit remains almost the same. Meanwhile, R_a^2 increases to 0.053, which represents improvement of the regression. Now $x(1)$ has the lowest F value, 0.024. Omitting it will have the least influence on the fit. We proceed to do so to seek a better model. The resulting regression is listed in Table 3. The corresponding condition number is 6.349 and SRE = 18.60.

Given the result shown in Table 3, we proceed to remove $x(3)$, and continue the backward elimination procedure. The next result is in Table 4. The condition number (2.177) and SRE (4.496) are reasonably small this time. However, we need to check whether the estimates of all the coefficients are statistically robust. Two of the variables still have partial F statistics less than 4.07, the 5% right-tail point of $F(1,46)$, indicating that another variable can be eliminated. Our two criteria for stopping backward elimination, a significantly decreasing R^2 and falling R_a^2 , have not been obtained, allowing us to continue the process.

Table 5 is the result for only two variables, $x(5)$, the maximum sediment thickness, and $x(6)$, the $\gamma\Delta$ term.

The condition number (1.820) and SRE (2.807) are both small now. The most important result is that both the partial F values of $x(5)$ and $x(6)$ are beyond the 5% right-tail point of $F(1,47) = 4.05$. The estimates for these two coefficients are now significant. This is our preferred model. Its R^2 is only 4.7% smaller than R^2 of the first model, and R_a^2 reaches its peak.

We did consider models for single variables, $x(5)$ or $x(6)$. However, both the R^2 (the triangles in Figure 12), and R_a^2 (the solid circles) decrease abruptly. A single variable case, using either maximum sediment thickness or $\gamma\Delta$, does not fit as well as the two variable model. This result reaffirms the importance of both crustal attenuation and sedimentary basin controls on regional phases such as L_g . However, we emphasize that the other crustal parameters undoubtedly play some role, and our statistical test merely identifies the most significant factors.

Application for Seismic Discrimination

Due to the relatively larger S wave energy excited by the source, the L_g amplitudes measured from earthquake.

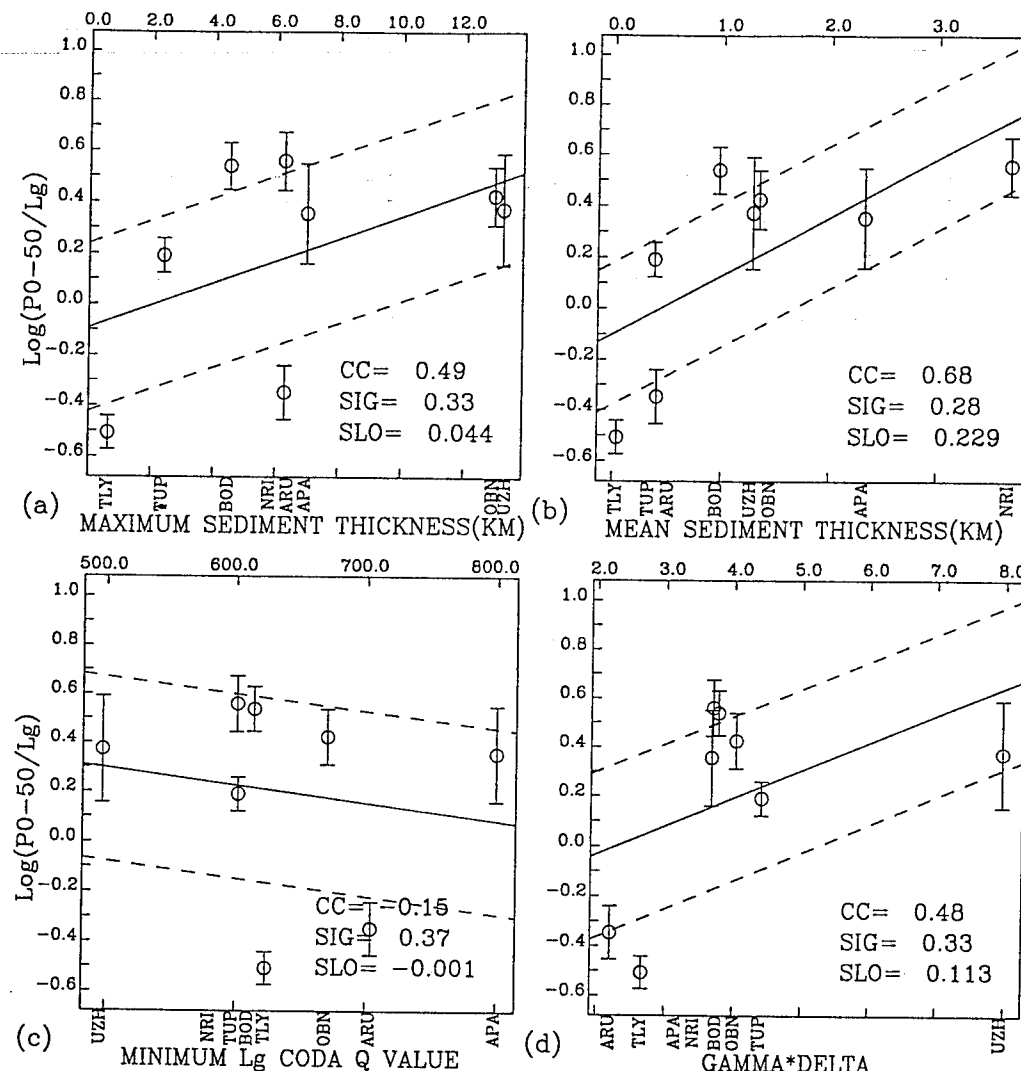


Figure 11. The $\log P/L_g$ ratio variations with (a) maximum and (b) mean sediment thickness, (c) minimum Q value and (d) attenuation term $\gamma\Delta$ for Semipalatinsk explosion data.

recordings are usually larger than those of explosion recordings with comparable P wave amplitudes. The P/L_g ratio is thus a promising discriminant for use at regional distances [e.g., Bennett and Murphy, 1986; Taylor *et al.*, 1989]. However, variations in crustal structure and attenuation cause large scatter of P/L_g ratios, and the discriminant does not work uniformly [e.g., Lynnes and Baumstark, 1991]. Figure 13a shows the

$\log P/L_g$ ratios for earthquakes (solid circles), Semipalatinsk explosions (crosses), and Novaya Zemlya explosions (pluses) as a function of m_b . The two groups of points overlap significantly. There may be many reasons for the overlap, including the physical separation of paths recording explosion and earthquake signals, the relatively low frequencies at which the measurements are made (P/L_g discriminants work best above 5 Hz, outside

Table 1a. Correlation Coefficients

Variable	$x(1)$	$x(2)$	$x(3)$	$x(4)$	$x(5)$	$x(6)$	Y
$x(1)$	1.000						
$x(2)$	0.939	1.000					
$x(3)$	0.805	0.784	1.000				
$x(4)$	0.864	0.908	0.887	1.000			
$x(5)$	-0.529	-0.541	-0.549	-0.517	1.000		
$x(6)$	-0.396	-0.292	-0.590	-0.350	0.536	1.000	
Y	-0.390	-0.362	-0.473	-0.401	0.499	0.558	1.000

Condition number is 10.782 and the sum of the reciprocals of eigenvalues is 50.065.

Table 1b. Six-Parameter Regression

Variable	B_j	S.E.	$F(B_j=0)$
$x(1)$	0.016	0.245	0.005
$x(2)$	0.008	0.201	0.002 \leftarrow MPF
$x(3)$	0.006	0.026	0.058
$x(4)$	-0.020	0.032	0.393
$x(5)$	0.014	0.011	1.668
$x(6)$	0.081	0.036	5.023
Intercept	-0.138		

$R^2 = 0.387$ $R_a^2 = 0.031$, number of observations is 50, and $F(6,43) = 4.5$.

Table 2. Five-Parameter Regression

Variable	B_j	S.E.	$F(B_j=0)$
$x(1)$	0.024	0.154	0.024 ← MPF
$x(3)$	0.006	0.025	0.058
$x(4)$	-0.019	0.027	0.514
$x(5)$	0.014	0.010	1.793
$x(6)$	0.082	0.035	5.469
Intercept	0.120		

$R^2 = 0.387$, $R_a^2 = 0.053$, number of observations is 50, and $F(5,44) = 5.5$.

the passband of this data), as well as possible failure of the discriminant due to spall from the explosions. We explore whether our empirical path corrections can improve the performance of the discriminant at all, given this most demanding set of conditions. We introduce a parameter, OV, to describe the overlap of the two populations of events. We speculate that the explosion data cover a range $\mu_1 \pm 3\sigma_1$, and earthquake data occupy $\mu_2 \pm 3\sigma_2$, where μ is the respective average ratio and σ is the standard deviation for each population. We assume $\mu_2 < \mu_1$. The overlap parameter is defined as

$$OV = \frac{\mu_2 + 3\sigma_2 - (\mu_1 - 3\sigma_1)}{s}$$

where

$$s = \sqrt{\frac{(n_1 - 1)\sigma_1^2 + (n_2 - 1)\sigma_2^2}{n_1 + n_2 - 2}}$$

is the pooled standard deviation of the two samples under consideration. Thus the overlap is expressed in units of the standard deviation [Flury and Riedwyl, 1988]. The n_1 and n_2 denote the sample size. If the two samples have no overlap in range, the OV value is negative. OV is 2.64 in Figure 13a, which reflects significant overlap and poor performance of the discriminant.

Averaging ratios for recordings from the same source can partially suppress path effects. When this is done, OV = 0.25, as shown in Figure 13b. This includes event-averaged values for all 17 earthquakes and 97 explosions. The reduction in overlap achieved by event averaging indicates the extent of path variability, although discrimination is still not achieved in this case.

We use our final model with two explanatory variables, maximum sediment thickness and $\gamma\Delta$, given in Table 5 to correct the log P/L_g ratios. The reference

Table 4. Three-Parameter Regression

Variable	B_j	S.E.	$F(B_j=0)$
$x(4)$	-0.012	0.010	1.311 ← MPF
$x(5)$	0.014	0.010	1.920
$x(6)$	0.076	0.027	8.119
Intercept	0.000		

$R^2 = 0.386$, $R_a^2 = 0.093$, number of observations is 50, and $F(3,46) = 9.6$.

sediment thickness is chosen as 10 km, and the reference $\gamma\Delta$ is 4. The choice of reference values is arbitrary, and does not affect the result. If h denotes sediment thickness, the correction is done by:

$$\text{Ratio}_{\text{corrected}} = \text{Ratio}_{\text{raw}} - (0.019\delta h + 0.079\delta(\gamma\Delta)).$$

After correction for the path effect, the variance of the ratio values for earthquake data is reduced from 0.3078 to 0.1846, about 40%. The variance for explosion observations is reduced from 0.1648 to 0.1202, more than 27%. The OV value decreases from 2.64 to 1.47. This change is still not enough to separate the two groups, but it is a significant improvement. The event average values in Figure 11d also show reduced overlap. We do not explore more quantitative discriminant measures with this data because it is clear that even with the path corrections we have not eliminated overlap. It will be of great interest to establish whether comparable path correction procedures improve discriminant performance for higher frequency P/L_g data and/or for explosion and earthquake data sampling similar paths.

Discussion and Conclusions

The empirical relationships established in this paper and by Zhang and Lay [1994a,b] indicate that regional wave propagation is influenced by attributes of gross crustal structure that can be independently determined. This has important implications for both quantifying the wave propagation effects, as well as for developing predictive ability for regional phase energy partitioning on new paths through the crust. The latter ability is of particular importance for discriminating explosion and earthquake sources in regions with no prior known explosion activity. At this time, numerical methods such as finite difference are inadequate to perform extensive modeling of the heterogeneous waveguide effects indicated by the crustal models used here, but the trends found above will

Table 3. Four-Parameter Regression

Variable	B_j	S.E.	$F(B_j=0)$
$x(3)$	0.006	0.025	0.064 ← MPF
$x(4)$	-0.017	0.023	0.560
$x(5)$	0.014	0.010	1.808
$x(6)$	0.081	0.034	5.566
Intercept	0.025		

$R^2 = 0.386$, $R_a^2 = 0.074$, number of observations is 50, and $F(4,45) = 7.1$.

Table 5. Two-Parameter Regression

Variable	B_j	S.E.	$F(B_j=0)$
$x(5)$	0.019	0.009	4.172
$x(6)$	0.079	0.027	8.823
Intercept	-0.568		

$R^2 = 0.368$, $R_a^2 = 0.099$, number of observations is 50, and $F(2,47) = 13.7$.

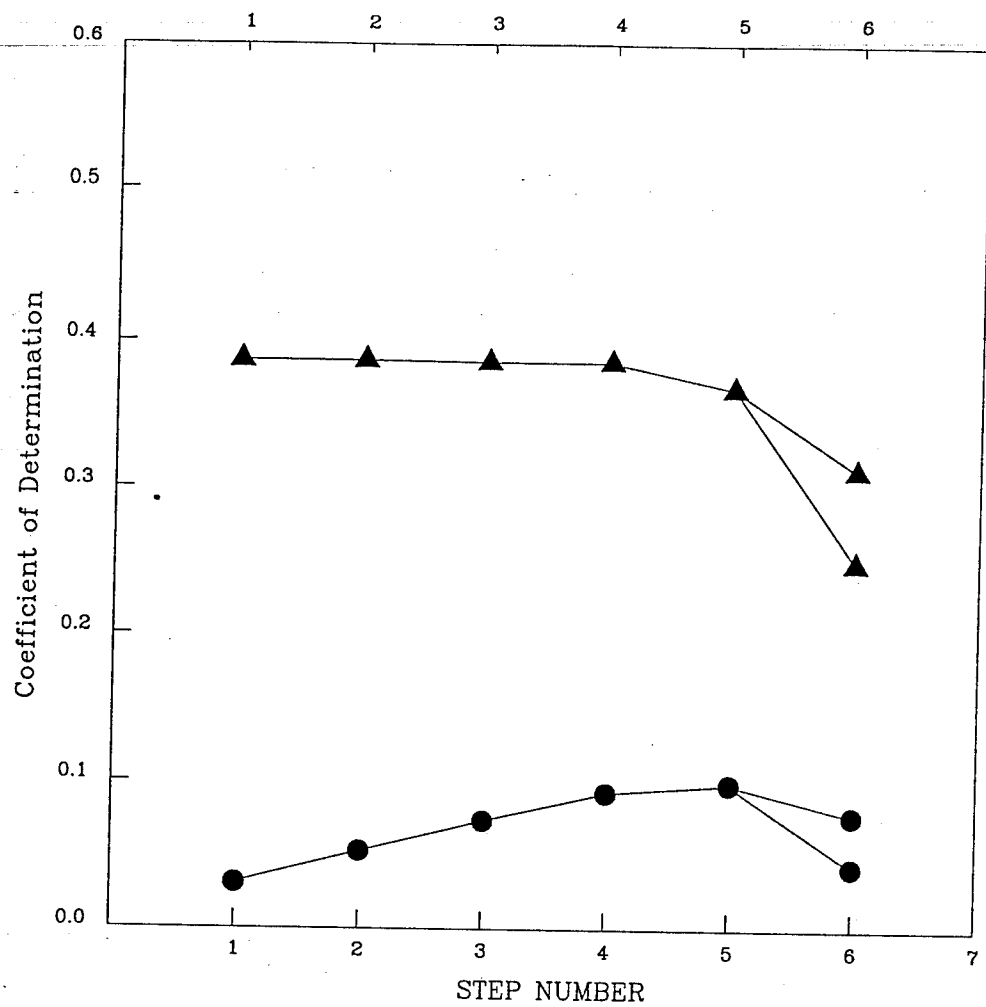


Figure 12. The behavior of the coefficient of determination R^2 and adjusted R -square R_a^2 as functions of backward elimination step. The triangles indicate R^2 , which drops only a tiny amount in the first four steps, but then drops strongly in the fifth step, when we use only one explanatory variable, sediment depth or attenuation. The solid circles are R_a^2 , which rises until the fourth variable elimination and then drops. These two statistics provide the stopping criteria of backward elimination for multivariate regression.

guide future modeling efforts, as well as provide empirical corrections.

The multivariate analysis supports the importance of both waveguide heterogeneity and crustal attenuation in shaping the regional signal. Use of higher-resolution crustal models and more accurate attenuation models may reveal the important physics better than this initial study. In addition, most of our propagation paths are long, and there is little crossing coverage with which to isolate effects.

We use the L_g coda Q model of *Pan et al.* [1992] as a parameterization of attenuation effects rather than as an explicit Q model. The L_g coda Q model undoubtedly reflects some of the L_g Q effects on any given path, but it is likely that it will not provide a full characterization of the apparent attenuation for individual paths. In deriving the L_g coda Q model, the L_g coda waves are assumed to be L_g energy scattered within an ellipse, following *Xie and Nuttli* [1988]. Thus the Q value should reflect only the attenuation properties of the crust. However, there may be some mantle contribution. Figure 14 shows empirical relationships between the attenuation

term $\gamma\Delta$ and four phases from the earthquake data: RMS P amplitudes measured in the time window from 0 to 20 s, P coda from 20 to 50 s, S_n , and L_g . The $\log L_g$ is strongly correlated with $\gamma\Delta$ (Figure 14d), but the absolute value of the slope (-0.27) is much smaller than the theoretical value for 1 Hz of $\log_{10}e = -0.43$. This indicates that the exponential attenuation relationship for a single frequency (1 Hz) cannot be directly used for the band-passed data (0.6-3 Hz in our study). The correlation of $\gamma\Delta$ with $\log S_n$ is the second strongest. S_n waves mainly propagate in the upper mantle but do involve crustal paths. This correlation with the attenuation term implies that the L_g coda used to determine the Q model may sample the upper mantle as well. However, S_n to L_g scattering may be responsible for the S_n coda having sensitivity to crustal parameters. [Baumgardt, 1990]. Although the direct P waves (0-20 s, Figure 14a) correlate weakly with $\gamma\Delta$, the P wave coda (20-50 s, Figure 14b) correlation is surprisingly strong. Perhaps scattered L_g contributes to the P wave coda, or again there may be some mantle contribution to the Q values. The correlation of P (0-50 s), used above, is almost as strong as

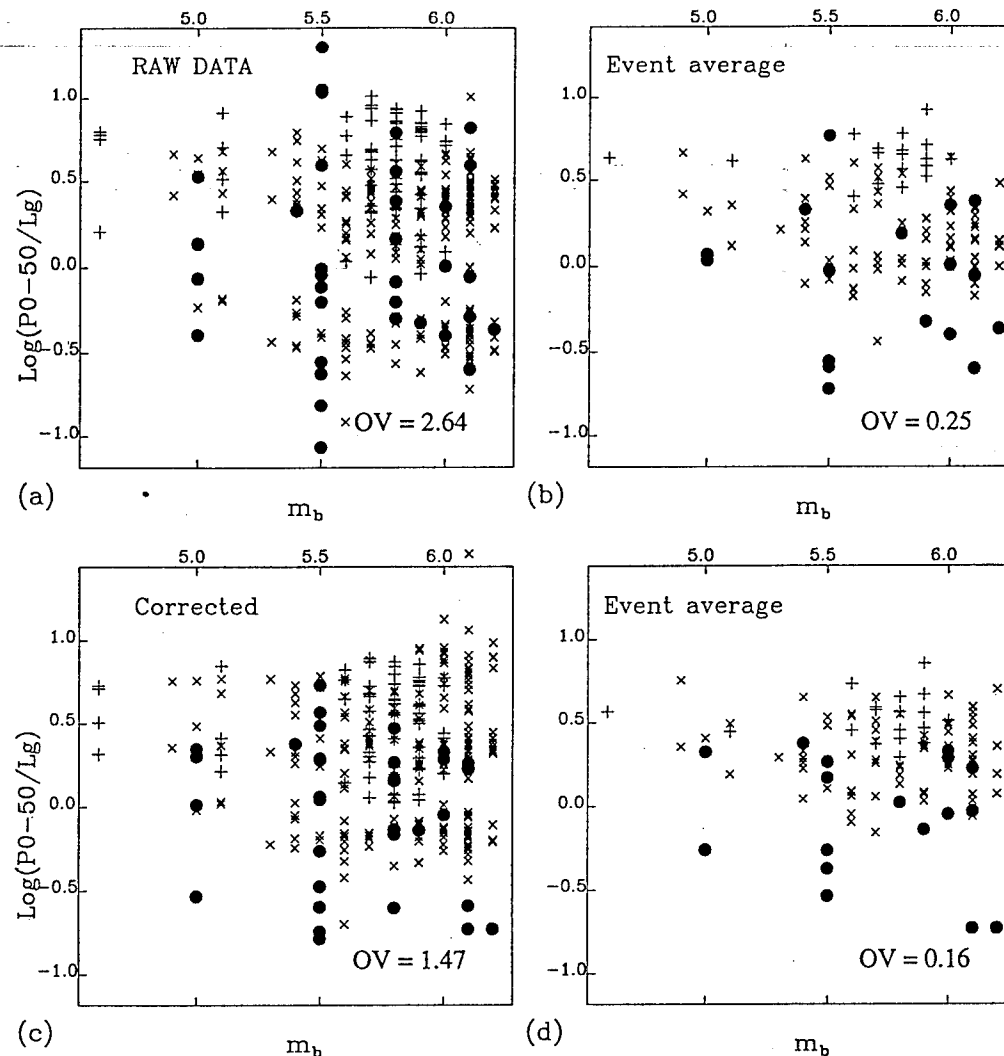


Figure 13. The $\log P/L_g$ ratios for earthquakes (solid circles) and explosions (crosses for Semipalatinsk data and pluses for Novaya Zemlya data) as a function of m_b . (a) individual raw data, (b) event-averaged raw data, (c) individual data after applying the multivariate model to correct for path effects, and (d) event-averaged corrected data. The variances and overlaps of both groups are reduced after correction.

P (20-50 s). It appears that the Q model generally has the right geographic pattern, and certainly attenuation is an important factor influencing the regional wave propagation for the various phases. However, it seems that L_g coda Q not only represents the attenuation property of crust but also that of upper mantle, given the strong relations with S_n and P coda. This may also indicate coupling between Q structure in the crust and upper mantle, a natural consequence of tectonic processes. Unlike for L_g , we do not have any theoretical framework for directly correcting the P amplitudes for attenuation, thus we have treated the effect of $\gamma\Delta$ on the P/L_g values empirically.

Zhang and Lay [1994b] attribute correlations found with maximum water depth to either locally thick sediment layers or thin crust and could not find a robust procedure to separate the effects of the two factors. One of the objectives of this study was to better elucidate propagation effects on regional signals. We obtain a "best fit" model through multivariate regression; however, we

emphasize that the solution found is not unique. Besides waveguide attenuation, the structural parameters may all have some importance. The maximum sediment thickness factor ($x(5)$) is correlated with the other structural factors with correlation coefficients > 0.5 (Table 1a). If we use $\gamma\Delta$ plus any of the other structural factors, instead of maximum sediment thickness, the resulting fits are not far from the best one. Table 6 shows these results, where the columns indicate models with $\gamma\Delta$ plus one of the following: minimum altitude, mean altitude, minimum crustal thickness, mean crustal thickness, and maximum sediment thickness. All the coefficients of determination R^2 are greater than 0.344, only slightly smaller than 0.368 for the best model with maximum sediment thickness and $\gamma\Delta$. All the overall F values are greater than the 1% right-tail point of $F(2, 46) = 5.10$. However, only the maximum sediment thickness coefficient passes the partial F test; in the row marked "partial F ", 4.172 $> 5\%$ right-tail point of $F(1, 46) = 4.05$. Our choice of the "best model" with $\gamma\Delta$ and maximum sediment thick-

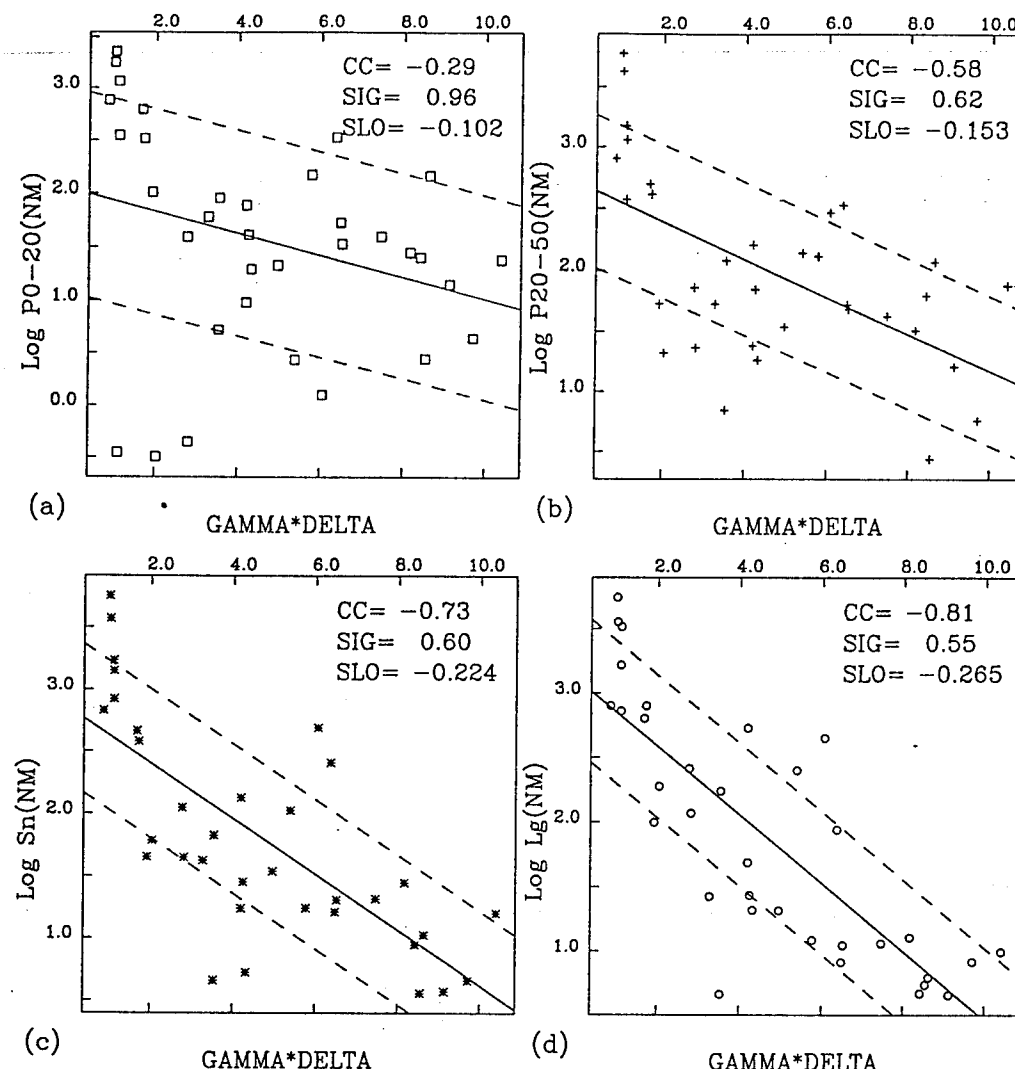


Figure 14. Correlations of the path attenuation term $\gamma\Delta$, computed from the L_g coda Q model [Pan et al., 1992] with (a) P wave RMS amplitude measured in the 0-20 s window, (b) P wave coda RMS amplitude measured in a 20-50 s window, (c) RMS S_n , and (d) RMS L_g . These correlations imply that the L_g coda Q reflects not only crustal properties but also the upper mantle to a lesser extent.

ness is clearly preferred in a statistical sense but the strong collinearity in the problem should not be overlooked.

Although the crustal thickness is not included in our final model, its importance cannot be neglected. Its partial F value is only 30% less than that of sediment thickness (Table 4). Our study area includes two regions with some of the thickest sediment layers in the world, the effect of which is pronounced. In other regions lacking such thick sediment regions, crustal thickness meas-

ures may be more influential. Measures of crustal thickness variation should be further explored for their influence on the regional signals.

While we gain some insight into regional wave energy partitioning by these empirical approaches, synthetic calculations are ultimately needed to fully understand the coupled relationships. The coupling of structural parameters and Q is also important to consider. Mitchell and Hwang [1987] conclude that $L_g Q$ and sediment thickness are coupled in the central United States, but are not related in the western United States. It is possible that these factors are related in portions of Eurasia and not in other regions, giving rise to significance as two separate variables in our multivariate regressions. Variation in sediment thickness may also play an important role in L_g blockage.

Our primary conclusion is that the combined effect of the two crustal variables: $\gamma\Delta$, which reflects the gross attenuation properties of each path, and maximum sediment thickness, which is the most prominent structure factor causing blockage of L_g , dominate the path effect

Table 6. Comparison of Alternate Models

	$\gamma\Delta$			+	
	minimum altitude	mean altitude	minimum crustal thickness	mean crustal thickness	maximum sediment thickness
R^2	0.346	0.355	0.344	0.360	0.368
Over all F	12.4	13.0	12.3	13.2	13.7
Partial F	2.428	3.167	2.273	3.521	4.172

on the regional log P/L_g ratio. This offers the potential to reduce variance in measurements of these ratios for seismic discrimination applications.

Acknowledgements. We thank J. Xie and Y. Pan for providing us with their L_g coda Q model. E. Fielding of Cornell kindly provided the data on Moho depth and sediment thickness. We make extensive use of the graphics software GMT provided by P. Wessel and W. H. F. Smith. We thank T. L. Pratt, S. R. Taylor and D. R. Baumgardt for helpful comments on the manuscript. This research was supported by the W.M. Keck Foundation, the Advanced Research Projects Agency monitored by the Phillips Laboratory under contract F29601-91-K-DB18 and grant F49620-92-J-0461 from the Air Force Office of Scientific Research. This is contribution 239 of the Institute of Tectonics and the W. M. Keck Seismological Laboratory.

References

Baumgardt, D. R., Investigation of teleseismic L_g blockage and scattering using regional arrays, *Bull. Seismol. Soc. Am.*, 80, 2261-2281, 1990.

Baumgardt, D. R., and G. B. Young, Regional seismic waveform discriminants and case-based event identification using regional arrays, *Bull. Seismol. Soc. Am.*, 80, 1874-1892, 1990.

Bennett, T. J., and J. R. Murphy, Analysis of seismic discrimination capabilities using regional data from western United States events, *Bull. Seismol. Soc. Am.*, 76, 1069-1086, 1986.

Bennett, T. J., A. K. Campanella, J. F. Scheimer, and J. R. Murphy, Demonstration of regional discrimination of Eurasian seismic events using observations at Soviet IRIS and CDSN stations, *Tech. Rep. PL-TR-92-2090*, Phillips Lab., Hanscom Air Force Base, Mass., 1992.

Campillo, M., L_g wave propagation in a laterally varying crust and the distribution of the apparent quality factor in central France, *J. Geophys. Res.*, 92, 12,604-12,614, 1987.

Campillo, M., Propagation and attenuation characteristics of the crustal phase L_g , *Pure Appl. Geophys.*, 132, 1-19, 1990.

Campillo, M., J. L. Plantet, and M. Bouchon, Frequency-dependent attenuation in the crust beneath central France from L_g waves: Data analysis and numerical modeling, *Bull. Seismol. Soc. Am.*, 75, 1395-1411, 1985.

Cao, S., and K. J. Muirhead, Finite difference modeling of L_g blockage, *Geophys. J. Int.*, 116, 85-96, 1993.

Chatterjee, S. and B. Price, *Regression Analysis by Example*, John Wiley, New York, 1991.

Chun, K.-Y., T. F. Zhu, and X. R. Shih, Time domain analysis of L_g wave attenuation in Eurasia, in *Regional Wave Attenuation in Eurasia*, *Sci. Rep. 2, Def. Adv. Res. Proj. Agency/Nuclear Monitoring Research Office, Arlington, Va.*, 3-12, 1992.

Fielding, E. J., B. L. Isacks, and M. Barazangi, A geological and geophysical information system for Eurasia, *Tech. Rep. 2, F19601-91-K-DB08*, Phillips Lab., Hanscom Air Force Base, Mass., 1992.

Flury, B. and H. Riedwyl, *Multivariate Statistics*, Chapman and Hall, New York, 1988.

Israelsson, H., RMS L_g as a yield estimation in Eurasia, final report, Phillips Lab., Hanscom Air Force Base, Mass., 1992.

Jih, R-S., Statistical characterization of rugged propagation paths with application to R_g scattering study, *Tech. Rep. TGAL-93.7*, Teledyne Geotech, Alexandria, Va., 1993.

Kennett, B. L. N., L_g waves and structural boundaries, *Bull. Seismol. Soc. Am.*, 76, 1133-1141, 1986.

Kunin, N. Y., Distribution of sedimentary basins of Eurasia and the volume of the Earth's sedimentosphere, *Int. Geol. Rev.*, 22, 1257-1264, 1987.

Kunin, N. Y., and E. R. Sheykh-Zade, New data on lateral inhomogeneities in the upper mantle under western Eurasia, *Dokl. Akad. Nauk. USSR*, 273, 1087-1091, 1983.

Lynnes, C., and R. Baumstark, Phase and spectral ratio discrimination in North America, *Final Tech. Rep., PL-TR-91-2212(II)*, Phillips Lab., Hanscom Air Force Base, Mass., 1991.

Maupin, V., Numerical modeling of L_g wave propagation across the North Sea central graben, *Geophys. J. Int.*, 99, 273-283, 1989.

Mitchell, B. J., and H. J. Hwang, Effect of low Q sediments and crustal Q on L_g attenuation in the United States, *Bull. Seismol. Soc. Am.*, 77, 1197-1210, 1987.

Mitchell, B. J., J. Xie, Y. Pan, and J. Ni, L_g Q , L_g coda Q and yield estimation in Eurasia, in paper presented at the 15th Annual Seismic Research Symposium, Phillips Lab./GPE, Vail, Colo., 1993.

Nicolas, O. W., B. Mechler, and M. Bouchon, Attenuation of regional phases in Western Europe, *Bull. Seismol. Soc. Am.*, 72, 2089-2106, 1982.

Nuttli, O. W., The excitation and attenuation of seismic crustal phases in Iran, *Bull. Seismol. Soc. Am.*, 70, 469-485, 1980.

Nuttli, O. W., On the attenuation of L_g waves in western and central Asia and their use as a discriminant between earthquakes and explosions, *Bull. Seismol. Soc. Am.*, 71, 249-261, 1981.

Nuttli, O. W., Yield estimates of Nevada test site explosions obtained from seismic L_g waves, *J. Geophys. Res.*, 91, 2137-2151, 1986.

Nuttli, O. W., L_g magnitudes and yield estimates for underground Novaya Zemlya explosions, *Bull. Seismol. Soc. Am.*, 78, 873-884, 1988.

Pan, Y., B. J. Mitchell, J. Xie, and J. Ni, L_g coda Q across northern Eurasia, paper presented at the 14th Annual Seismic Research Symposium, Phillips Lab./Darpa, Tucson, Az., 1992.

Press, F., and M. Ewing, Two slow surface waves across North America, *Bull. Seismol. Soc. Am.*, 42, 219-228, 1952.

Regan, J., and D. G. Harkrider, Seismic representation theorem coupling: Synthetic SH mode sum seismograms for non-homogeneous paths, *Geophys. J. R. Astron. Soc.*, 98, 429-446, 1989.

Taylor, S. R., M. D. Denny, E. S. Vergino, and R. E. Glaser, Regional discrimination between NTS explosions and western U.S. earthquakes, *Bull. Seismol. Soc. Am.*, 79, 1142-1176, 1989.

Wessel, P., and W. H. F. Smith, Free software helps map and display data, *Eos*, 72, 441, 445-446, 1991.

Xie, J., and B. J. Mitchell, A back-projection method for imaging large-scale lateral variations of L_g and coda Q with application to continental Africa, *Geophys. J. Int.*, 100, 161-181, 1990.

Xie, J., and O. W. Nuttli, Interpretation of high-frequency coda at large distances: stochastic modeling and method of inversion, *Geophys. J. R. Astron. Soc.*, 95, 579-595, 1988.

Zhang, T., and T. Lay, Analysis of short-period regional phase path effects associated with topography in Eurasia, *Bull. Seismol. Soc. Am.*, 84, 119-132, 1994a.

Zhang, T., and T. Lay, Effects of crustal structure under the Barents and Kara seas on short-period regional wave propagation for Novaya Zemlya explosions: empirical relations, *Bull. Seismol. Soc. Am.*, 84, 1132-1147, 1994b.

T. Lay, S. Y. Schwartz and T.-R. Zhang, Institute of Tectonics, University of California, Santa Cruz, CA 95064. (e-mail: thorne@rupture.ucsc.edu; susan@earthsci.ucsc.edu; tien@earthsci.ucsc.edu)

(Received April 22, 1994; revised August 5, 1994; accepted August 11, 1994)